Numerical modeling and failure prediction of laser welded joints in a support of car seat

Waseem Arif

Thèse de doctorat

Pour obtenir le grade de Docteur de l'Université de VALENCIENNES ET DU HAINAUT-CAMBRESIS

Discipline: Mécanique

École Doctorale: Science pour l'ingénieur (SPI)

Laboratoire d'Automatique, de Mécanique et d'Informatique Industrielles et Humaines (LAMIH), UMR CNRS 8201

Présenté par: **Waseem ARIF**

Modélisation numérique d'assemblage soudé par laser de châssis pour sièges de voiture, sous sollicitations dynamiques.

Date de Soutenance : **10 Avril 2017**

A Valenciennes, devant le jury:

Karl DEBRAY	Professeur	URCA	(Rapporteur)
Nathalie BOUDEAU	Professeur	Université de Franche-Comté	(Rapporteur)
Veronique FAVIER	Professeur	Arts et Métiers ParisTech	(Présidente du jury)
Nicolas LECONTE	Maitre de conférence	Université de Valenciennes	(Examinateur)
Hakim NACEUR	Professeur	Université de Valenciennes	(Directeur de thèse)
Eric MARKIEWICZ	Professeur	Université de Valenciennes	(Co-directeur de thèse)
Mohamed BEN TKAYA	FEA Engineer	Faurecia Automotive Seating	(Invité)

Abstract

Nowadays environmental policies have become more strict towards the automotive industry to reduce the CO_2 emission, therefore lightweight structures using high strength materials have become of great interest. Two different FE models namely "*Solid Refine Model*" (SRM) and "*Shell Coarse Model*" (SCM) have been developed and are being used as standard models by Faurecia Automotive Seating (Caligny). The SRM is capable to predict accurately the local welding behavior but unfortunately, due to its high computational cost, the SRM is not suitable for a full car seat modeling. On the other hand, the SCM is computationally efficient but it cannot predict the weld line behaviour. The aim of the present thesis is to develop a multimaterial FE model within the Ls-dyna commercial software, which will enhance the SCM to allow the accurate prediction of weld line behavior until failure with a reasonable computational cost. The standard quadrilateral shell FE is developed and enriched using a recently developed method called the "*Interpolation Covers Method*" (ICM) to capture the solution gradients accurately without mesh refinement. An elasto-plastic material model is developed within Ls-dyna commercial software which takes into account two different materials namely BM and HAZ inside a single shell element. The Generalized Incremental Stress State dependent damage Model has been implemented as a UMAT within Ls-dyna commercial software to predict the weld line failure in SCM. The different developments have allowed the SCM to become able to predict the complex behavior of the welded line accurately until failure, at low computational cost compatible with the industrial needs.
Keywords : LBW; SRM; SCM; Interpolation covers method; Multimaterial element; GISSMO
Résumé :
De nos jours, les politiques environnementales sont devenues plus strictes envers l'industrie automobile pour réduire les émissions de CO_2, donc les structures légères utilisant des matériaux de haute résistance sont d'un grand intérêt. Deux modèles différents EF, à savoir "Solid Refine Model" (SRM) et "Shell Coarse Model " (SCM) ont été développés et sont utilisés comme modèles standard par Faurecia Automotive Seating (Caligny). Le SRM est capable de prédire avec précision le comportement de soudage local, mais malheureusement, en raison de son coût de calcul élevé, le SRM n'est pas adapté à une modélisation de sige de voiture complète. D'autre part, le SCM est efficace sur le plan numérique, mais il ne peut pas prédire le comportement de la ligne de soudure. L'objectif de la présente thèse est de développer un modèle EF multi-matèriel dans le logiciel commercial Ls-dyna, qui améliorera le SCM pour permettre une prédiction précise du comportement de la ligne de soudure jusqu'à l'échec avec un coût de calcul raisonnable. Le modèle FE quadrilatère standard est développé et enrichie à l'aide d'une méthode récemment développée appelée "Interpolation Covers Method" (ICM) pour capturer les gradients de la solution avec précision sans raffinement de maillage. Un modèle de matériau élasto-plastique est développé dans le logiciel commercial Ls-dyna qui prend en compte deux matériaux différents à savoir BM et HAZ dans un seul élément de coque. Le modèle généralisé d'endommagement dépendant de l'état de contrainte a été implémenté comme UMAT dans le logiciel commercial Ls-dyna pour prédire l'échec de la ligne de soudure dans SCM. Les différents développements ont permis au SCM de prédire avec précision le comportement complexe de la ligne soudée jusqu'à l'échec, à faible coût de calcul compatible avec les besoins industriels.
Mots-clés : LBW; SRM; SCM; Interpolation covers method; élement multi-materiel; GISSMO

Acknowledgement

First of all, I am wholeheartedly thankful to Almighty Allah (SWT), the most merciful and the most compassionate, the sustainer, the creator and Lord of all the universes, Who endowed me with the hearing, vision, hearts and gave me courage to complete my thesis. My special praise for the last Prophet Muhammad (PBUH), who is a perfect role model to be followed, may Allah shower the blessings upon him. Thereafter, I would like to express my gratitude, from deep of my heart, to Professor Hakim Naceur, director of the thesis and my research father, who selected me and believed me to be an appropriate student to carry out this project. He continuously guided and supervised me thorough out the course of my thesis. He has always been there next to me to listen all of my questions, confusions and curiosities and guided me in the right direction. I would say that this work was not possible without his constant guidance and encouragement. He has ability to find the solution from out of the box. I found him a true passionate researcher and hard worker and his personality was always impressive for me. I would like to express my gratitude to Professor Eric Markiewics, co-director of the thesis, who gave me an opportunity to work in his department. I also would like to thank to Dr. Nicolas Leconte, my co-supervisor, who supported me and his critical remarks kept me on the right track.

I would like to thank to all of my colleges in the, International Campus on the Safety and Inter-modality of Transport (CISIT), who helped me one or another way. I also appreciate the funding of Faurecia, the automotive seating industry in Caligny.

I would like to extend my sincere gratitude to all of my family members back to Pakistan. I would like to thank to my parents for their unconditional love, prayers and support throughout my life. I don,t have words to express their everlasting love to me. I would like to thank to all of my brothers and sisters for their best wishes. I would express my gratitude to my beloved wife and my son who made my life colourful and gave me a reason to live a happy life. All of my family members continuously supported and encouraged me throughout all the course of my theis. At the end, I would like to thank to my motherland, Pakistan, where I brought up and completed my early education.

May Almighty Allah (SWT) bless all the above mentioned. Ameen.

Waseem Arif

Contents

List of Tables

List of Figures

State of the art of laser welding

1.1 Laser beam welding technology

Fuel economy and, thereby, weight reduction have become a point of considerable interest in the car industry over the past 20 years [1]. Increasing concern of environmental safety and reduction of fuel consumption motivate car manufacturers to use lightweight materials having a higher tensile strength coupled with better ductility. By reducing the weight of a car less fuel consumption along with less CO_2 emission can be achieved. The body-in-white, the heaviest and largest car component, comprises about 25–30 percent of the total weight of a medium-sized passengers car [2]. Hence, it has to fulfil a variety of material relevant requirements. For car manufacturer, five demanding areas can be distinguished: cost, production, styling and space optimization, physical characteristics and quality, environmental impact. The dominating role of steel as the material for car bodies is attributed to its good response to most of these requirements and its adaptability. Cold rolled, high strength sheet steels have been developed predominantly for automotive applications, and newly developed high strength steels are measured by the five criteria listed. Hence, the aim is to increase strength without decreasing formability, join-ability, coat-ability, and also process ability. Various new grades of steels - IF (Interstitial Free), DP (Dual Phase), HSLA (High Strength Low Alloy) - have been developed which show excellent formability and are able to meet the most automotive requirements [3].
It is often stated that a very high percentage of a country's gross domestic product is related to welding in one way or another [4] and in the case of the automobile body structure welding is the mostly used joining operation. In previous years, car bodies were mostly manufactured by mild steel and assembled via resistance spot welding (RSW), a method which fulfilled the demand of automobile manufacturers for high process speed and high volume scenario. But due to the changed material scenario, other welding methods have also gained popularity in the industry. A significant amount of work has been conducted on the mechanical property of the welded DP steel joined by other welding processes, such as resistance spot welding (RSW) [5–7], laser spot welding [8], gas metal arc welding (GMAW) [9], and friction stir welding [10]. A lot of work can also be found on the laser weldability of DP steel coupled with the effect of welding on the tensile properties [11]. Due to ease of automation and flexibility laser welding has already gained its reputation in the metal joining field. Spot welding processes are recently being replaced by laser welding processes in the auto-body assembly industry to improve productivity and to reduce costs.
Laser beam welding (LBW) is a fusion welding process that results in joining of materials by the interaction of a concentrated, coherent beam of light and the material surface. Laser welding is a highly efficient and precise welding method, which is greatly desired in the automotive, aeronautical and ship building industries. It elucidates some excellence, such as higher depth to width ratio [12], concentrated heat input, minimal thermal distortion, minimized weld fusion and heat affected zone, reduced post weld rework and possibly joining widely dissimilar materials [13]. But laser welding has also clearly demonstrated some drawbacks. First of all, the cost of laser

equipment and maintenance are high. Second, highly reflective materials, such as aluminum, copper and gold, are more difficult to process with some laser sources. Finally, the high welding speed leads to high solidification rate, which in turn induces metallurgical problems, such as cracking, pores and brittle phase structures [14].

The lasers used in welding can be divided into different types by the wide variety of lasing gain medium types available such as gas (He-Ne and carbon dioxide), solid state (neodymium-doped yttrium aluminum garnet; $Nd : Y_3Al_5O_{12}$), semiconductor (diode lasers) etc. Nd: YAG lasers are the most common type of solid-state laser used for welding. Disregarding laser brazing and soldering as different joining methods, laser welding can be divided into: conduction mode laser welding and keyhole (or deep penetration) welding. In the first method, the laser beam is absorbed at the workpiece surface, forming a semicircular weld cross section whereas in the second method, the power density of the laser beam is sufficiently high to cause evaporation, forming a capillary that enable the beam to penetrate deeper into the workpiece, forming a narrow deep weld. Except plasma and electron beam welding, no other welding methods can reach high enough power densities to form a keyhole. The process can also be divided into pulsed wave and continuous wave welding.

Laser hybrid arc welding (LHAW) has been increasingly noted a promising joining process. It combines laser and electric arc welding (usually MIG/MAG) and compensates the drawbacks or weaknesses occurring in laser welding and arc welding. It uses the advantages of high precision, welding speed and penetration depth associated with lasers and the addition of cheap extra heat input and wire addition [14]. Laser-gas metal arc (GMA) hybrid welding is one of the state-of-the-art technologies and is designed to overcome problems commonly encountered during either laser or arc welding. Hybrid welding offers some additional advantages over mere laser and arc welding. Firstly, the combination of a laser beam and gas metal arc in welding will reduce the propensity for cracking, brittle phase formation and porosity. Secondly, the feeding wire modifies the metallurgy of the weld. Thirdly, the effect of the coupled process exceeds the effects of the laser and arc heat sources taken separately, and the laser beam located in front of the GMA weld pool could suppress hump formation during high travel speed [13]. Multi-kilowatt CO_2 lasers are increasingly being used for welding applications due to their capability of producing deep penetration welds at high welding speeds. Although most metals are being successfully welded, laser welding of aluminum alloys is proving to be very difficult. Laser welds in aluminum alloys contain extensive porosity, and excessive vaporization of alloying elements occurs from the fusion zone. The welds have severe undercuts and large discontinuous cavities on the bead surface [16].

Significant progress has been made to improve the quality of the laser welds. One progress is development of Arc-augmented laser welding process. This process involves rooting of an electric arc into the keyhole or the laser-material interaction zone produced during laser welding. It was observed that such an arc augmentation gives a welding speed which is almost four times the speed obtained with laser welding alone. The arc current plays an important role in determining whether full penetration in the weld would occur. It was reported that maximum welding speed increases with increasing arc current. Second progress in laser beam welding is invention of dual-beam laser welding process. By using this process, It was observed that welding of aluminum sheets resulted in significant reduction in porosity when the second beam was defocused. One of the beams can be used for melting of the workpiece during welding, while, the other beam can be used either for preheating of workpiece ahead of welding beam or post-heating (heat treatment) of the welds past the welding beam. Another improvement is laser welding of tailor-welded blanks. Significant reduction in the weight of the vehicle can be achieved by welding the blanks (of various materials, thicknesses, properties, surface treatments, etc.) into a single "tailor-welded blank" [12].

1.2 Laser welding defects

1.2.1 Porosity

Large voids at the bottom and small distributed voids towards the surface and small bubbles related with trapping gas bubble during solidification. Porosity can be minimized by optimizing the laser parameters such that the stability of the keyhole is improved and the turbulence in the fluid flow is minimized. Number of pores per unit weld length can be reduced by increasing the welding speed and improving the laser beam quality [15, 16].

1.2.2 Cracks

Restrictions to free contractions of material during cooling cycle resulting high tensile stresses causing cracking. There are mainly two types of cracks can be found in laser welded structure.

- Solidification cracking in weld metal. Material properties like large solidification range, high thermal expansion, and large solidification shrinkage contribute to solidification cracking.
- Liquation cracking in base metal. It occurs in partially melted zone as a result of large quantity of alloying addition that form eutectic phase with low melting point. Liquid will tear if sufficient stress is present [17].

1.3 Microstructure of laser beam welding

This section focuses on impact of microstructure of welded structures on mechanical properties. Phase transformation occurs in different zones of welded specimen during welding process. This phase transformation remarkably influences mechanical properties in these areas. Microstructure can be controlled by manipulating welding parameters e.g. welding speed, laser type etc. The main focus is on the welding of different steel grades and alteration of their mechanical properties due to microstructural changes.
Dual Phase steel, so called because they consist essentially of a dispersion of martensite in a ferrite matrix, are produced by inter-critically annealing and cooling at such a rate as to give the desired structure. The microstructure and mechanical properties of laser welded joints in dual phase HDT580X steel have been presented by Weglowski et al. [18]. Butt-welded joints 2.4 mm in thickness have been produced by using a Nd:YAG laser and deep penetration method was adopted. Optical and scanning microscope has been used to investigate microstructure. The microstructure of welded joints is mainly composed of lath martensite in the weld and a mixture of lath martensite, bainite and ferrite in the heat affected zone (HAZ). Microhardness is measured on metallographic samples across the weld and base metal by using Vicker hardness tester at a load of 500g. The base material hardness values did not exceed 226 HV. In the HAZ there was an increase of hardness to 285 HV. The maximum hardness 343 HV was observed in the weld. These results confirmed that the low carbon lath martensite was present in the weld and HAZ.
Farabi et al. [19] investigated the microstructural change after laser welding and its effect on the mechanical properties in DP600 steel. The DP600 steel having a thickness of 1.2mm was selected to weld by using diode laser welding technique. The cross sectional microstructures of the welded specimens were examined by using an optical microscope coupled with Clemex image analysis system. Microstructural study indicates that predominantly martensite in conjunction with some side-plate ferrite and bainite is present in the fusion zone (FZ). The formation of martensite in the FZ resulted from the rapid cooling of the weld pool during laser welding

process. On the basis of hardness, HAZ can be divided into inner and outer zones. The inner zone, region near the fusion zone, had a higher hardness than the region close to the base metal due to the formation of martensite. The outer zone, region near the base metal, was observed to have a lower hardness value than the base metal and also called the soft zone. The presence of the soft zone was mainly due to tempering of pre-existing martensitic phase. The engineering stress strain curves were obtained from both the base metal and the welded joints at different strain rates. The experimental results indicated that failure occurred at outer HAZ in welded samples. The welded joints had higher yield strength than the base metal but the tensile strength of the welded specimens was slightly lower than that of the base metal. While both yield strength and ultimate tensile strength slightly increased with increasing strain rate.

Microstructural change and its impact on mechanical properties of laser welded dissimilar DP600/DP980 steel joints was investigated by Farabi et al. [20]. The two dissimilar dual phase steels DP600/DP980 were welded using diode laser welding. Scanning electron microscope (SEM) was used to see microstructural changes during the laser welding process. The fusion zone of this kind of welded joints contained mainly martensite along with side-plate ferrite due to rapid cooling of the weld pool. The HAZ at the DP600 side showed tempered martensite and possibly bainite along with some pre-existing martensite in the ferrite matrix. The HAZ microstructure at the DP980 steel was consisting of tempered martensite along with some possible bainite in conjunction with some pre-existing martensite in the ferrite matrix. Significantly higher hardness was observed in the FZ due to the formation of prevailing martensite. There existed a signifcant hardness drop called soft zone in the HAZ. The degree of softening was more severe and size of the soft zone was larger at the DP980 side. The occurrence of the soft zone was partly attributed to the disappearance of martensite and partly due to tempering of the remaining martensite pre-existed in the base metals during laser welding. Stress strain curves for both metals and laser welded dissimilar welded joints at a strain rate $1 \times 10^{-2} s^{-1}$ were obtained and compared . The experimental results showed that failure occurred in the soft zone at the DP600 side. The YS of the dissimilar welded joints was apparently higher than that of the DP600 base metal but it was lower than the YS of DP980 base metal. The UTS of the dissimilar welded joints was observed to be essentially the same as that of the DP600 base metal.

The effect of fiber laser welding (FLW) and diode laser welded (DLWed) on the microstructure, hardness and tensile properties of DP980 was identified by Xu et al. [21] with single linear and multiple linear joint geometry. The welding of DP980 steel with $1.2mm$ thick sheet was conducted using a Nuvonyx diode laser system at welding speed 1 m/min and an IPG Photonics YLS-6000 fiber laser system at speed 16 m/min. It was observed that more martensite decomposition occurred in the HAZ of the DLWed joint than in the HAZ of the FLWed joint. The wider HAZ and lower hardness in FZ in DLW was due to much lower welding speed. After welding, higher hardness was observed in the FZ of both DLWed and FLWed joints, and soft zones occurred beside the FZ in both types of laser welded joints. The engineering stress strain curves from base metal, DLW and FLW with sigle linear and multiple linear joint geometery were obtained at a strain rate of $1 \times 10^{-3} s^{-1}$. It was noticed that that YS and UTS of FLW was remained very close to that of BM 980 steel. However, remarkably decreased YS and UTS were found in DLW. There was no obvious difference of the tensile properties between the FLWed DP980-S and DP980-M joints was observed.

Coelho et al. [22] studied the effect of different combinations of induction heating and autogenous CO_2 laser welding on the gradient of microstructure and microhardness in butt joints of thermomechanically processed S500MC streel grade. He selected commercial TMP S500MC steel plates with dimensions of $6.8mm \times 100mm \times 300mm$ for this study. Five strategies were pursued by varying the inductor position with respect to the laser beam. The sample designations were defined according to the CO_2 LBW strategy: without induction heating (A); and subjected to

pre-heating (B); post-heating (C); combined pre- and post- heating (D); and induction annealing after cooling the weld seam(E). Vicker microhardness tester was used to get micro hardness line profiles averaged over the top, middle and bottom of the plates for each welding strategy. The obtained results indicated that laser welded sample without any induction heating provoked marked hardening of the FZ and HAZ. The increase of hardness within the FZ and HAZ was caused by the predominantly martensitic/bainitic microstructures formed without induction heating. A hardness increase of about 200HV and 150HV was observed for samples (F) and (A), respectively. Martensite formation could be suppressed within the FZ and HAZ and smooth hardness distributions were obtained by pre-heating and combined pre-and post-heating.

Evaluation the microstructure, hardness and tensile properties of fiber laser welded (FLW) joints on high strength low alloy (HSLA) and dual-phase (DP980) steel in similar and dissimilar material combinations was carried out by Parkes et al. [23]. Microstructural study was carried out by using a light microscope attached with Clemex image analysis system software and with a scanning electron microscope (SEM). The micrographs of HSLA-HSLA revealed martensitic structure with a lathy morphology in the FZ. While the FZ of DP980-DP980 contained highly martensitic structure which was attributed to the high cooling rate involved in the FLW and also to the higher harden ability of DP980 steel as a result of the higher content of manganese and carbon. The micrograph taken from the center of the FZ in the dissimilar welded joints indicated the formation of martensitic structure. While a soft zone occurred on the DP980 side, it was absent on the HSLA side. Hardness profile across the dissimilar welded joint exhibited an asymmetric characteristic with a higher hardness on the DP980 side and a lower hardness on the HSLA side. In particular, hardness drop was observed in soft zone appeared on the DP980 side, but it was absent on the HSLA side. It was seen that both the HSLA-HSLA welded joint and the HSLA side of the dissimilar HSLA-DP980 welded joint had a similar trend of hardness variation with a constant and uniform BM hardness followed by a sharp increase through the HAZ up into the FZ. The engineering stress strain curves of the similar HSLA-HSLA and DP980-DP980, and dissimilar HSLA-DP980 welded joints were obtained at $1 \times 10^{-3} s^{-1}$. The YS, UTS and strain to failure of the similar HSLA-HSLA welded joints after FLW were observed to be very close to those of the BM. While lower strain to failure of DP980-DP980 welded joints was observed but the UTS was very close to that of the DP980 BM indicating a high joint efficiency. In the dissimilar HSLA-DP980 welded joints, the YS and UTS were remarkably below those of the similar DP980-DP980 welded joints but they were same as those of the HSLA BM or similar HSLA-HSLA welded joints.

The rate dependent mechanical properties, deformation and fracture behavior of DP600 steel and its welded joint produced by Nd:YAG laser over a wide range of strain rates had been presented by Dong et al. [24] Micrographs of welded DP600 were obtained by using SEM and Vicker hardness tester was used to get hardness profile across the welded sample. The microhardness of the FZ becomes higher because of fully martensite microstructure in this zone. Just outside the FZ, fine martensite and undesolved ferrite microstructures were found in the HAZ. The local microhardness drops below the BM microhardness in the outer HAZ. This is also known as softened zone which is adjacent to the unaffected BM.

Ahmed et al. [25] used two commercially available types of steels, DP and TRIP, in his work. Bead-on-plate DP600/DP600, TRIP700/TRIP700 and DP600/TRIP700 steel sheet welds were produced with 6 kW CW CO_2 beam laser. He observed that in DP/DP steel weldments, the average of maximum hardness which achieved in FZ was 350±30 HV and represents 1.75 times of DP steel base metal hardness. The martensite structure allowed the weld metal and HAZ near the weld metal to have the maximum hardness, and the decrease in the hardness of HAZ near the base metal results from relatively soft ferrite having a low hardness. In TRIP/TRIP steel weldments, the average of maximum hardness which was present in FZ was 500±30 HV and represented

1.92 times of TRIP steel base metal hardness. FZ microstructure of this configuration consisted of ferrite and martensite due to the high aluminum content. In DP/TRIP steel weldments, the average FZ hardness in DP600 sheets was 410±10 (2.05 times of DP steel base metal hardness) and in TRIP700 sheets was 450±20 HV (1.73 times of TRIP steel base metal hardness).
A new failure for laser welded regions under combined normal and shear loading conditions had been proposed by Ha et al. [26] The failure criteria was basically divided into base metal failure and interfacial failure. Experiments were performed in nine different loading directions including the normal loading and pure shear loading directions to get failure criteria. The experimental results revealed that the shear failure load increased as the normal failure load decreased with increase of the loading angle in case of base metal failure. The transition point was observed around a loading angle of 75 degree due to the change in the failure mode from base metal failure to interfacial failure. The shear failure load decreased as the normal failure load decreased with increase of the loading angle in case of the interfacial failure.

1.4 Numerical modeling of laser beam welding

1.4.1 3D FE solid modeling of laser welding

Due to the complex welded joint geometry and its three-dimensional nature, it is very difficult to obtain governing equations for predicting the metallurgical and mechanical properties of laser welded joints. The experimental predictions are time consuming and expensive. To overcome these problems, the finite element (FE) method is increasingly used in recent decades. Some outstanding developments of FE analysis of laser welding have been accompanied by scientific research such as at Queen's University (Canada) [27,28], National Institute of Technology (India) [29,30], University of Paderborn (Germany) [31,32], etc.
An accurate knowledge of the laser welding process is important for predicting the metallurgical and mechanical properties of the laser welded joints. It is very difficult to get insight into the joint during laser welding process. The effective way to analyze welded joint during forming process is to perform FE simulation. The FE simulations of the laser welding processes enables estimation of different process parameters such as weld pool geometry, transient temperature, stresses, and distortion. The FE simulation is not an easy task since it involves the interaction of thermal, mechanical, and metallurgical phenomena.
For having a knowledge of the recent progress in FE analysis of the laser welding, published work in recent years relating to the FE analysis of the laser welding is reviewed in this section. The FE analysis of laser beam welding process was carried out by Lacki and Adamus [33] with the ADINA System v.8.6. The obtained results allow for determination of both the material properties, and stress and strain state in the joint. Turna et al.'s work [34] presented a numerical simulation of thermal and stress fields in welding tubes made of austenitic stainless CrNi steel type AISI 304 with a pulsed Nd:YAG laser. The achieved results of numerical simulation were almost identical with a real weldment thermally affected by welding process. To improve the nonhomogeneity of dissimilar alloys laser welding, relative uniform energy distribution of laser beam and appropriate groove were attempted by Chen et al. [35]. The effects of these attempts on the nonhomogeneity of interfacial reactions were investigated by FE numerical simulation and experimental validation. Tensile test results showed that the combination of rectangular spot laser welding- brazing and V-shaped groove can effectively control the fracture of Ti/Al joints in the seam in a wide processing parameters window.
Both boundary conditions and metal phase transformations have influence on the levels of the residual stress in the weld process. The effect of metallurgical phase transformations upon the residual stresses and distortions induced by laser beam welding in a T-joint configuration was

investigated by Zain-ul-abdein et al. [36] using the FE method. Two separate models were studied using different FE codes, where the first one describes a thermo-mechanical analysis using ABAQUS; while the second one discusses a thermo-metallo-mechanical analysis using SYSWELD. A comparative analysis of experimentally validated FE models has been performed and the residual stress states with and without the metallurgical phase transformations are predicted. A FE model of pulsed laser welding for Zircaloy-4 plate was developed by Han et al. [37] for incorporating the phase transitions and the dynamic material properties with transient temperature. The parametric study presented that the welding induced distortions are highly dependent on the geometry of the molten zone and the heat affected zone (HAZ).

Montalvo-Urquizo et al. [38] presented a coupled simulation of the thermal and mechanical problems of the laser welding process. The mechanical model included the thermo-elasto-plastic solution, required for the residual state computation. The implementation was done using the Adaptive-FEM Toolbox ALBERTA, making use of a posteriori error estimation for the proper adaption of the mesh with respect to the moving heat source. In Salonitis et al.'s article [39], a modeling strategy for the penetration laser welding was presented. The simulation was exploited for selecting process parameters that will not harm the internal layer of the sandwich material. Based on the experimental verification, strategies and guidelines for the successful welding of such materials were discussed. Numerical simulations and multifactor regression were used by Yu et al. [40] to investigate how the three process parameters, laser power, spot radius, and spot offset, influence the temperature distribution in Beryllium (Be) cylindrical shells. The experiments were designed by the compound response surface method. The results could provide guidelines for welding process of Be materials.

The residual stress for AISI 4047 bead-on-plate samples were measured by Casalino et al. [41] using strain gage method after laser welding with different values for the laser speed and power, and focus height. The residual stresses were calculated by means of a nonlinear FE analysis. The analysis took in account the thermomechanical phenomena with temperature dependent steel properties. A 3D conical Gaussian heat source was employed by Balasubramanian et al. [42] for performing nonlinear thermal analysis of laser beam welding of AISI 304austenitic stainless steel. The transient temperature profile and weld bead dimensions, depth of penetration, and bead width were calculated by FE simulation.

Kuppuswamy et. al. [43] studied finite element modeling of impact strength of laser welds for automotive applications. They discussed in their study, the laser welding modeling techniques, including element selection, choice of material models for the weld etc. Owing to the huge surface area of BIW, the element sizes used varying between 3.5 mm to 6 mm. Most of the elements were shell elements. The total number of elements could touch close to one million. Visco-plastic steel material model was used for the upper and lower flanges. But the substitute weld has been tested with both elastic-nonlinear visco-plastic and also bilinear elastic-plastic models. These are inbuilt material models in LS Dyna commercial FE software known through keywords MAT24 and MAT100, respectively. The type and dimension of the weld model was fixed and validated on experimental crash test results. An empirical relationship was then developed which covers the numerous physical effects like sheet thickness, static and dynamic strength and failure behavior of the joint. A general description of the model and some recommendations for application of the model where coarse meshes were involved for both welds and flanges were given as well.

1.4.2 Enrichment techniques

Finite element enrichment technique named interpolation covers method has been developed recently by Kim and Bathe. The solution accuracy of the traditional low-order finite element can be increased without mesh refinement. Higher order enrichment is used to improve the stresses

without introducing additional nodes in the element. The authors have developed MITC3 shell finite element enriched by interpolation covers method and have shown the stress improvement and good convergence behavior even when distorted meshes are used. The enrichment scheme not only captures higher gradients but also decreases inter-element stress jumps [44–46].
The extended finite element method (XFEM) is used as enrichment technique. The XFEM method basically uses heaviside functions for enrichment purpose as they are relatively simple to implement and do not require the highly accurate quadrature rules needed to handle analytic or higher-order polynomial enrichment functions. The XFEM enrichment by heaviside functions is applicable to weak and strong discontinuities [47–49]. Curved surfaces and interfaces can be represented implicitly by the iso-zero values of a level set function and without explicitly mesh boundaries [50, 61]. The XFEM formulation can also be used to represent non-smooth displacement field resulted from a yield line and to capture the elasto-plastic behavior of a plate by very few elements [52].
Hybrid-Trefftz displacement method is used to develop perforated plate super element. An original 8-node plate element containing a hole has been selected for the study. Special trial functions derived from Kolosov Muskhel- ishvili complex variable formulation are the priori solutions of the governing equations. By doing so, the problem is reduced from interior domain integrals to boundary integrals. The study shows that super element can capture high stress gradient without mesh refinement and shows good agreement with the reference solution. The aim of this study is to develop super elements to model rupture initiation in rivited assemblies at low computational cost [53–56].
Variable singularity power wedge element to capture singular stress fields due to local failures in multimaterial composites is developed by Ugo Icardi [57]. The aim of this study is to develop a new mixed singular wedge element based on interpolation functions with a variable singularity power which can adapt to the problem. The displacements and the interlaminar stresses are considered as nodal degrees of freedom. The accuracy of this element is assessed after application on sample cases with singular stress fields due to dissimilar properties of materials, geometry or cracks. The numerical results demonstrated that this element is capable to predict accurately the presence and the nature of singularities, the related stress fields and the participation of the singular stresses [57–60].
Interface enriched generalized finite element method (IGFEM) is used for 3D problems with discontinuous gradient fields. In this method, the generalized degrees of freedom are assigned to the interface nodes when creating integration subdomains unlikely in conventional GFEM where the generalized degrees of freedom (dofs) are assigned to the nodes of the original mesh. A linear combination of the Lagrangian shape functions in these integration subelements are then used as the enrichment functions to capture the discontinuity in the gradient field [61–63].
The nodal point force based finite element method for linear static stress calculations in finite element analysis is presented by Daniel Jose Payen [64]. Element nodal point forces are used in establishing the stiffness matrix rather than the stress assumption employed. Finite element stress predictions are improved at low computational cost. The nodal point force based stress calculation method uses the principles of virtual work in the form of boundary tractions and in the form of internal stresses [64–68].
The mixed formulation based on the Hu-Washizu principle is developed to improve stresses [69]. Low order displacement based finite elements are being focused because they provide good convergence due to low computational cost. This stress improvement procedure can be used in static, dynamic and nonlinear solutions [69–72].
Arlequin method is used to couple two different mechanical states to conduct multiscale modeling [73–76]. This is a straightforward unified method for calculating coupling matrices. Arlequin method can couple two different mechanical states through reliable coupling operators as well as

consistent energy distribution between the two coupling zones.The Arlequin user elements have been systematically developed, enabling a successful integration of the Arlequin method with the ABAQUS platform. To show the flexibility of the method and its application to multiscale modeling, numerical results of 2D-2D, 1D-2D, 1D-3D and 2D-3D coupling examples are presented and accurate results are obtained after comparing with very fine mesh [77].

All reviewed stress improvement techniques are compared by putting them all in matrix of decision in Figure 1.1.

Criteria / Methods	Implementation in Lsdyna	Computational efficiency	Adaptation to explicit dynamics	Nonlinear	Accuracy	Degree of complexity
Interpolation covers	!	✓	!	!	✓	✓
XFEM	!	!	!	!	✓	!
Variable singularity power	!	✗	!	!	✓	!
Hybrid-Trefftz displacement method	!	✓	!	✗	✓	!
IGFEM	!	✗	!	!	!	!
Nodal point force	!	!	!	!	✓	!
Mixed variational formulation	!	!	✓	✓	✓	✗
Arlequin	!	✗	!	✓	✓	!

Figure 1.1: Matrix of decision.

Interpolation covers method can improve the stresses without any local mesh refinement. Method can handle dynamic and non-linear problems. Good solution accuracy can be obtained at low computational cost. XFEM is able to model material discontinuities. Formulation still valid for elastic problems and only few new papers show its applicability on elasto-plastic plates. Accuracy depends on the number of integration points and basis functions. Computational time is high if compare with coarse mesh in case of elasto-plastic plate problems. In variable singularity power method, generalized degrees of freedom are assigned to interface nodes. Implementation in Ls-Dyna may not be very easy because element is divided according to interface geometry. Reasonable accuracy can be achieved. Computational cost is high because very fine mesh requires to capture gradient discontinuity. Hybrid-Trefftz displacement method can not be adopted to solve non-linear structures and difficult to extend to explicit dynamic problems. In IGFEM, generalized degrees of freedom are assigned to interface nodes. Implementation in Ls-Dyna may not be very easy because element is divided according to interface geometry. Reasonable accuracy can be achieved. Method can be extended to dynamic and non linear problems. Computational cost is high because very fine mesh requires to capture gradient discontinuity. NPF method can give good solution accuracy and stresses can be improved at relatively low computational cost. Mixed variational formulation method can enhance the solution accuracy at reasonable computational cost. This method can be used to solve non-linear and dynamic problems but degree of complexity is high.Arlequin method can couple two different mechanical states through reliable coupling operators. Method can solve non-linear problems and can be extended to handle explicit dynamic problems. Implementation in LS Dyna and computational cost of this method is not per our requirements.

After reviewing all the solution improvement methods, interpolation covers method has been selected due to good compromise on accuracy and computational cost.

1.4.3 Damage models

The micro mechanical model by Gurson–Tvergaard–Needleman is widely used for the prediction of ductile fracture. An elastic-plastic material model that accounts for the nucleation and growth of microscopic voids in a ductile metal has been developed by Gurson [78, 79]. Analyses of the influence of microscopic voids on plastic flow have been carried out on the basis of a set of approximate constitutive relations. In this material model the voids are represented in terms of a single parameter, the void volume fraction, and the voids give rise to an apparent dilatancy and pressure sensitivity of the macroscopic plastic deformations [80]. Needleman and Tvergaard investigated the ductile crack growth based on Gurson model. They modeled the fracture as a natural outcome of deformation process due to possibility of complete loss of load carrying capacity due to large void growth. They have shown experimental and numerical analysis of cup-cone fracture in a round tensile test specimen based on a set of elastic-plastic constitutive relations that account for the nucleation, growth and coalescence of micro-voids [81–83].

Metal deformation and rupture under impact loading is a complex and dynamic process, always involving high plastic strains as well as large changes in strain rates [84]. Johnson-Cook material model [85] is a popular constitutive relation for metals, widely used in simulation of impact and penetration related problems [87–90, 145]. The popularity is more due to the simple form of the equation and the relative ease of determination of the model constants [91]. The Johnson-Cook constitutive model is phenomenological model that reproduces several important material responses observed in impact and penetration of metals. The three key material responses are hardening, strain rate effects and thermal softening [92]. The fracture criterion proposed by Hancock and Mackenzie [143] has been extended by Johnson and Cook [145] to make the failure strain sensitive to stress triaxiality, temperature, strain rate and the strain path. The model assumes that damage accumulates in the material element during plastic straining which accelerates immediately when the damage reaches a critical value. To effectively apply the Johnson-Cook fracture model, researchers extended the model in different ways. Liu et al. [94] proved that Johnson-Cook fracture model can be used as damage initiation coupled with damage evolution in metal cutting simulations. Moreover, the damage evolution combines the two different fracture modes effects. Bao and Wierzbicki [146] extended the Johnson-Cook fracture model in their fracture locus so that the part with high stress triaxiality is similar to Johnson-Cook fracture model while the other parts are expressed in different ways.

The phenomenological cumulative-strain-damage model is developed by Wilkins [96]. This model assumes that fracture is the result of the history of strain damage to the material. Two important factors which are hydrostatic tension and asymmetric strain are considered to enhance the strain damage. The Wilkins damage based on the ductility destruction theory proposed by McClintock [97] that the rupture occurs due to the damage that depends on the strain. Hydrostatic tension accounts for the growth of holes in fracture by spalling, in which the loading consists of large triaxial stress and small strain. Asymmetric strain accounts for the observation that the elongation before failure decreases as the shear load increases in fracture tests with combined stress loads. The cumulative damage formulation by Wilkins is implemented in the numerical simulation code Ls-dyna [98]. Papadrakakis et al. [99] and Yamasaki et al. [100] used and validated the Wilkins damage model for the material modeling of an Aluminum cast alloy. Feucht et al. [101] applied Wilkins model to describe the damage behavior and failure in crash simulations of Aluminum die cast alloy and in a high strength steel.

The damage model GISSMO (Generalised Incremental Stress State dependent damage MOdel), describes the damage evolution and failure of sheet metal. The phenomenological damage model GISSMO was proposed by Neukamm et al. [102–104] in order to bridge the gap between metal forming and crash worthiness simulations. This damage model is the fruit of an ambitious

cooperative effort between Daimler AG and Dynamore GmbH [102–108]. In metal forming simulations, the classical models such Forming Limit Diagrams usually predict relatively bad results. Therefore the damage model GISSMO is formulated as an incremental continuum damage model. In crash worthiness simulations, usually isotropic models such as J_2-plasticity are used. On the other hand in metal forming more sophisticated anisotropic yield loci are considered. Thus it is necessary to use different constitutive laws in the process chain. The damage model GISSMO is used both in metal forming and crash worthiness simulations simultaneously with constitutive plasticity models. The fracture strain is defined as a function of stress triaxiality in this damage model. Basaran M. [109] proposed the extension of the GISSMO damage/failure model to also account for the Lode angle dependence. He also introduced instability variable and coupling of damage with plasticity in the GISSMO damage model. Andrade et al. [110] has adopted the GISSMO damage/failure model to describe the failure behavior of a dual-phase steel (DP800) and showed that the GISSMO damage/failure model is a useful option to predict accurate failure after comparing results with experimental and Gurson damage model in his studies.

1.5 Aim of the present thesis

The objective of the present thesis is to develop a specific FE shell model in order to be able to simulate accurately the complex behavior of a laser welding line within an industrial context i.e. using a coarse shell mesh. Therefore the developments concern the following points.

- The new multimaterial element should be able to capture stress/plastic strain gradients accurately at the vicinity of laser welded line.
- It should be able to show the physical deformation of welded sections.
- It should be fast enough to be used in the industrial environment.
- It should be also capable to predict failure accurately.

1.6 Outline of the thesis

The present thesis manuscript consists of four chapters.

- General state of the art of laser beam welding technology, its main defects, the effects of microstructure, aim of the present thesis and a description of numerical modeling techniques for laser welded structures.
- In chapter 2, the problem statement of laser beam welding is exposed through different aspects of the industrial benchmark WSII. Here will be exposed difference between "*Solid Refine Model*" (SRM) and "*Shell Coarse Model*" (SCM) within the WSII benchmark. Detailed description of WSII modeling will be given such as boundary and loading conditions, contact interfaces, elements and their mesh sizes etc. Finally local and global numerical results of SRM and SCM are compared and evaluated.
- Chapter 3 presents the developed User Shell Element within Ls-dyna commercial software and based on the famous MITC4 shell element. A new strain enhancement using a quadratic approximation through the thickness has been introduced to improve stress state has been developed. Then, will be exposed the adopted procedure for the enrichment of our User element (UEL) using the Interpolation Covers Method (ICM), important features of the User element and its corresponding Ls-dyna card, will be also detailed.

- Chapter 4 is dedicated to the detailed description of the multimaterial user model and the corresponding UMAT. Indeed a ductile damage model involving both BM and HAZ materials in the same UMAT treatment will be described. Numerical applications related to the laser welding problem have been treated. More precisely, a two-beam bending application and the WSII benchmark have been analyzed using the developed User Element and their result comparisons will be discussed in this chapter. Some other important practical points regarding the preprocessing stage will be detailed e.g. preparation of Ls-dyna key file to select the best input parameters for the UEL/UMAT model to insure good results quality.

- In chapter 5, conclusion of this technical report is presented as well as some perspectives for possible future work are drawn.

Laser welding modeling statement

The objective of this chapter is to present the statement of the numerical modeling of laser welded line, while keeping into mind always the industrial concerns i.e. the use of very coarse shell mesh to achieve good solution!
In fact during a car crash accident the car seat will be subjected to very high loading which may involve large elasto-plastic strains and damage in all the welded metallic parts which constitute the car seat. It has been observed that the general behavior of the subsystems becomes quickly very highly nonlinear and its numerical solution may not be obtained using the classical implicit algorithms, because of difficulty in obtaining convergence.
Therefore, in our investigation, the Explicit Dynamics time integration formulation has been chosen to solve the mechanical problem of a welded subsystem submitted to severe loading. The first section is dedicated to the recall of necessary equations for the Explicit Dynamics time integration formulation, using the finite element method. The second section deals with the description of the laser welding modeling used at Faurecia Automotive seating, using the standard WSII benchmark. Discrepancy of results between the reference "*Solid Refine Model*" (SRM) and the "*Shell Coarse Model*" (SCM) will be discussed. Finally some important remarks and conclusions will be drawn concerning the necessary improvements needed for the SCM to enhance the quality of its results. This target represents the main objective of the present research investigation.

2.1 Explicit dynamics time integration

The study of impact and more generally dynamic loading problems, is a task which requires skills in both mechanics (large strains, anisotropic elasto-plastic behavior, contact, high strain rates, etc.) and also in numerical simulation (numerical analysis, resolution algorithms, Convergence, etc.). From the theoretical point of view, many academic research teams and industrials are actively working on this topic. The themes addressed in numerous international conferences (DYMAT, ICLLS, ECOMAS, SILS, etc.) and the development of commercial finite element codes (Ls-dyna, Pam-Crash, Radioss, Dytran, Abaqus Explicit, Autodyn, etc.) reveal the diversity of activities in this field and the complexity of the combined physical phenomena. Numerical simulation allows the qualitative and quantitative evaluation of the behavior of the welded parts by the identification and the prediction of these phenomena.
Various spatial discretization schemes are possible while using the finite element method [111]. The great majority (if not all) of commercial finite element programs use the updated Lagrangian formulation, where all variables are referred to the current (i.e. from the end of the previous time step) configuration of the system [112–115]. Therefore, Cauchy stress and Almansi (or logarithmic) strain are used. The advantage of this approach is the simplicity of incremental strain description. The disadvantage is that all derivatives with respect to spatial co-ordinates must be recomputed in each time step, because the reference configuration is changing.

In implicit methods, the equations of dynamics are combined with the time integration operator, and the displacements are found directly. In explicit methods, on the other hand, at first the accelerations are determined from the equations of dynamics and then integrated to obtain the displacements. The most commonly used implicit integration methods, such as the Newmarks' constant acceleration method, are unconditionally stable [111]. This implies that their time step is limited only by the convergence/accuracy considerations. However, the implicit methods require solution of a set of non-linear algebraic equations at each time step. Furthermore, iterations need to be performed for each time step of implicit integration to control the error and prevent divergence. Therefore, the number of numerical operations per each time step can be three orders of magnitude larger than for explicit integration [116]. Thus, 'the advantage of implicit method for three-dimensional (transient) problems becomes marginal' [111]. On the other hand, in explicit methods, such as the central difference method, treatment of non-linearities is very straightforward and no iterations are required.
Whatever the procedure chosen, the objective of any study is the search for a state of equilibrium at time t, which can be defined in variational form from the principle of virtual works:

$$\int_V \delta\boldsymbol{\varepsilon}^T \boldsymbol{\sigma} dV = \int_S \delta\boldsymbol{u}^T \boldsymbol{f}_s dS + \int_V \delta\boldsymbol{u}^T (\boldsymbol{f_b} - \rho\ddot{\boldsymbol{u}}) dV \qquad \forall\, \delta\boldsymbol{u}\ K.A. \tag{2.1}$$

where $\boldsymbol{\sigma}$ is the Cauchy stress tensor, $\delta\boldsymbol{\varepsilon}$ is the virtual strain tensor, $\boldsymbol{f}_s$ is the surface load vector, $\boldsymbol{f}_b$ is the body load vector, $\delta\boldsymbol{u}$ is the virtual displacement vector, ρ is the material density and $\ddot{\boldsymbol{u}}$ the acceleration vector.
The resolution of 2.1 is based on a spatial discretization of the domain. The movements (real and virtual) as well as the accelerations, of any point can be defined respectively from the displacements (real and virtual) and the accelerations to the nodes using interpolation functions:

$$\begin{aligned} \boldsymbol{u} &= \mathbb{N}\,\boldsymbol{u_n} \\ \delta\boldsymbol{u} &= \mathbb{N}\,\delta\boldsymbol{u}_n \\ \ddot{\boldsymbol{u}} &= \mathbb{N}\,\ddot{\boldsymbol{u}}_{\boldsymbol{n}} \end{aligned} \tag{2.2}$$

with $\boldsymbol{u}_n$ and $\delta\boldsymbol{u}_n$ the real and virtual element nodal degrees of freedom respectively and $\mathbb{N}$ is the finite element approximation matrix. The virtual strains are defined by

$$\delta\boldsymbol{\varepsilon} = \mathbb{B}\,\delta\boldsymbol{u_n} \tag{2.3}$$

where $\mathbb{B}$ is the strain matrix which depends on the geometry at time t and of type of finite element model (shell, solid, etc.).
Using the previous equations, the discretized equilibrium equation can be obtained on each element, as follows

$$\sum_{e=1}^{nelt} \left(\int_{V^e} \delta\boldsymbol{u}_n^T\, \mathbb{B}^T\, \boldsymbol{\sigma}\, dV - \int_{S^e} \delta\boldsymbol{u}_n^T\, \mathbb{N}^T\, \boldsymbol{f}_s\, dS - \int_{V^e} \delta\boldsymbol{u}_n^T\, \mathbb{N}^T\, (\boldsymbol{f_b} - \rho\, \ddot{\boldsymbol{u}})\, dV \right) = 0 \tag{2.4}$$

where S^e and V^e are the element surface and volume respectively.
Using the notions of element internal force $\boldsymbol{f}^e_{int}$, element external force $\boldsymbol{f}^e_{ext}$ and element mass matrix $\boldsymbol{M}^e$, equation 2.4 can be written as follows:

$$\sum_{e=1}^{nelt} \delta\boldsymbol{u}_n^T\, (\boldsymbol{f}^e_{int} - \boldsymbol{f}^e_{ext} + \mathbb{M}^e\, \ddot{\boldsymbol{u}}_{\boldsymbol{n}}) = 0 \qquad \forall\, \delta\boldsymbol{u}_n \neq \boldsymbol{0} \tag{2.5}$$

with

$$\begin{aligned} \boldsymbol{f}^e_{int} &= \int_{V^e} \mathbb{B}^T \boldsymbol{\sigma}\, dV \\ \boldsymbol{f}^e_{ext} &= \int_{S^e} \mathbb{N}^T \boldsymbol{f}_s\, dS + \int_{V^e} \mathbb{N}^T \boldsymbol{f_b}\, dV \\ \mathbb{M}^e &= \int_{V^e} \mathbb{N}^T \rho\, \mathbb{N}\, dV \end{aligned} \tag{2.6}$$

After assembly, the system of equations can be derived easily.

$$\mathbb{M}\,\ddot{\boldsymbol{U}} = \boldsymbol{F_{ext}} - \boldsymbol{F_{int}} \tag{2.7}$$

where $\mathbb{M} = \sum_{e=1}^{nelt} \mathbb{M}^e$ is the global mass matrix usually diagonal, $\boldsymbol{F_{ext}} = \sum_{e=1}^{nelt} \boldsymbol{f}^e_{ext}$ is the global external force vector, $\boldsymbol{F_{int}} = \sum_{e=1}^{nelt} \boldsymbol{f}^e_{int}$ is the global internal force vector.
Usually two extra force vectors are added to equation 2.7, namely the anti-hourglassing force vector $\boldsymbol{F_{hrg}}$ and the contact force vector $\boldsymbol{F_{ctc}}$, so that the general expression of the discretized equilibrium system of equation leads to

$$\mathbb{M}\,\ddot{\boldsymbol{U}} = \boldsymbol{F_{ext}} - \boldsymbol{F_{int}} + \boldsymbol{F_{hrg}} + \boldsymbol{F_{ctc}} \tag{2.8}$$

Several commercial codes use the Explicit Dynamics resolution method (Ls-dyna, Pam-crash, Radioss, Abaqus Explicit, etc.). We chose to use the EF Ls-dyna commercial code, because it is the main code used at Faurecia Automotive Seating for crash simulation and also because it allows an easy programming interface using FORTRAN language.
Equation 2.8 is written for any time t^n corresponding to a step n. In order to move forward to the next time step $n+1$, generally the central difference time integration is used:

$$\begin{aligned} \ddot{\boldsymbol{U}}^n &= \mathbb{M}^{-1}\left(\boldsymbol{F}^n_{\boldsymbol{ext}} - \boldsymbol{F}^n_{\boldsymbol{int}} + \boldsymbol{F}^n_{\boldsymbol{hrg}} + \boldsymbol{F}^n_{\boldsymbol{ctc}}\right) \\ \dot{\boldsymbol{U}}^{n+1/2} &= \dot{\boldsymbol{U}}^{n-1/2} + \ddot{\boldsymbol{U}}\,\Delta t^n \\ \boldsymbol{U}^{n+1} &= \boldsymbol{U}^n + \dot{\boldsymbol{U}}^{n+1/2}\,\Delta t^{n+1/2} \end{aligned} \tag{2.9}$$

with time step $\Delta t^{n+1/2} = \dfrac{\Delta t^n + \Delta t^{n+1}}{2}$.
The deformed geometry of the next step $n+1$ is obtained by summing the total displacement vector to the coordinates of the initial mesh.

$$\boldsymbol{X}^{n+1} = \boldsymbol{X}^0 + \boldsymbol{U}^{n+1} \tag{2.10}$$

It is important to notice that dynamic relaxation allows approximating solution to converge towards the quasi-static state. This can be achieved by introducing the damping forces into dynamic equilibrium system of equations, which reads

$$\mathbb{M}\,\ddot{\boldsymbol{U}}^n + \mathbb{C}\,\dot{\boldsymbol{U}}^n + \boldsymbol{Q}^n(\boldsymbol{U}) = \boldsymbol{0} \tag{2.11}$$

with $\boldsymbol{Q}^n(\boldsymbol{U}) = \boldsymbol{F}^n_{\boldsymbol{int}} - \boldsymbol{F}^n_{\boldsymbol{ext}} - \boldsymbol{F}^n_{\boldsymbol{hrg}} - \boldsymbol{F}^n_{\boldsymbol{ctc}}$ and $\mathbb{C}$ is the damping matrix. The damping is not only necessary because of the numerical actions to reduce the computation time but also to ensure fast convergence of the solution towards the static solution describing the actual process. With Δt as the fixed time increment we get for the central difference scheme

$$\dot{\boldsymbol{U}}^{n+1/2} = \frac{\boldsymbol{U}^{n+1} - \boldsymbol{U}^{n}}{\Delta t}; \qquad \ddot{\boldsymbol{U}} = \frac{\dot{\boldsymbol{U}}^{n+1/2} - \dot{\boldsymbol{U}}^{n-1/2}}{\Delta t} \tag{2.12}$$

For he velocity at time t^n we usually assume an averaged value, as follows

$$\dot{\boldsymbol{U}}^{n} = \frac{\dot{\boldsymbol{U}}^{n+1/2} + \dot{\boldsymbol{U}}^{n-1/2}}{2} \tag{2.13}$$

Therefore we can obtain the final updating equation of solution, for the next time t^{n+1}.

$$\dot{\boldsymbol{U}}^{n+1/2} = \left(\frac{1}{\Delta t}\mathbb{M} + \frac{1}{2}\mathbb{C}\right)^{-1}\left(\frac{1}{\Delta t}\mathbb{M} - \frac{1}{2}\mathbb{C}\right)\dot{\boldsymbol{U}}^{n-1/2} - \boldsymbol{Q}^{n} \tag{2.14}$$

$$\boldsymbol{U}^{n+1} = \boldsymbol{U}^{n} + \Delta t\,\dot{\boldsymbol{U}}^{n+1/2} \tag{2.15}$$

In order to preserve the explicit form of the central difference integrator, $\mathbb{M}$ and $\mathbb{C}$ are always kept diagonal for computational efficiency. Further reductions of the computation time per increment of time step from utilization of reduced integration schemes that are often applied even to the deviatoric parts of the stiffness matrix, and finally numerical actions related to mass scaling and load factoring contribute.

The analogy between the dynamic equilibrium equation and the ideal mass-spring vibrating system allows concluding that explicit central difference time integration schemes (frequently referred as explicit integration schemes) are conditionally stable whenever the size of the increment of time Δt satisfies the COURANT condition [117]:

$$\Delta t \leq \Delta t_c = \frac{L^e}{c^e} = \frac{L^e}{\sqrt{E/\rho}} \tag{2.16}$$

where L^e is the smallest size of all the finite element mesh through the discretized domain, E is the Young's modulus and c^e is the longitudinal sound wave speed propagation into the material. Normally a severe restriction on the time step size has to be included in order to receive satisfactory simulation results. For example, in impact and crash simulations conducted with explicit solvers the time step is usually in the order of magnitude of microseconds or even tenths of microseconds [118].

2.2 Experimental analysis and modeling of WSII subsystem

2.2.1 Brief presentation of Arcan experiment

The Arcan experimental setup is used for the mechanical characterization of material using different loading conditions with the same device. The Arcan test consists of a fixture jig that allows for simultaneous combined shear and tension loading on a tensile test machine [131]. It also provides an angular adjustment of results to different shear and tension configuration. The original Arcan test presents a specimen with a bow tie shape that is directly attached by bolt screws [131].

Experimental procedures have been developed to test a specimen in pure tension (mode I) and pure shear (mode II) loads and in mixed mode I/II loads [131, 132]. The Arcan test was firstly developed by Arcan et al. [131–134] to study and characterise the damage behaviour of composite materials. Other problems such as crack propagation in metal plates have been studied with this type of tests by Sutton et al. [135, 136]. Spot weld failure under combined loading conditions was examined by Lin S.H. et al. [137–139]. Arcan experimental set-up enables one to mix and control tensile and shear loads as shown in Figure 2.1. The angular position, between the the

(a) Peeling load at an angle of $0^\circ/0^\circ$.

(b) Zoom on peeling load at an angle of $0^\circ/0^\circ$.

(c) Peeling load at an angle of $0^\circ/45^\circ$.

Figure 2.1: Lase welded specimen under peeling load in Arcan test experimental set-up.

disk quarter and the load direction, defines exactly the tensile/shear ratio. Varying this angular position leads to several load combinations. The global load is applied to the centre.

2.2.2 Experimental results of Arcan test

In the current study, the investigation is limited to the peeling test at an angle of $0^\circ/0^\circ$ as shown in Figure 2.1(a). Numerous experiments have been conducted by Faurecia to get load-displacement curves of welding sub system WSII as shown in Figure 2.2. For the sack of comparison with the numerical FE models, mean experimental curve is used as depicted in the Figure 2.3.

2.2.3 Description of WSII benchmark

Welding sub system WSII has been devised by Faurecia Automotive Seating to study the influence of welding parameters on its strength and also to validate their finite element models, namely the "*Solid Refine Model*" (SRM) and the "*Shell Coarse Model*" (SCM). WSII is a welding

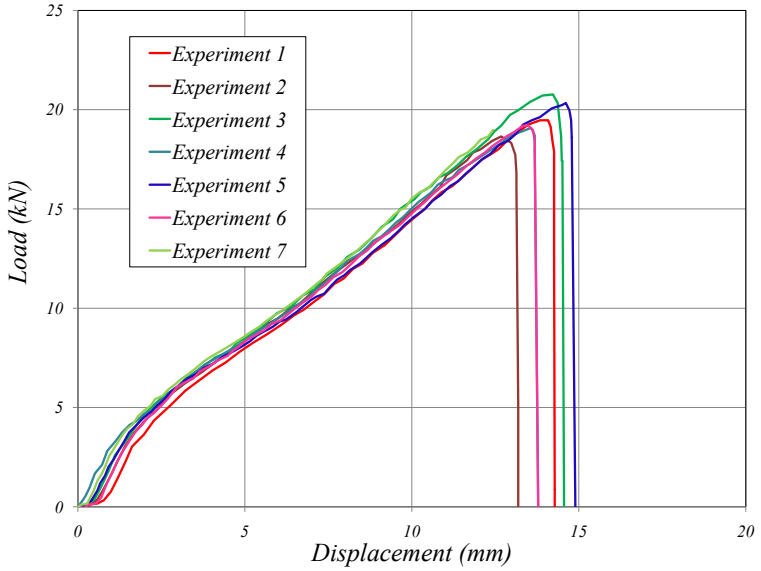

Figure 2.2: Experimental load-displacement curves of welding sub system WSII.

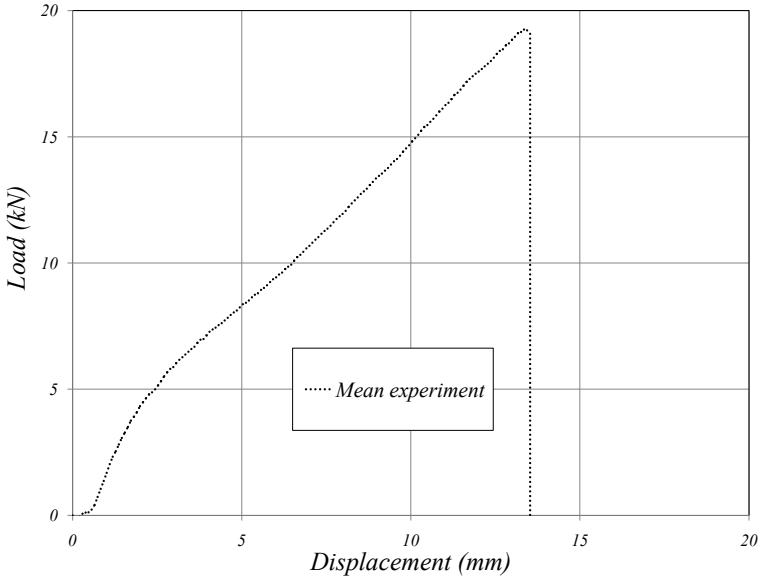

Figure 2.3: Mean experimental load-displacement curves of welding sub system WSII.

benchmark in which two U-shaped metallic sheets of same or different materials are welded as shown in 2.4. In the following a modeling analysis of WSII using two different material namely the $S500$ and $S420$ steels are joined by welding process. The two U-shaped joined steel sheets $S500$ and $S420$ have thickness of $2.5mm$ and $1.8mm$ receptively. Full Arcan test set up is shown in Figure 2.4.

Laser weld line consists of three different kind of zones namely, Base Material (BM), Heat Affected Zone (HAZ) and Melted Zone (MZ). Weld line having three different zones with element size 0.2mm are illustrated in Figure 2.6.

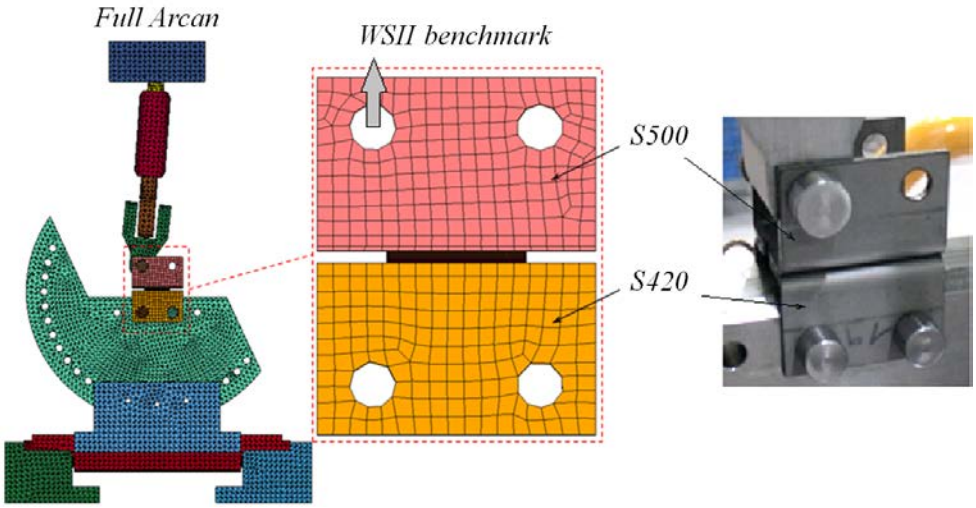

Figure 2.4: Numerical model of Arcan test and zoom on WSII welding benchmark.

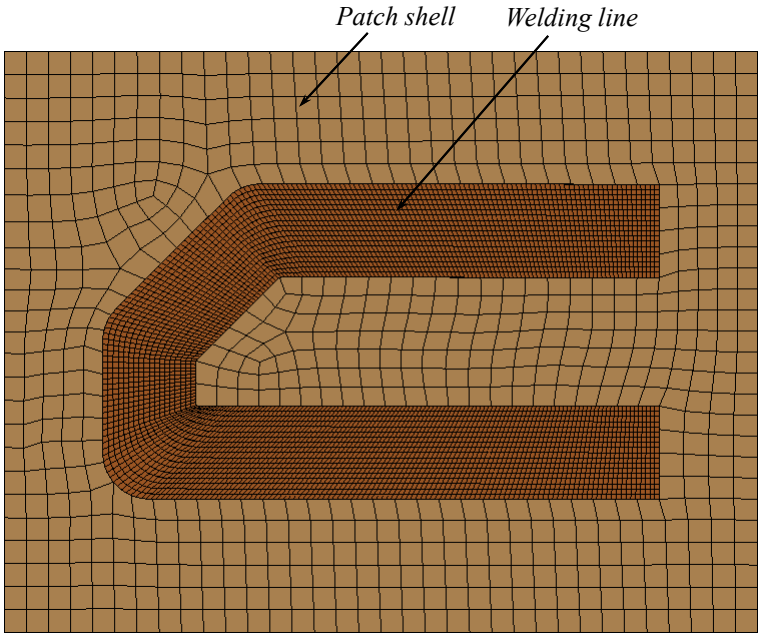

Figure 2.5: Patch shell with laser welding line.

2.2.4 Numerical modeling of WSII

Faurecia Automotive Seating has developed and proposed two FE models to analyze laser welded joints in a support of car seat. These two models are the "*Solid Refine Model*" (call SRM) and the "*Shell Coarse Model*" (called SCM). The SRM will be used as a reference model since it uses a refine solid hexahedral mesh and the welding area is correctly represented using several elements in the sheet metallic thickness (Figure 2.7). The SCM is our target model, which we will try to improve since it uses a very coarse shell mesh and does not take into account correctly the HAZ (Figure 2.9).

The SRM is modeled by using 3D solid elements and it shows realistic representation of welding sections e.g. melted zone (MZ), heat affected zone (HAZ) and base material (BM). Cross section of welding line of solid refined model is represented in Figure 2.7. The mesh size has been

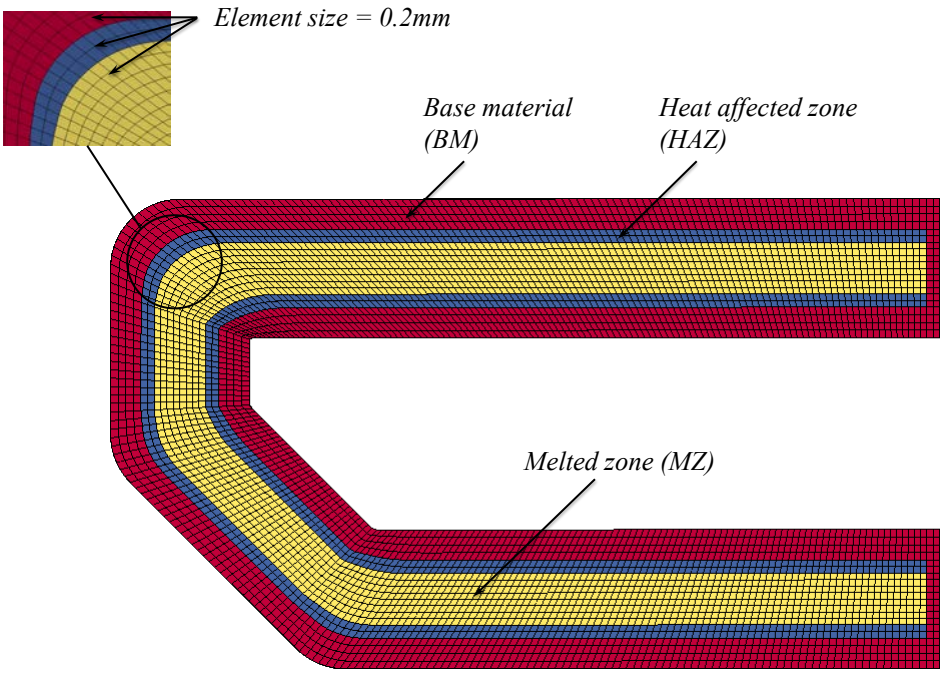

Figure 2.6: Weld line with BM, HAZ and MZ.

chosen to have a minimum of 2 elements ($0.2mm$ size of each element) through HAZ width. Figure 2.8 shows the section cut of solid refined model WSII, where the solid and shell elements are connected through tied contact. This model is able to represent global behavior of welded connection as well as it gives reliable information of the local welding deformation or rupture. The drawbacl use such king of modeling ı

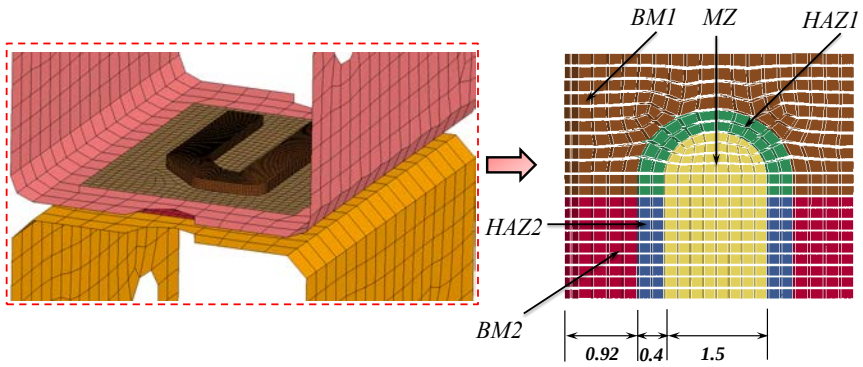

Figure 2.7: Cross section of solid refine model.

The SCM is built of shell elements with a coarse mesh size of $1.5mm$ in the transition area and in the MZ. Figure 2.9 shows the cross section of the SCM where the MZ shell elements share nodes with the elastic solid element. This classical model is able to represent global behavior of the welded connection, but it is not able to capture accurately stresses and plastic strain locally at the interface between BM and HAZ. This kind of modeling has been imposed by Faurecia Automotive Seating with the objective to enhance its behavior to make it able to

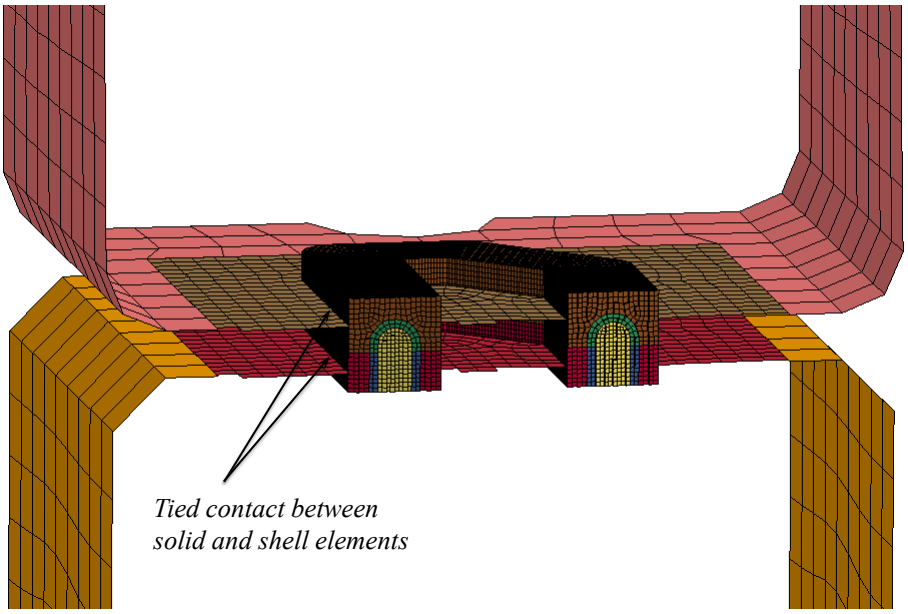

Figure 2.8: Tied contact between solid and shell elements.

predict accurately the complex behavior of the WSII under dynamic loading.

For the calculations, MPP Ls-dyna 971 R6.1.2 version with 2 CPU's is used. Table 2.1 illustrates the total number of elements used to model solid refined and shell coarse models with and without Arcan machir -

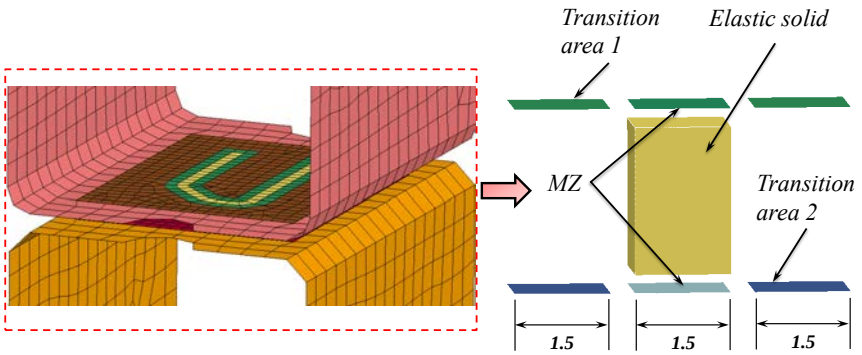

Figure 2.9: Cross section of shell coarse model.

Table 2.1: Soild refine vs shell coarse models.

Models	Full Arcan (no. of elements)	Without Arcan (no. of elements)
Solid refine	237889	106438
Shell coarse	133264	1813

2.2.4.1 Loading and boundary conditions

The studied configuration of WSII concerns the peeling case, where a $0.2m/s$ velocity is applied on one bolt on the top of the Arcan to pull the specimen apart. Velocity imposed curve is given in Figure 2.10. Where we can observe, initially during first $5ms$ no velocity is applied, then a linear increase of velocity is applied until the top speed of $0.2m/s$ is reached at $20ms$ of time. Then the velocity is maintained constant during all the simulation process, until the end time of $80ms$.

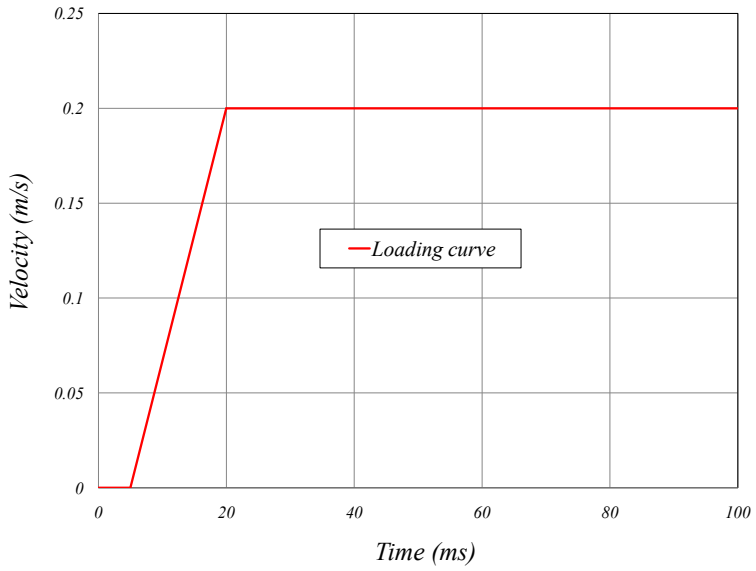

Figure 2.10: Input loading curve.

On the other hand, the WSII is considered fixed at the bottom side of $S420$ metallic sheet which is attached by the two bolts as shown in Figure 2.4. It has to be noticed, that when using the Faurecia supplied models SRM and SCM, we could obtain good solutions only when using the Massively Parallel Processing (MPP) version of Ls-dyna 971 R6.1.2. Indeed the Shared Memory Processing (SMP) version of Ls-dyna 971 R6.1.2 gave always a noised non feasible response of the full Arcan. Therefore for the remaining, all our developments have been done within the MPP Ls-dyna 971 R6.1.2 version, available in our Laboratory.

2.2.4.2 Materials description used in WSII

In the welding line, basically five different materials are used: 2 HAZ, 2BM and 1 FZ. The five material data were introduced using Ls-dyna material card `*MAT_PIECEWISE_LINEAR_PLASTICITY`. The basic common material data are the Young's modulus $E = 210GPa$, Poisson ratio $\nu = 0.3$, density $\rho = 7850kg/m^3$. Here it is assumed only isotropic hardening effects for all the materials, and the hardening curves for the five materials are shown in Figure 2.11. To reproduce local behaviour, material of each zone has to be identified. BM is characterized by classical traction test. Material is considered as fully isotropic, as a consequence the plasticity is given by the classical von Mises criteria. For two others MZ and HAZ materials, the characterization is more complex. The only material information currently available is the micro vicker hardness along a welding cross section. As a first assumption, HAZ and MZ materials are directly derived from base material and hardness test values.
Generalized incremental stress state dependent damage model (GISSMO) of Ls-dyna has been

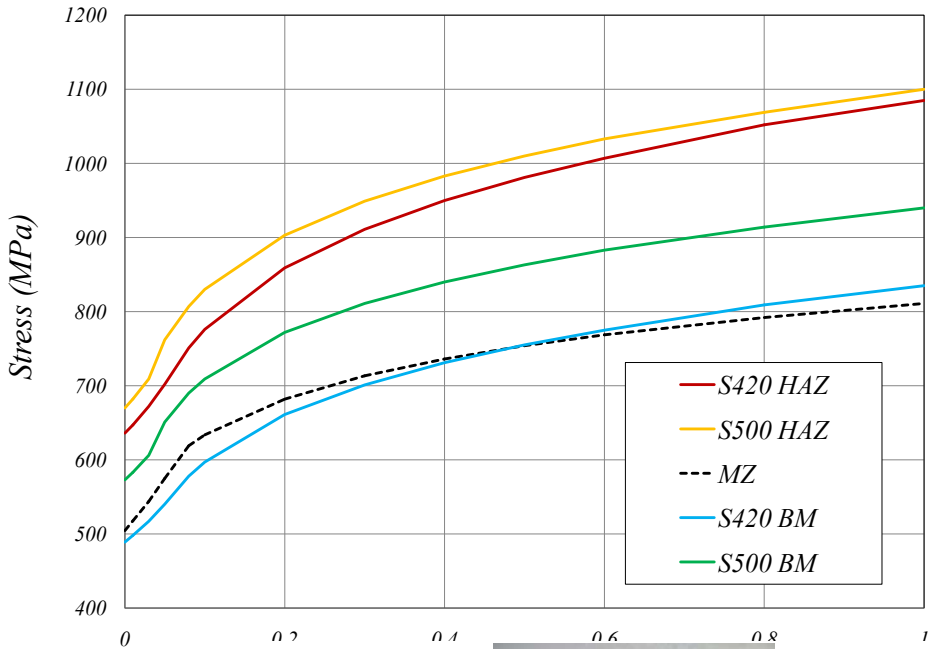

selected to predict the failu
was selected to use the pre
It has to be noticed that
failure has occurred exper
2.12.

(a) Deformed WSII.

(b) Zoom on deformed WSII.

Figure 2.12: Deformed WSII using experiments : failure occurs in the HAZ on the side of S500.

Therefore, it has been identified experimentally a failure surface of the material HAZ $S500$, which depends on the triaxiality and on Lode parameter, as shown in Figure 2.13.

2.2.4.3 Solution control

Numerical simulation was carried using the explicit solver. Mass scaling option to reduce CPU time was also used from Ls-dyna control time step card as it can be seen in Figure 2.14.
In Figure 2.14, DT2MS represents time step size for mass scaled solutions.

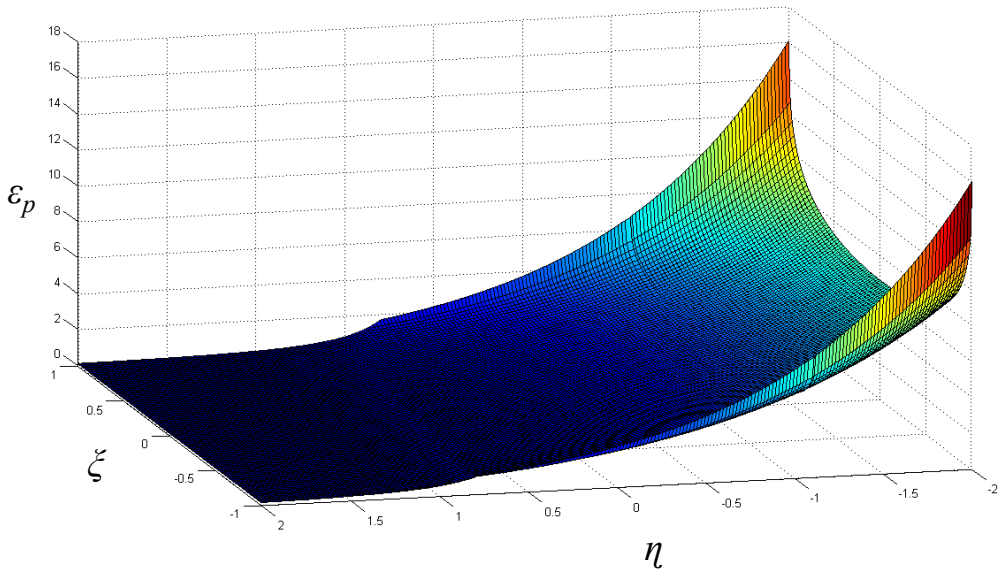

Figure 2.13: Fracture surface of HAZ S500 in 3D space.

```
*CONTROL_TIMESTEP
$$   DTINIT    TSSFAC      ISDO    TSLIMT     DT2MS      LCTM     ERODE     MSIST
     0.000  0.900000         0     0.000 -6.000E-4         0         0         0
$#   DT2MSF   DT2MSLC     IMSCL    UNUSED    UNUSED     RMSCL
     0.000         0         0                         0.000


*CONTROL_SHELL
$    WRPANG     ESORT     IRNXX    ISTUPD    THEORY       BWC     MITER      PROJ
 70.000000         1         0         4        16         1         1         0
$   ROTASCL    INTGRD   LAMSHT    CSTYP6    TSHELL
     0.000         1         0         0         0
$   PSSTUPD   SIDT4TU    CNTCO   ITSFLG   IRQUAD
         0         0         0         0         2
```

Figure 2.14: Control time step card of Ls-dyna.

Figure 2.15 shows the control shell card of Ls-dyna where INTGRD is set to 1, it means Lobatto inte
Inte
in t
Figu

```
*CONTROL_TIMESTEP
$$   DTINIT    TSSFAC      ISDO    TSLIMT     DT2MS      LCTM     ERODE     MSIST
     0.000  0.900000         0     0.000 -6.000E-4         0         0         0
$#   DT2MSF   DT2MSLC     IMSCL    UNUSED    UNUSED     RMSCL
     0.000         0         0                         0.000


*CONTROL_SHELL
$    WRPANG     ESORT     IRNXX    ISTUPD    THEORY       BWC     MITER      PROJ
 70.000000         1         0         4        16         1         1         0
$   ROTASCL    INTGRD   LAMSHT    CSTYP6    TSHELL
     0.000         1         0         0         0
$   PSSTUPD   SIDT4TU    CNTCO   ITSFLG   IRQUAD
         0         0         0         0         2
$    NFAIL1    NFAIL4   PSNFAIL   KEEPCS    DELFR   DRCPSID    DRCPRM
         0         0         0         0         0         0     0.000

*SECTION_SHELL_TITLE
S500_SHELL_1.8MM
$     SECID    ELFORM      SHRF       NIP     PROPT   QR/IRID    ICOMP    SETYP
         1        16  0.833300         5  1.000000     0.000        0        1
$       T1        T2        T3        T4      NLOC   MAREA      IDOF   EDGSET
 1.800000  1.800000  1.800000  1.800000     0.000     0.000     0.000        0
```

Figure 2.15: Control shell card of Ls-dyna.

Solid elements ELFORM02 with 0.2mm mesh size were used in the SRM, whereas ELFORM16 shell elements with 1.5mm mesh size were selected for the SCM in the weld line area.

```
*CONTROL_SHELL
$    WRPANG      ESORT      IRNXX     ISTUPD     THEORY        BWC     MITER      PROJ
 70.000000          1          0          4         16          1         1         0
$   ROTASCL     INTGRD     LAMSHT     CSTYP6     TSHELL
      0.000          1          0          0          0
$   PSSTUPD    SIDT4TU      CNTCO     ITSFLG     IRQUAD
          0          0          0          0          2
$    NFAIL1     NFAIL4    PSNFAIL     KEEPCS      DELFR    DRCPSID     DRCPRM
          0          0          0          0          0          0      0.000

*SECTION_SHELL_TITLE
S500_SHELL_1.8MM
$     SECID     ELFORM       SHRF        NIP      PROPT    QR/IRID     ICOMP     SETYP
          1         16   0.833300          5  1.000000      0.000         0         1
$        T1         T2         T3         T4       NLOC      MAREA      IDOF    EDGSET
   1.800000   1.800000   1.800000   1.800000      0.000      0.000     0.000         0
```

Figure 2.16: Shell section card of Ls-dyna.

2.2.4.4 Contact treatment

Automatic surface to surface contact was used between BM $S420$ and BM $S500$ parts using the `*CONTACT_AUTOM`

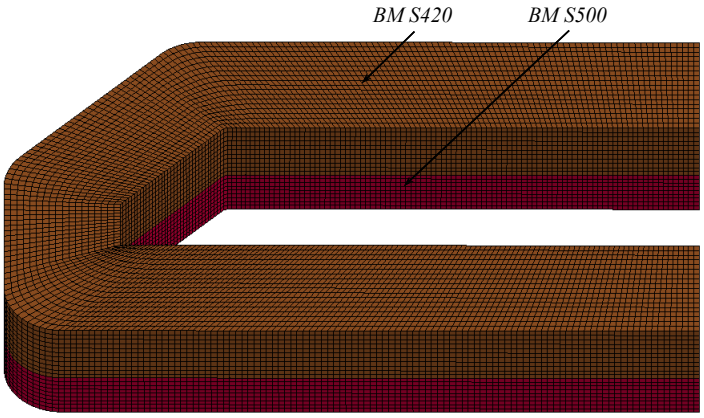

Figure 2.17: Automatic surface to surface contact between BM $S420$ and BM $S500$.

Patch shell set and BM node set were contacted using tied shell edge to surface beam offset contact of Ls-dyna using card `*CONTACT_TIED_SHELL_EDGE_TO_SURFACE_BEAM_OFFSET` as shown in Figure 2.18 and Figure 2.19.

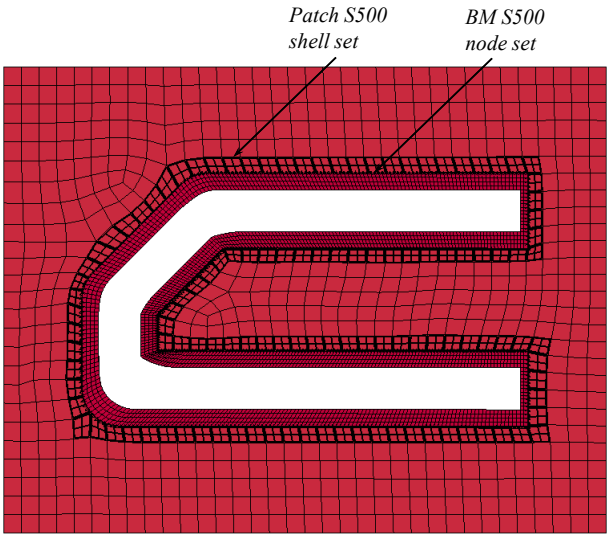

Figure 2.18: Tied contact contact between patch $S500$ shell set and BM $S500$ node set.

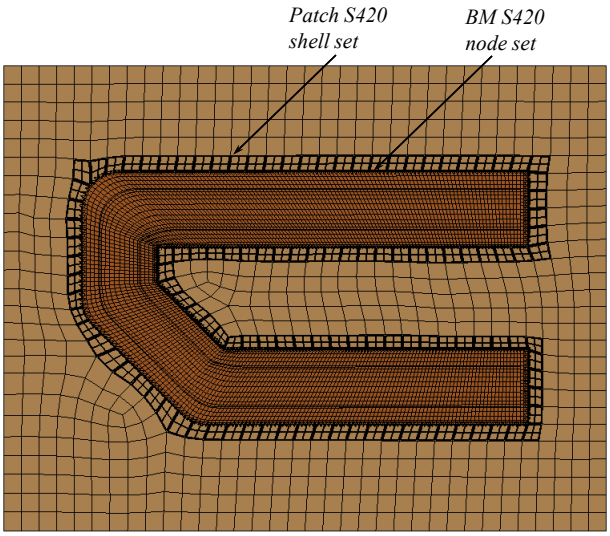

Figure 2.19: Tied contact contact between patch $S420$ shell set and BM $S420$ node set.

Tied shell edge to surface beam offset contact is used between global shape shell set and patch node set and it is presented in Figure 2.20 and Figure 2.21.

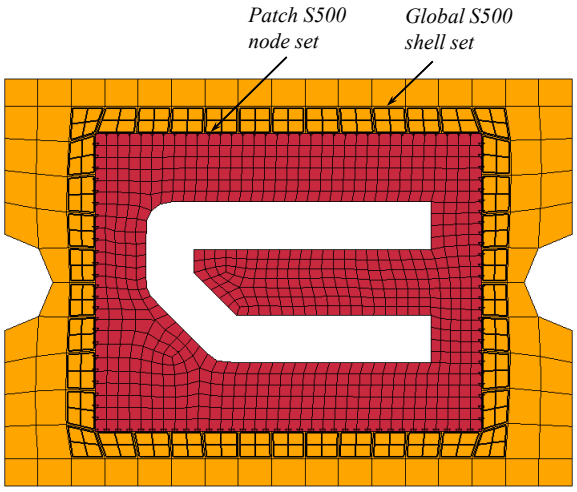

Figure 2.20: Tied contact contact between patch S500 node set and Global shape S500 shell set.

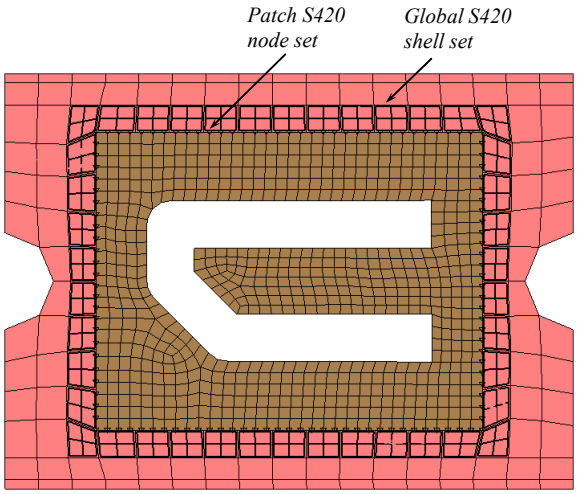

Figure 2.21: Tied contact contact between patch S420 node set and Global shape S420 shell set.

2.2.5 Baseline results comparison: SRM vs. SCM

In the following the results obtained using the FE baseline models supplied initially by Faurecia Automotive Seating company namely the "*Solid Refine Model*" (SRM) and the "*Shell Coarse Model*" (SCM) will be compared and analyzed. The SRM results will be considered as a reference target which the SCM model is supposed to achieve. Due to the nature and complexity of the present benchmark, numerous results are available, therefore, some selected local and global results will be compared and analyzed to assess the advantages and limitations of the SCM.

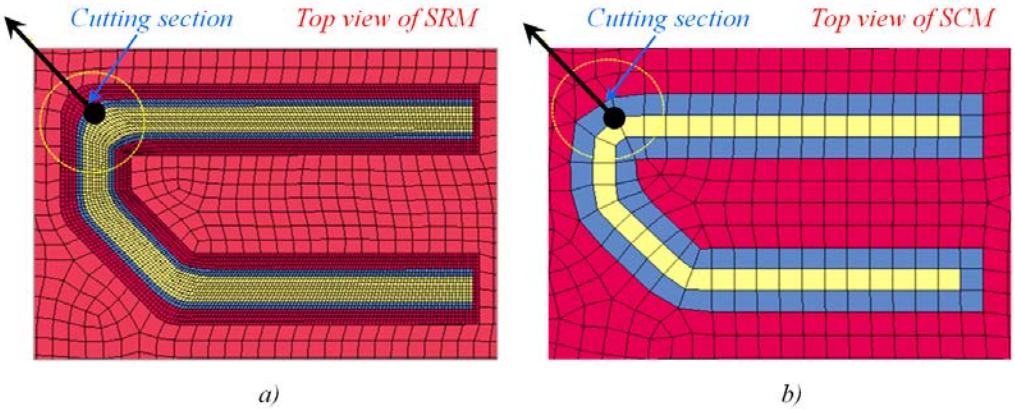

Figure 2.22: Section cut for post-processing: a) SRM, b) SCM.

In order to compare local results in both cases, section cut was taken from corner of the U-shape welded line where stress concentration is expected to be maximum. These section cuts in the SRM and SCM are sown in Figure 2.22.
Post-processing of the stresses was carried out on integration points for the same level of load of $13kN$ and on the $S500$ steel sheet where failure has been observed experimentally. In SCM post-processing of stresses at integration points was not available directly through the graphical interface of Ls-prepost. Therefore we developed a FORTRAN utility subroutine which reads the

ELOUTDET ascii file generated by Ls-dyna code, and extracts the stress results on the desired integration points.
Von-Mises stress contour plots obtained from the SRM reference model as well as the SCM are shown in Figure 2.23 and Figure 2.24, respectively. The arrow tail shows starting point of measuring whereas arrow head shows ending point of curve post-processing.

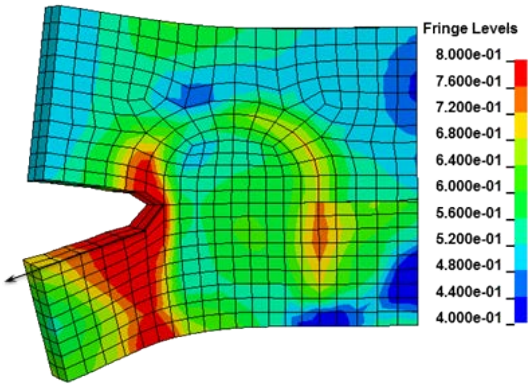

Figure 2.23: Von-Mises stress (GPa) distribution obtained using the SRM at a load of 13kN.

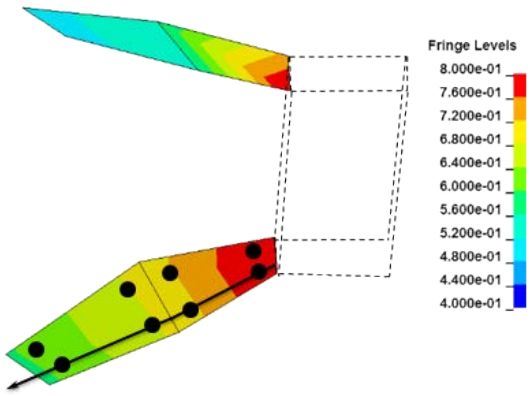

Figure 2.24: Von-Mises stress (GPa) distribution obtained using the SCM at a load of 13kN.

Von-Mises stress comparison graph between results of SRM and SCM is illustrated in Figure 2.25. As one can observe, the SRM is able to capture stress concentration accurately especially in the HAZ where the material is exhibiting more strength than BM. It can be noticed also that SCM fails to capture stress concentration due to the absence of HAZ material with an error percentage of approximately 24%. Indeed in the SCM, only BM and MZ materials are used because the HAZ area is very small and it has been completely removed in this model.
Global results comparison was carried out in terms of load-displacement curve between SRM and experimental results as shown in Figure 2.26. As one can observe, the SRM model is predicting accurately the ultimate load for the welded line in the WSII. We can also observe good tendency of load evolution between the numerical and the experimental curves, with a slightly stiff numerical solution which may due to the mesh refinement.
Failure in the SRM has been predicted accurately thanks to the GISSMO damage model available in Ls-dyna. Figure 2.27(a) shows the final deformed WSII after failure, whereas Figure 2.27(b) shows the SCM deformed shape where no failure can be observed even if the load is increased artificially.

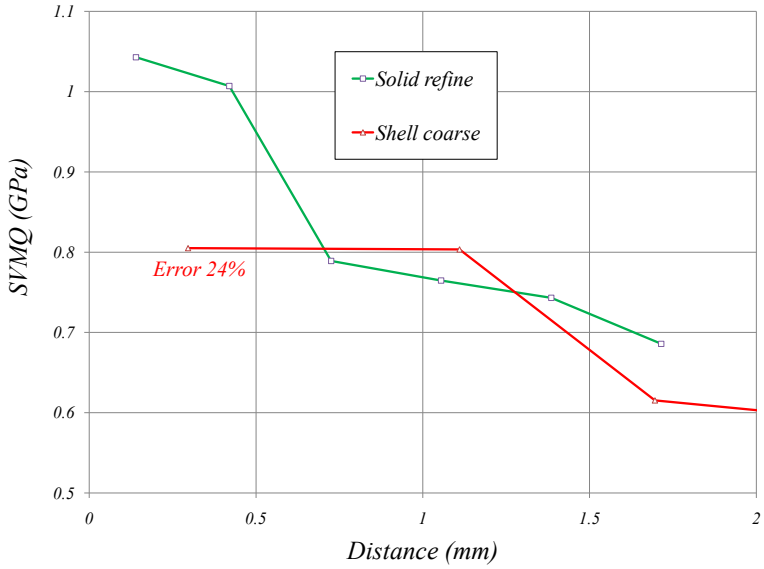

Figure 2.25: Von-Mises stress comparison : SRM vs. SCM for the same load of 13kN.

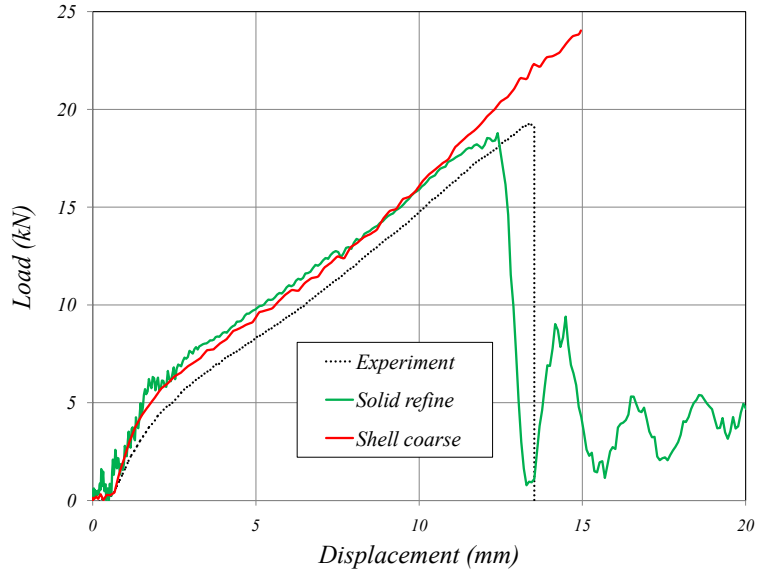

Figure 2.26: Load-displacement curve comparison between solid refine and experimental results.

2.3 Concluding remarks

At the beginning of this chapter a general formulation for the modeling of an impact or crash problem has been presented using the Explicit Dynamics time integration. A brief overview of Arcan Experiment was discussed, using fixture jig which allows to conduct experiments in pure shear, pure tensile as well as in mixed mode by adjusting angular configuration.
Faurecia Automotive Seating company has developed a dedicated subsystem for laser welding known as WSII welding subsystem. The purpose of this development is to compare the influence of welding parameters on its ultimate strength and also to evaluate the efficiency of various FE modeling through the use of simple welding specimens.
Two different kinds of FE laser welded models proposed by Faurecia Automotive Seating com-

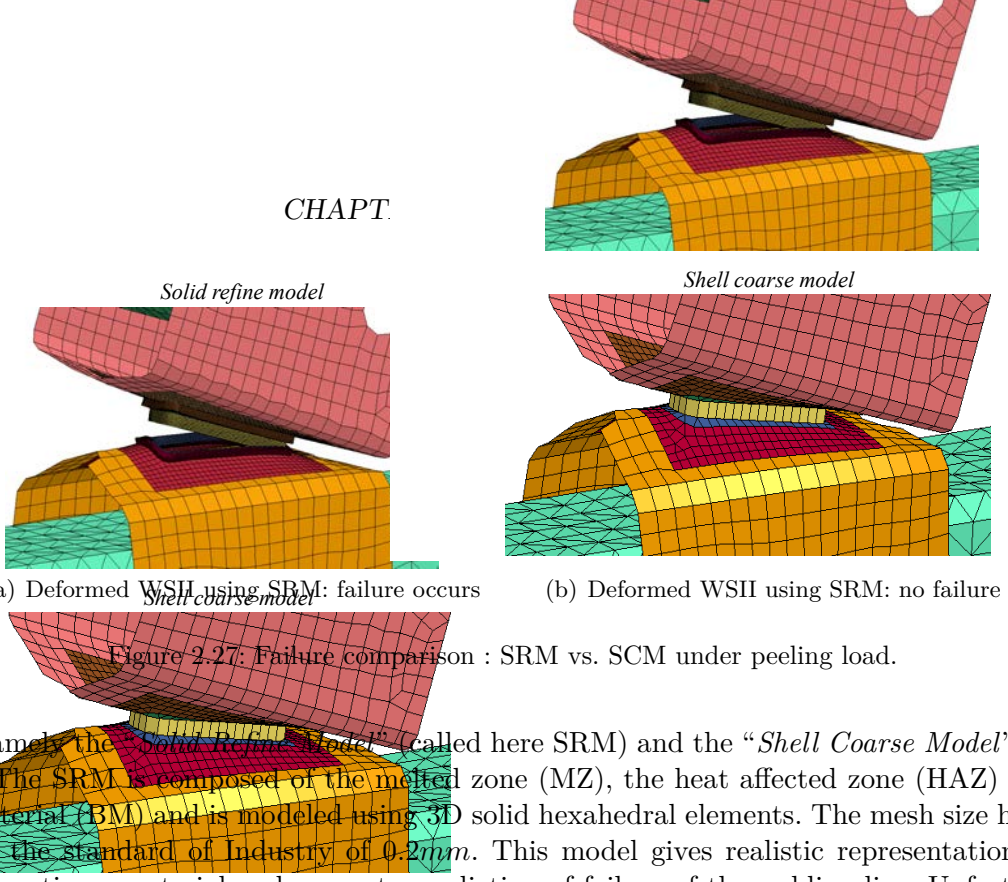

(a) Deformed WSII using SRM: failure occurs (b) Deformed WSII using SRM: no failure

Figure 2.27: Failure comparison : SRM vs. SCM under peeling load.

pany, namely the "*Solid Refine Model*" (called here SRM) and the "*Shell Coarse Model*" (called SCM). The SRM is composed of the melted zone (MZ), the heat affected zone (HAZ) and the base material (BM) and is modeled using 3D solid hexahedral elements. The mesh size has been fixed to the standard of Industry of $0.2mm$. This model gives realistic representation of the welding sections, material and accurate prediction of failure of the welding line. Unfortunately due to its high computing costs, the SRM cannot be used in a full seat for a front car crash simulation.

In order to address the issue of numerical computation time, the SCM has been developed which is modeled by 2D shell elements. The element size follows the industry standards of $1.5mm$ to be able to use it in a full car seat during crash simulation. Unfortunately, the SCM cannot be used in its baseline version as shown in this chapter, because it is not able to capture high stress gradient accurately especially in the vicinity of welding line at the interface between the BM and the HAZ and hence cannot predict failure accurately.

Therefore, the objective of the present investigation will the enhancement of the SCM through the development of special enriched FE shell model in order to be able to simulate accurately the complex behavior of a laser welding line within an industrial context i.e. using a coarse shell mesh of $1.5mm$ size. The main steps of developments which will be described in the next chapters, concern the following points:

- In chapter 3, will be shown the development of an efficient shell element enriched using a newly developed method called the interpolation covers method. This development will be discussed in details and some academic applications will be treated to show the efficiency of the proposed shell enriched element.

- In chapter 4, a multimaterial model linked to the previously developed shell element will be presented. The multimaterial model allows the use of only one shell element to represent both BM and HAZ areas, using discontinuous Heaviside functions. A generalized stress based damage model is also implemented within Ls-dyna commercial code to allow the User shell element to predict the failure of the welded line in WSII benchmark.

Proposal of an enriched Shell Element

This chapter describes the formulation of an improved version of shell element based on the famous and efficient four-node shell element called MITC4. At first the original formulation of the MITC4 shell element is presented. Then a new enhancement based on a quadratic approximation of strains is introduced to improve stress distribution. At the end the improved developed shell element will be enriched using a numerical method introduced recently by Bathe [44, 46] and called the "*Interpolation Covers Method*" (ICM). The ICM is capable of increasing the FE interpolation degree without adding extra degrees of freedom, by using the surrounding nodes of the target element. Important features and preparation of Ls-dyna User ELement (UEL) will be also presented. Some academic numerical application will be treated to show the efficiency of the proposed procedure.

3.1 General assumptions

Shell elements are still nowadays very important in the modeling of thin flexible structures. Their efficient performance ratio of lightweight/strength has rendered their use widespread in numerous fields of engineering applications. To a large extent, shell structures are now solved in practice using 4-node shell elements. Among those available, the MITC4 shell element is probably one of the most effective elements, in particular when linear and nonlinear analyses are to be performed. The formulation is based on the Reissner–Mindlin theory taking into account shearing stresses while assuming plane stress condition. In this theory, "material fibers originally straight and normal to the shell mid-surface do not stretch and remain straight" and "zero stress normal to the shell mid-surface".
This section is devoted to a detailed description of a quadrilateral shell element having four nodes and six degrees of freedom per node with a quadratic representation through the thickness of strains/stresses. This element can be used for the analysis of thin and thick shells including thickness stretch for large elasto-plastic strains. The main characteristics of the present element are:

- The geometry of a shell is presented by a set of curve facets with four non-necessary coplanar nodes. The position vectors $\boldsymbol{x}_p$ of the mid-surface are continuous, but the normal directions are discontinuous from an element to another.
- Plane stress condition is applied, leading to a zero stress through thickness $\sigma_{zz} = 0$. However shearing stresses are taken into account and are denoted by σ_{xz} and σ_{yz}.
- For each element, five degrees of freedom are considered, three local translations u, v, w and two local rotations θ_1, θ_2 by considering that the "*thick fiber*" (defined by $\boldsymbol{n}_i$) is normal to the reference plane of the element to the node i.

- Prior to assembly, the five local degrees of freedom/node $(u, v, w, \theta_1, \theta_2)$ are transformed into the global framework using six degrees of freedom/node $(U, V, W, \theta_X, \theta_Z, \theta_Z)$.

3.1.1 Rigid rotation of a vector

The rotation of an angle θ around the unit vector $\boldsymbol{e} = \{e_X, e_Y, e_Z\}^T$ will bring point q (vector $\boldsymbol{r}$) to point q (point $\boldsymbol{r'}$) as shown in Figure 3.1.

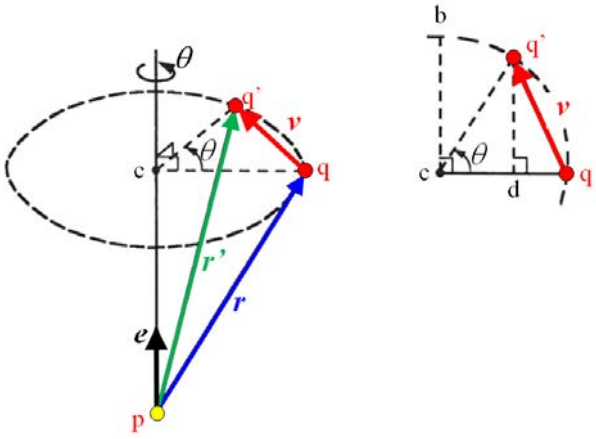

Figure 3.1: Large rigid rotation.

Following Figure 3.1, we have

$$\boldsymbol{r'} = \boldsymbol{r} + \boldsymbol{v} = \boldsymbol{r} + \boldsymbol{e} \wedge \boldsymbol{r} \sin\theta + \boldsymbol{e} \wedge (\boldsymbol{e} \wedge \boldsymbol{r})(1 - \cos\theta) \tag{3.1}$$

By introducing the skew matrix $\mathbb{A}$ ($\mathbb{A}^T = -\mathbb{A}$), it is possible to replace the operand $\boldsymbol{e}\wedge$ and rewrite eq(3.1) in a simpler form

$$\boldsymbol{r'} = \mathbb{Q}\,\boldsymbol{r}; \qquad \text{with} \qquad \mathbb{Q} = \mathbb{I} + \mathbb{A}\,\sin\theta + \mathbb{A}^2\,(1 - \cos\theta) \tag{3.2}$$

and $\mathbb{A} = \begin{bmatrix} 0 & -e_Z & e_Y \\ e_Z & 0 & -e_X \\ -e_Y & e_X & 0 \end{bmatrix}$

For shells, it is necessarily to define a unique orthonormal framework $\mathbb{Q}$ at any point p of the mid-surface having a normal $\boldsymbol{n} = \{n_X, n_Y, n_Z\}^T$. If we consider $\boldsymbol{r} \equiv \boldsymbol{k}$ along $\boldsymbol{Z}$ and $\boldsymbol{r'} \equiv \boldsymbol{n}$, then eq(3.2) leads to $\boldsymbol{n} = \mathbb{Q}\,\boldsymbol{k}$. Now, by choosing $\boldsymbol{e}$ orthogonal to $\boldsymbol{k}$ and to $\boldsymbol{n}$ at the same time, one can obtain the final unique orthonormal basis which will be used in the next sections, it is given by:

$$\mathbb{Q} = \begin{bmatrix} n_Z + \dfrac{n_Y}{1+n_Z} n_Y & -\dfrac{n_X}{1+n_Z} n_Y & n_X \\ -\dfrac{n_Y}{1+n_Z} n_X & n_Z + \dfrac{n_X}{1+n_Z} n_X & n_Y \\ -n_X & -n_Y & n_Z \end{bmatrix} = \begin{bmatrix} \boldsymbol{t}_1 & \vdots & \boldsymbol{t}_2 & \vdots & \boldsymbol{n} \end{bmatrix} \tag{3.3}$$

3.1.2 Kinematics of the shell

The geometry and nodal variables of the 4-node shell element are shown in Figure 3.2 and Figure 3.3, respectively.

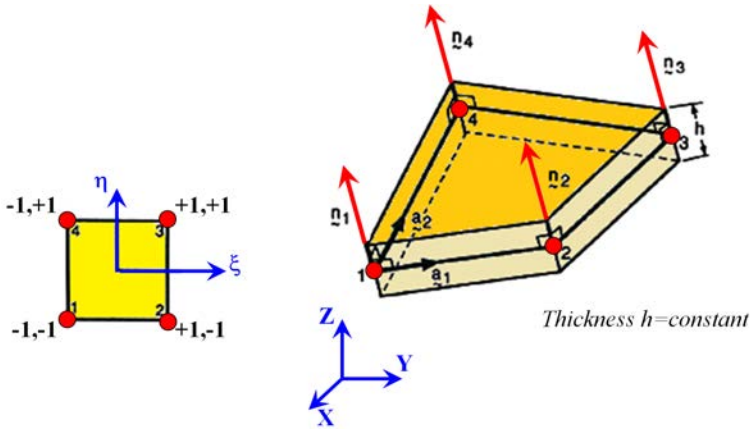

Figure 3.2: Description of the shell element.

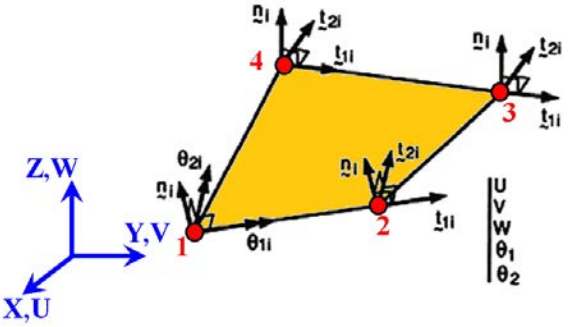

Figure 3.3: Nodal variables (5 local degrees of freedom/node).

$$\boldsymbol{x}_p = \sum_{i=1,4} N_i(\xi,\eta)\boldsymbol{X}_i; \qquad \boldsymbol{X}_i = \{X_i, Y_i, Z_i\}^T \tag{3.4}$$

where X_i , Y_i ,Z_i are cartesian coordinates at node i and $N_i(\xi,\eta)$ are the planar shape functions of the Q4 shell element.

$$N_i(\xi,\eta) = \frac{1}{4}\,(1+\xi_i\,\xi)\,(1+\eta_i\,\eta) \tag{3.5}$$

The virtual displacements (symbol δ) of the quadrilateral shell element are given by:

$$\delta\boldsymbol{u}_q = \delta\boldsymbol{u} + z\;\delta\boldsymbol{\beta} = \sum_{i=1,4} N_i\;\delta\boldsymbol{u}_i + z\;\sum_{i=1,4} N_i\;\left(-\boldsymbol{t}_{2i}\;\delta\theta_{1i} + \boldsymbol{t}_{1i}\;\delta\theta_{2i}\right) \tag{3.6}$$

where $\delta\boldsymbol{u} = \{\delta U, \delta V, \delta W\}^T$ is the virtual translational vector and $\delta\boldsymbol{\beta} = \{\delta\theta_1, \delta\theta_2\}^T$ the virtual rotational vector, which can be written in cartesian components

$$\left\{\begin{array}{c}\delta U_q\\ \delta V_q\\ \delta W_q\end{array}\right\} = \left\{\begin{array}{c}\delta U\\ \delta V\\ \delta W\end{array}\right\} - z\left\{\begin{array}{c}t_{2X}\\ t_{2Y}\\ t_{2Z}\end{array}\right\}\delta\theta_1 + z\left\{\begin{array}{c}t_{1X}\\ t_{1Y}\\ t_{1Z}\end{array}\right\}\delta\theta_2 \tag{3.7}$$

The finite element approximation leads to the matrix form, using nodal degrees of freedom at four nodes.

$$\delta \boldsymbol{u}_q = \mathbb{N}\, \delta \boldsymbol{u}_n; \qquad \delta \boldsymbol{u}_n = \{..., \delta U_i, \delta V_i, \delta W_i, \delta\theta_{1i}, \delta\theta_{2i}, ...\}^T \quad i = 1,4 \tag{3.8}$$

with

$$\mathbb{N}_{3\times 20} = \left[\begin{array}{c|ccc|c|c} \dots & N_i & 0 & 0 & zN_i\boldsymbol{V}_X{}^T & \dots \\ & 0 & N_i & 0 & zN_i\boldsymbol{V}_Y{}^T & \\ & 0 & 0 & N_i & zN_i\boldsymbol{V}_Z{}^T & \end{array}\right] \quad i = 1,4$$

$$\boldsymbol{V}_X = \{-t_{2Xi},\, t_{1Xi}\}^T; \qquad \boldsymbol{V}_Y = \{-t_{2Yi},\, t_{1Yi}\}^T; \qquad \boldsymbol{V}_Z = \{-t_{2Zi},\, t_{1Zi}\}^T$$

The position vector of any point q located at a distance z from the mid-surface of the shell is then derived,

$$\boldsymbol{x}_q = \boldsymbol{x} + z\, \boldsymbol{n}; \qquad \text{with} \quad z = \frac{h}{2}\,\zeta \tag{3.9}$$

On the mid-surface (at $z = 0$), the covariant basis $\mathbb{F}_o$ can be calculated by

$$\mathbb{F}_o = [\ \boldsymbol{a}_1 \ \vdots\ \boldsymbol{a}_2 \ \vdots\ \boldsymbol{n}\ ]; \qquad d\boldsymbol{x} = \mathbb{F}_o\, d\boldsymbol{\xi} \tag{3.10}$$

with $\boldsymbol{a}_1 = \sum_{i=1,4} N_{i,\xi}\boldsymbol{X}_i$, $\boldsymbol{a}_2 = \sum_{i=1,4} N_{i,\eta}\boldsymbol{X}_i$ being the covariant basis vector and $d\boldsymbol{x} = \{dX, dY, dZ\}^T$, $d\boldsymbol{\xi} = \{d\xi, d\eta, d\zeta\}^T$, $\boldsymbol{n} = \dfrac{\boldsymbol{a}}{|\boldsymbol{a}|}$ and $\boldsymbol{a} = \boldsymbol{a}_1 \wedge \boldsymbol{a}_2$.

3.1.3 Virtual strain of the shell

In shell formulation it is natural to define strains and stresses in the curvilinear basis. Therefore the virtual displacement gradient tensor $\delta\mathbb{L}$ in the cartesian coordinate system may be obtained by

$$\delta\mathbb{L} = \mathbb{Q}\, \delta\mathbb{L}_t\, \mathbb{Q}^T = \mathbb{F}_z{}^{-T}\, \delta\mathbb{L}_\xi\, \mathbb{F}_z{}^{-1} \tag{3.11}$$

where $\mathbb{Q}$ is the orthonormal basis given by eq(3.3), $\delta\mathbb{L}_t$ and $\delta\mathbb{L}_\xi$ are the virtual displacement gradient tensor in the curvilinear and the covariant bases respectively and $\mathbb{F}_z$ is the covariant basis for any value of $z \neq 0$ which is given by

$$\mathbb{F}_z = \mathbb{F}_o + z\, \mathbb{F}_n; \qquad \text{with} \quad \mathbb{F}_n = [\ \boldsymbol{n}_{,\xi} \ \vdots\ \boldsymbol{n}_{,\eta} \ \vdots\ \boldsymbol{0}\ ] \tag{3.12}$$

where parametric curvatures are given by $\boldsymbol{n}_{,\xi} = \sum_{i=1,4} N_{i,\xi}\, \boldsymbol{n}_i$ and $\boldsymbol{n}_{,\eta} = \sum_{i=1,4} N_{i,\eta}\, \boldsymbol{n}_i$. The gradient tensor $\mathbb{F}_z$ can be estimated using the following

$$\mathbb{F}_z = \mathbb{F}_o\, (\mathbb{I} + z\, \mathbb{B}_n)\,; \qquad \mathbb{B}_n = \mathbb{F}_o^{-1}\, \mathbb{F}_n \tag{3.13}$$

where $\mathbb{F}_o^{-1} = [\ \boldsymbol{a}^1 \ \vdots\ \boldsymbol{a}^2 \ \vdots\ \boldsymbol{n}\ ]^T$, $\boldsymbol{a}^1 = \dfrac{1}{J_o}\boldsymbol{a}_2 \wedge \boldsymbol{n}$, $\boldsymbol{a}^2 = \dfrac{1}{J_o}\boldsymbol{n} \wedge \boldsymbol{a}_1$ and $J_o = det\,(\mathbb{F}_o)$
The curvature tensor can be approximated by assuming that $\boldsymbol{n} \cdot \boldsymbol{n}_{,\xi} \approx 0$ and $\boldsymbol{n} \cdot \boldsymbol{n}_{,\eta} \approx 0$, to the following

$$\mathbb{B}_n \approx \begin{bmatrix} \boldsymbol{a}^1 \cdot \boldsymbol{n}_{,\xi} & \boldsymbol{a}^1 \cdot \boldsymbol{n}_{,\eta} & 0 \\ \boldsymbol{a}^2 \cdot \boldsymbol{n}_{,\xi} & \boldsymbol{a}^2 \cdot \boldsymbol{n}_{,\eta} & 0 \\ 0 & 0 & 0 \end{bmatrix} \tag{3.14}$$

Using eq(3.13), the inverse of the gradient tensor can be obtained by

$$\mathbb{F}_z^{-1} = \frac{1}{\mu}\left(\hat{\mathbb{I}} + z\,\hat{\mathbb{B}}_z\right)\mathbb{F}_o^{-1} \tag{3.15}$$

where $\hat{\mathbb{I}} = \begin{bmatrix} 1 & 0 & 0 \\ 0 & 1 & 0 \\ 0 & 0 & \mu \end{bmatrix}$, $\hat{\mathbb{B}}_z = \begin{bmatrix} \mathbb{B}_{n22} & -\mathbb{B}_{n12} & 0 \\ -\mathbb{B}_{n21} & \mathbb{B}_{n11} & 0 \\ 0 & 0 & 0 \end{bmatrix}$ and $\mu(z) = 1 - 2zH + z^2K$

with : $2H = -(\mathbb{B}_{n11} + \mathbb{B}_{n22})$ $K = \mathbb{B}_{n11}\,\mathbb{B}_{n22} - \mathbb{B}_{n12}\,\mathbb{B}_{n21}$.

From eq(3.11) one can define the virtual strains $\delta\boldsymbol{\varepsilon}_t$ in the curvilinear basis of the shell as

$$\delta\boldsymbol{\varepsilon}_t = \frac{1}{2}\left(\delta\mathbb{L}_t + \delta\mathbb{L}_t{}^T\right) = \begin{bmatrix} \delta\varepsilon_x & 0.5\,\delta\gamma_{xy} & 0.5\,\delta\gamma_{xz} \\ & \delta\varepsilon_y & 0.5\,\delta\gamma_{yz} \\ sym & & 0 \end{bmatrix} \tag{3.16}$$

In shell formulation, it is usually convenient to split the strain tensor in two parts : the virtual membrane/bending strains $\delta\boldsymbol{\varepsilon}_s$ and the virtual shearing strains $\delta\boldsymbol{\gamma}_s$.

3.1.3.1 Membrane/bending virtual strain

The in-plane virtual strain components can be calculated using eq(3.16) in terms of the displacement gradient $\delta\mathbb{L}_t$

$$\delta\boldsymbol{\varepsilon}_s = \frac{1}{2}\left(\delta\mathbb{L}_s + \delta\mathbb{L}_s{}^T\right) = \begin{bmatrix} \delta\varepsilon_x & 0.5\,\delta\gamma_{xy} \\ & \delta\varepsilon_y \end{bmatrix} \tag{3.17}$$

The components of $\delta\mathbb{L}_t$ relative to the tangent plane $(\boldsymbol{t}_1, \boldsymbol{t}_2)$ are then defined by:

$$\delta\mathbb{L}_s = \begin{bmatrix} \delta\mathbb{L}_{t11} & \delta\mathbb{L}_{t12} \\ \delta\mathbb{L}_{t21} & \delta\mathbb{L}_{t22} \end{bmatrix} = \frac{1}{\mu}\left(\delta\mathbb{L}_o + z\delta\mathbb{L}_{s\beta}\right)\,\mathbb{G}_{(2\times2)} \tag{3.18}$$

with

$$\mathbb{G} = \mathbb{I} + z\,\mathbb{C}_b; \qquad \mathbb{C}_b = \mathbb{C}_o^{-1}\,\overline{\mathbb{B}}; \qquad \overline{\mathbb{B}} = \hat{\mathbb{B}}_z\,\mathbb{C}_o; \qquad \mathbb{C}_o = \mathbb{F}_o^{-1}\,\mathbb{Q} \tag{3.19}$$

and

$$\delta\mathbb{L}_o = \left[\boldsymbol{t}_1 \vdots \boldsymbol{t}_2\right]^T \left[\delta\boldsymbol{u}_{,\xi} \vdots \delta\boldsymbol{u}_{,\eta}\right]\,\mathbb{C}_{o(2\times2)} \tag{3.20}$$

$$\delta\mathbb{L}_{s\beta} = \left[\boldsymbol{t}_1 \vdots \boldsymbol{t}_2\right]^T \left[\delta\boldsymbol{\beta}_{,\xi} \vdots \delta\boldsymbol{\beta}_{,\eta}\right]\,\mathbb{C}_{o(2\times2)} \tag{3.21}$$

By replacing eq(3.19) into eq(3.18), we can obtain a quadratic approximation of strains in z, as follows :

$$\delta\mathbb{L}_s = \frac{1}{\mu}\left(\delta\mathbb{L}_o + z\,\delta\mathbb{L}_1 + z^2\,\delta\mathbb{L}_2\right) \tag{3.22}$$

with $\delta\mathbb{L}_1 = (\delta\mathbb{L}_o + \delta\mathbb{L}_{s\beta})\,\mathbb{C}_{b(2\times2)}$, and $\delta\mathbb{L}_2 = \delta\mathbb{L}_{s\beta}\,\mathbb{C}_{b(2\times2)}$
Finally, by using eq(3.17, 3.22) and by adopting the engineering notations, the membrane/bending virtual strain vector $\delta\boldsymbol{\varepsilon}_s = \{\delta\varepsilon_x,\ \delta\varepsilon_y,\ \delta\varepsilon_{xy}\}^T$ can be derived

$$\delta\boldsymbol{\varepsilon}_s = \frac{1}{\mu}\left(\delta\boldsymbol{\varepsilon}_o + z\ \delta\boldsymbol{\varepsilon}_1 + z^2\ \delta\boldsymbol{\varepsilon}_2\right) \tag{3.23}$$

Now by introducing the finite element approximation eq(3.8), the membrane/bending virtual strain vector $\delta\boldsymbol{\varepsilon}_s$ can be rewritten as follows

$$\delta\boldsymbol{\varepsilon}_s = \frac{1}{\mu}\left(\mathbb{B}_o + z\ \mathbb{B}_1 + z^2\ \mathbb{B}_2\right)\delta\boldsymbol{u}_n \tag{3.24}$$

with

$$\begin{aligned}
\mathbb{B}_{o(3\times 20)} &= \left[\begin{array}{c|c|c|c} \cdots & \begin{array}{l}\boldsymbol{t}_1^T\ C_{1i}\\ \boldsymbol{t}_2^T\ C_{2i}\\ \boldsymbol{t}_1^T\ C_{2i} + \boldsymbol{t}_2^T\ C_{1i}\end{array} & \begin{array}{cc}0 & 0\\ 0 & 0\\ 0 & 0\end{array} & \cdots \end{array}\right];\\
\mathbb{B}_{1(3\times 20)} &= \left[\begin{array}{c|c|c|c} \cdots & \begin{array}{l}\boldsymbol{t}_1^T\ D_{1i}\\ \boldsymbol{t}_2^T\ D_{2i}\\ \boldsymbol{t}_1^T\ D_{2i} + \boldsymbol{t}_2^T\ D_{1i}\end{array} & \begin{array}{l}\boldsymbol{V}_{1i}^T\ C_{1i}\\ \boldsymbol{V}_{2i}^T\ C_{2i}\\ \boldsymbol{V}_{1i}^T\ C_{2i} + \boldsymbol{V}_{2i}^T\ C_{1i}\end{array} & \cdots \end{array}\right];\\
\mathbb{B}_{2(3\times 20)} &= \left[\begin{array}{c|c|c|c} \cdots & \begin{array}{ccc}0 & 0 & 0\\ 0 & 0 & 0\\ 0 & 0 & 0\end{array} & \begin{array}{l}\boldsymbol{V}_{1i}^T\ D_{1i}\\ \boldsymbol{V}_{2i}^T\ D_{2i}\\ \boldsymbol{V}_{1i}^T\ D_{2i} + \boldsymbol{V}_{2i}^T\ D_{1i}\end{array} & \cdots \end{array}\right]; \qquad for\ \ i = 1,4
\end{aligned} \tag{3.25}$$

and

$$\begin{aligned}
C_{1i} &= N_{i,\xi}\ \mathbb{C}_o(1,1) + N_{i,\eta}\ \mathbb{C}_o(2,1)\\
C_{2i} &= N_{i,\xi}\ \mathbb{C}_o(1,2) + N_{i,\eta}\ \mathbb{C}_o(2,2)\\
D_{1i} &= N_{i,\xi}\ \overline{\mathbb{B}}(1,1) + N_{i,\eta}\ \overline{\mathbb{B}}(2,1)\\
D_{2i} &= N_{i,\xi}\ \overline{\mathbb{B}}(1,2) + N_{i,\eta}\ \overline{\mathbb{B}}(2,2)\\
\boldsymbol{V}_{1i} &= \{-\boldsymbol{t}_1^T\cdot\boldsymbol{t}_{2i},\ \boldsymbol{t}_1^T\cdot\boldsymbol{t}_{1i}\}^T\\
\boldsymbol{V}_{2i} &= \{-\boldsymbol{t}_2^T\cdot\boldsymbol{t}_{2i},\ \boldsymbol{t}_2^T\cdot\boldsymbol{t}_{1i}\}^T
\end{aligned}$$

At the end the in-plane virtual strain can be put in a unique membrane/bending matrix denoted by $\mathbb{B}_{mb(3\times 20)}$ which is quadratic in z, as follows :

$$\delta\boldsymbol{\varepsilon}_s = \frac{1}{\mu}\mathbb{B}_{mb}\ \delta\boldsymbol{u}_n; \qquad \text{with} \quad \mathbb{B}_{mb} = \mathbb{B}_o + z\ \mathbb{B}_1 + z^2\ \mathbb{B}_2 \tag{3.26}$$

We observe that the matrix $\mathbb{B}_1$ is representing the linear part on z, involves the rotation components $\delta\theta_1$, $\delta\theta_2$ but also that of displacement $\delta U_i, \delta V_i, \delta W_i$.
It is to be noticed also that in the original formulation of the MITC4 shell element, only matrices $\mathbb{B}_0$ and $\mathbb{B}_1$ have been proposed including only a linear variation in z and therefore the present shell element is enriched to the quadratic degree through the thickness, and hence one can expect enhancement of the results especially for highly dominant bending problems.

3.1.3.2 Transverse shear virtual strain

The shear virtual strains $\delta\boldsymbol{\gamma}_s$ can be derived using eq(3.11) and eq(3.16) and by adopting the engineering notation, we can obtain :

$$\delta\boldsymbol{\gamma}_s = \left\{\begin{array}{c}\delta\gamma_{xz}\\ \delta\gamma_{yz}\end{array}\right\} = \left\{\begin{array}{c}\delta\mathbb{L}_{t31} + \delta\mathbb{L}_{t13}\\ \delta\mathbb{L}_{t32} + \delta\mathbb{L}_{t23}\end{array}\right\} = \frac{1}{\mu}\mathbb{G}^T\ \delta\boldsymbol{\gamma}_o = \frac{1}{\mu}\left(\boldsymbol{\gamma}_o + z\ \boldsymbol{\gamma}_1\right) \tag{3.27}$$

and

$$\delta\boldsymbol{\gamma}_o = \mathbb{C}_o^T\ \delta\boldsymbol{\gamma}_\alpha; \qquad \delta\boldsymbol{\gamma}_1 = \overline{\mathbb{B}}^T\ \delta\boldsymbol{\gamma}_\alpha \tag{3.28}$$

with the covariant virtual shearing $\delta\boldsymbol{\gamma}_\alpha = \{\delta\gamma_\xi,\ \delta\gamma_\eta\}^T$.
$\delta\boldsymbol{\gamma}_o$ the virtual shear strains at the mid-surface for $z = 0$.
$\delta\boldsymbol{\gamma}_\alpha = \{\delta\gamma_\xi,\ \delta\gamma_\eta\}^T$ the covariant virtual shear strains, which are treated in the following. Indeed in order to avoid shear locking, the Assumed Natural Strain (ANS) method will be applied. It consists in discretizing the shear strain with a unique constant value located at each of mid-edges. Two shear values γ_ξ^{A1}, γ_ξ^{A2} along ξ and two shear values γ_η^{B1}, γ_η^{B2} along η). Then the shear strain is re-interpolated linearly, as follows:

$$\begin{cases} \gamma_\xi = \left(\dfrac{1-\eta}{2}\right)\gamma_\xi^{A1} + \left(\dfrac{1+\eta}{2}\right)\gamma_\xi^{A2} \\ \\ \gamma_\eta = \left(\dfrac{1-\xi}{2}\right)\gamma_\eta^{B1} + \left(\dfrac{1+\xi}{2}\right)\gamma_\eta^{B2} \end{cases} \tag{3.29}$$

Points $A1, A2, B1$ and $B2$ are indicated on Figure 3.4. The values γ_ξ^{A1}, ..., γ_η^{B2} are then expressed in terms of nodal virtual dof $\delta\boldsymbol{u}_n$.

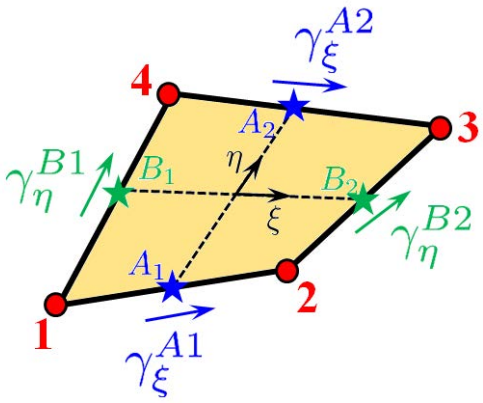

Figure 3.4: Assumed Natural Shear strain to avoid shear locking.

$$\begin{cases} \gamma_\xi^{A1} = (\boldsymbol{a}_1 \cdot \boldsymbol{\beta} + \boldsymbol{n} \cdot \boldsymbol{u}_{p,\xi})_{\xi=0,\eta=-1}\,; & \gamma_\xi^{A2} = (\boldsymbol{a}_1 \cdot \boldsymbol{\beta} + \boldsymbol{n} \cdot \boldsymbol{u}_{p,\xi})_{\xi=0,\eta=+1} \\ \gamma_\eta^{B1} = (\boldsymbol{a}_2 \cdot \boldsymbol{\beta} + \boldsymbol{n} \cdot \boldsymbol{u}_{p,\eta})_{\xi=-1,\eta=0}\,; & \gamma_\eta^{B2} = (\boldsymbol{a}_1 \cdot \boldsymbol{\beta} + \boldsymbol{n} \cdot \boldsymbol{u}_{p,\eta})_{\xi=+1,\eta=0} \end{cases} \tag{3.30}$$

By using eq(3.29) and eq(3.30), the covariant virtual shear strains $\delta\boldsymbol{\gamma}_\alpha$ reads

$$\delta\boldsymbol{\gamma}_\alpha = \mathbb{B}_{s\xi_{(2\times 20)}}\ \delta\boldsymbol{u}_n \tag{3.31}$$

with

$$\mathbb{B}_{s\xi} = \left[\begin{array}{cc|cc|cc|cc} -\boldsymbol{n}^{A1} & -\boldsymbol{d}_1^{A1} & \boldsymbol{n}^{A1} & \boldsymbol{d}_2^{A1} & \boldsymbol{n}^{A2} & \boldsymbol{d}_2^{A2} & -\boldsymbol{n}^{A2} & \boldsymbol{d}_1^{A2} \\ -\boldsymbol{n}^{B1} & -\boldsymbol{d}_1^{B1} & \boldsymbol{n}^{B2} & \boldsymbol{d}_1^{B2} & \boldsymbol{n}^{B2} & \boldsymbol{d}_2^{B2} & -\boldsymbol{n}^{B1} & \boldsymbol{d}_2^{B1} \end{array}\right] \tag{3.32}$$

$$\begin{cases} \boldsymbol{n}^{A1} = \dfrac{1-\eta}{4}\,\boldsymbol{n}_{A1}; \boldsymbol{n}^{A2} = \dfrac{1+\eta}{4}\,\boldsymbol{n}_{A2}; \boldsymbol{n}^{B1} = \dfrac{1-\xi}{4}\,\boldsymbol{n}_{B1}; \boldsymbol{n}^{B2} = \dfrac{1+\xi}{4}\,\boldsymbol{n}_{B2} \\ \boldsymbol{d}_1^{A1} = \dfrac{1-\eta}{4}\,\{-\boldsymbol{a}^{A1}\cdot\boldsymbol{t}_{21}, \boldsymbol{a}^{A1}\cdot\boldsymbol{t}_{11}\}^T; \boldsymbol{d}_1^{A2} = \dfrac{1+\eta}{4}\,\{-\boldsymbol{a}^{A2}\cdot\boldsymbol{t}_{24}, \boldsymbol{a}^{A2}\cdot\boldsymbol{t}_{14}\}^T \\ \boldsymbol{d}_1^{B1} = \dfrac{1-\xi}{4}\,\{-\boldsymbol{a}^{B1}\cdot\boldsymbol{t}_{21}, \boldsymbol{a}^{B1}\cdot\boldsymbol{t}_{11}\}^T; \boldsymbol{d}_1^{B2} = \dfrac{1+\xi}{4}\,\{-\boldsymbol{a}^{B2}\cdot\boldsymbol{t}_{22}, \boldsymbol{a}^{B2}\cdot\boldsymbol{t}_{12}\}^T \\ \boldsymbol{d}_2^{A1} = \dfrac{1-\eta}{4}\,\{-\boldsymbol{a}^{A1}\cdot\boldsymbol{t}_{22}, \boldsymbol{a}^{A1}\cdot\boldsymbol{t}_{12}\}^T; \boldsymbol{d}_2^{A2} = \dfrac{1+\eta}{4}\,\{-\boldsymbol{a}^{A2}\cdot\boldsymbol{t}_{23}, \boldsymbol{a}^{A2}\cdot\boldsymbol{t}_{13}\}^T \\ \boldsymbol{d}_2^{B1} = \dfrac{1-\xi}{4}\,\{-\boldsymbol{a}^{B1}\cdot\boldsymbol{t}_{24}, \boldsymbol{a}^{B1}\cdot\boldsymbol{t}_{14}\}^T; \boldsymbol{d}_2^{B2} = \dfrac{1+\xi}{4}\,\{-\boldsymbol{a}^{B2}\cdot\boldsymbol{t}_{23}, \boldsymbol{a}^{B2}\cdot\boldsymbol{t}_{13}\}^T \\ \boldsymbol{a}^{A1} = \dfrac{\boldsymbol{X}_2-\boldsymbol{X}_1}{2}; \boldsymbol{a}^{A2} = \dfrac{\boldsymbol{X}_3-\boldsymbol{X}_4}{2}; \boldsymbol{a}^{B1} = \dfrac{\boldsymbol{X}_4-\boldsymbol{X}_1}{2}; \boldsymbol{a}^{B2} = \dfrac{\boldsymbol{X}_3-\boldsymbol{X}_2}{2} \end{cases}$$

At the end the shear virtual strain can be put in a matrix denoted by $\mathbb{B}_{s(2\times 20)}$ which is linear in z, it is given by :

$$\delta\boldsymbol{\gamma}_s = \frac{1}{\mu}\mathbb{B}_s\,\delta\boldsymbol{u}_n; \qquad \text{with} \quad \mathbb{B}_s = \mathbb{B}_{so} + z\,\mathbb{B}_{s1} \tag{3.33}$$

with $\mathbb{B}_{so} = \mathbb{C}_o^T\,\mathbb{B}_{s\xi}$ and $\mathbb{B}_{s1} = \overline{\mathbb{B}}^T\,\mathbb{B}_{s\xi}$.

3.1.4 Principal of virtual work

In the present investigation, the Updated Lagrangian Formulation (ULF) is used to define the internal force vector $\boldsymbol{f}_{int}^e$ and the mass matrix $\mathbb{M}^e$ of the quadrilateral shell element. Therefore the equilibrium will be expressed on the deformed configuration. The principal of virtual work at the element level W^e can be stated at any time t as the balance between the internal virtual work W_{int}^e, the external virtual work W_{ext}^e and the inertial virtual work W_m^e. It can be written as :

$$W^e = W_{int}^e - W_{ext}^e + W_m^e \tag{3.34}$$

with

$$W_{int}^e = \int_{V^e} \delta\boldsymbol{\varepsilon}^T\boldsymbol{\sigma}\,dV \tag{3.35}$$

$$W_{ext}^e = \int_{S^e} \delta\boldsymbol{u}^T\boldsymbol{f}_s\,dS + \int_{V^e} \delta\boldsymbol{u}^T\boldsymbol{f_b}\,dV \tag{3.36}$$

$$W_m^e = \int_{V^e} \delta\boldsymbol{u}^T\rho\ddot{\boldsymbol{u}}\,dV \tag{3.37}$$

where S^e and V^e are the element surface and volume respectively.

3.1.4.1 Internal force vector

The internal force vector can be derived from the expression of the internal virtual work eq(3.35), which can be rewritten as follows

$$W_{int}^e = \int_{V^e} \left(\delta\boldsymbol{\varepsilon}_s^T\boldsymbol{\sigma}_s + \delta\boldsymbol{\gamma}_s^T\boldsymbol{\tau}\right)dV \tag{3.38}$$

with $\boldsymbol{\sigma}_s = \{\sigma_x, \sigma_y, \sigma_{xy}\}^T$ the in-plane stresses and $\boldsymbol{\tau} = \{\sigma_{xz}, \sigma_{yz}\}^T$ the shearing stresses.
By using eq(3.26) and eq(3.33) we can have

$$\begin{aligned} W^e_{int} = \quad & \delta \boldsymbol{u}_n^T \int_{V^e} \frac{1}{\mu} \left(\mathbb{B}_o^T + z\, \mathbb{B}_1^T + z^2\, \mathbb{B}_2^T \right) \boldsymbol{\sigma}_s \, dV + \\ & \delta \boldsymbol{u}_n^T \int_{V^e} \frac{1}{\mu} \left(\mathbb{B}_{so}^T + z\, \mathbb{B}_{s1}^T \right) \boldsymbol{\tau} \, dV = \delta \boldsymbol{u}_n^T \, \boldsymbol{f}^e_{int} \end{aligned} \tag{3.39}$$

By using $dV = \mu dz dA$, the element internal force vector takes the following form

$$\boldsymbol{f}^e_{int} = \int_{A^e} \int_{z=-h/2}^{z=+h/2} \left[\left(\mathbb{B}_o^T + z\, \mathbb{B}_1^T + z^2\, \mathbb{B}_2^T \right) \boldsymbol{\sigma}_s + \left(\mathbb{B}_{so}^T + z\, \mathbb{B}_{s1}^T \right) \boldsymbol{\tau} \right] dz\, dA \tag{3.40}$$

The final expression of the internal force vector expressed in the reference element reads

$$\begin{aligned} \boldsymbol{f}^e_{int} = \quad & \int_{\xi=-1}^{\xi=+1} \int_{\eta=-1}^{\eta=+1} \int_{\zeta=-1}^{\zeta=+1} \left(\mathbb{B}_o^T + \frac{h}{2}\zeta\, \mathbb{B}_1^T + \frac{h^2}{4}\zeta^2\, \mathbb{B}_2^T \right) \boldsymbol{\sigma}_s \, J_o \, \frac{h}{2} \, d\zeta \, d\eta \, d\xi + \\ & \int_{\xi=-1}^{\xi=+1} \int_{\eta=-1}^{\eta=+1} \int_{\zeta=-1}^{\zeta=+1} \left(\mathbb{B}_{so}^T + \frac{h}{2}\zeta\, \mathbb{B}_{s1}^T \right) \boldsymbol{\tau} \, J_o \, \frac{h}{2} \, d\zeta \, d\eta \, d\xi \end{aligned} \tag{3.41}$$

The integration of the internal force vector given in eq(3.41) is done following two quadrature rules. The integration in the mid-surface (ξ, η) of the element is done using 2×2 Gauss quadrature points. While the integration through the thickness direction (ζ) is done using 5 or more Lobatto quadrature points (depending on the degree of plastic strains and the desired accuracy).

3.1.4.2 Mass matrix

The mass matrix of the element can be calculated using the expression of the inertial virtual work eq(3.37), where the finite element approximation of virtual displacement is applied eq(2.3), as follows

$$\boldsymbol{u} = \boldsymbol{N}\, \boldsymbol{u_n}; \qquad \delta \boldsymbol{u} = \boldsymbol{N}\, \delta \boldsymbol{u}_n; \qquad \ddot{\boldsymbol{u}} = \boldsymbol{N}\, \ddot{\boldsymbol{u}}_{\boldsymbol{n}} \tag{3.42}$$

with $\boldsymbol{u}_n$ and $\delta \boldsymbol{u}_n$ the real and virtual element nodal degrees of freedom respectively and $\boldsymbol{N}$ is the finite element approximation matrix. The inertial virtual work W^e_m can be written as :

$$W^e_m = \delta \boldsymbol{u}_n^T \left(\int_{V^e} \delta \boldsymbol{N}^T \rho \boldsymbol{N} \, dV \right) \ddot{\boldsymbol{u}}_{\boldsymbol{n}} = \delta \boldsymbol{u}_n^T \, \mathbb{M}^e \, \ddot{\boldsymbol{u}}_{\boldsymbol{n}} \tag{3.43}$$

Therefore, the consistent mass matrix of the shell element is

$$\mathbb{M}^e = \int_{V^e} \boldsymbol{N}^T \, \rho \, \boldsymbol{N} \, dV = \int_{\xi=-1}^{\xi=+1} \int_{\eta=-1}^{\eta=+1} \int_{\zeta=-1}^{\zeta=+1} \boldsymbol{N}^T \, \rho \, \boldsymbol{N} \, \mu J_o \, \frac{h}{2} \, d\zeta \, d\eta \, d\xi \tag{3.44}$$

In the practice, this last expression cannot be used effectively in explicit calculations where matrix inversions are not feasible. The lumped mass matrix can be computed using the translational masses from the consistent mass matrix by row summing, leading to the following mass at element node i:

$$M^{trans}_{ii} = \int_{V^e} \rho \, N_i^2 \, dV = \int_{\xi=-1}^{\xi=+1} \int_{\eta=-1}^{\eta=+1} \int_{\zeta=-1}^{\zeta=+1} \rho \, N_i^2 \, \mu J_o \, \frac{h}{2} \, d\zeta \, d\eta \, d\xi \tag{3.45}$$

The rotational masses are computed by scaling the translational mass at the node by the factor α :

$$M^{rota}_{ii} = \alpha \, M^{trans}_{ii} \tag{3.46}$$

3.1.5 Transformation from five to six dof

Rotational dof of the shell element θ_{1i} and θ_{2i} are rotations around tangent vectors $\boldsymbol{t}_{1i}$ and $\boldsymbol{t}_{2i}$ defined at each node i. These rotations have to be transformed to the global framework, using the following relation:

$$\boldsymbol{\theta} = \boldsymbol{t}_1\ \theta_1 + \boldsymbol{t}_2\ \theta_2 + \boldsymbol{n}\ \theta_3 = \boldsymbol{i}\ \theta_X + \boldsymbol{j}\ \theta_Y + \boldsymbol{k}\ \theta_Z \tag{3.47}$$

$$\mathbb{Q} \left\{ \begin{array}{c} \theta_1 \\ \theta_2 \\ \theta_3 \end{array} \right\} = \left\{ \begin{array}{c} \theta_X \\ \theta_Y \\ \theta_Z \end{array} \right\} \qquad \Rightarrow \qquad \left\{ \begin{array}{c} \theta_1 \\ \theta_2 \\ \theta_3 \end{array} \right\} = \mathbb{Q}^T \left\{ \begin{array}{c} \theta_X \\ \theta_Y \\ \theta_Z \end{array} \right\} \tag{3.48}$$

The extension from five to six dof can be done by using the following steps:
a) Calculate an artificial $\boldsymbol{f}^z_{int(4,1)}$

$$W^z_{int} = \varepsilon \int_{A^e} \{\delta\theta_{z,x},\ \delta\theta_{z,y}\}^T\ \{\theta_{z,x},\ \theta_{z,x}\}\ J_o\ d\xi d\eta = \delta\boldsymbol{\theta}^T_{zn}\ \boldsymbol{f}^z_{int} \tag{3.49}$$

with the FE approximation $\theta_z \equiv \theta_3 = \sum_{i=1,4} N_i \theta_{zi} = \boldsymbol{N}^T\ \boldsymbol{\theta}_{zn}$

b) Extend the internal force vector $\boldsymbol{f}_{int}(20 \times 1) = \{\boldsymbol{f}^1_{int}, \boldsymbol{f}^2_{int}, \boldsymbol{f}^3_{int}, \boldsymbol{f}^4_{int}\}^T$ to $\overline{\boldsymbol{f}}_{int}(24 \times 1)$

$$\overline{\boldsymbol{f}}^i_{int(6\times1)} = \{\boldsymbol{f}^i_{int(5\times1)},\ \boldsymbol{f}^{zi}_{int}\} \qquad i = 1, 4 \tag{3.50}$$

with the new nodal dof in the global framework $\boldsymbol{u}_n = \{\ldots, U_i, V_i, W_i, \theta_{Xi}, \theta_{Yi}, \theta_{Zi}, \ldots\}^T$, for $i = 1, 4$.

c) Transform the internal force vector to the global framework as follows

$$\boldsymbol{F}_{int(24\times1)} = \mathbb{T}^T\ \overline{\boldsymbol{f}}_{int(24\times1)} \tag{3.51}$$

using the transformation matrix

$$\mathbb{T}_{(24\times24)} = \begin{bmatrix} \mathbb{I} & & & & \\ & \mathbb{Q}^T_1 & & & \\ & & \ddots & & \\ & & & \mathbb{I} & \\ & & & & \mathbb{Q}^T_4 \end{bmatrix}; \quad \mathbb{I} = \begin{bmatrix} 1 & 0 & 0 \\ 0 & 1 & 0 \\ 0 & 0 & 1 \end{bmatrix}; \quad \mathbb{Q}_i = \left[\boldsymbol{t}_{1i} \vdots \boldsymbol{t}_{2i} \vdots \boldsymbol{n}_i\right]$$

3.1.6 Numerical Validation

In the following, the efficiency of the developed quadrilateral shell element will be demonstrated through the resolution of three numerical applications. Commercial finite element solver ABAQUS is used to demonstrate the solution accuracy of the developed shell element. Finite element solver ABAQUS is selected because these three numerical applications are given in the ABAQUS benchmarks manual and their analytical solutions are also given. Fully integrated shell element S4 of ABAQUS is selected because it is equivalent to Ls-dyna fully integrated shell element ELFORM16. Obtained results from the developed element are compared with the reference analytical and ABAQUS S4 shell element results.

3.1.6.1 Deflection of a clamped plate

A square clamped plate structure of length $L = 20cm$ and thickness $h = 0.02cm$ is subjected to a unit central point load $P = 1kN$ as depicted in Figure 3.5. The material data correspond to $E = 10^6 kN/cm^2$, $\nu = 0.3$. The reference analytical solution of deflection is $W_{exact} = 0.0056\dfrac{PL^2}{D}$ and corresponds to $W_{exact} = 3.0576cm$

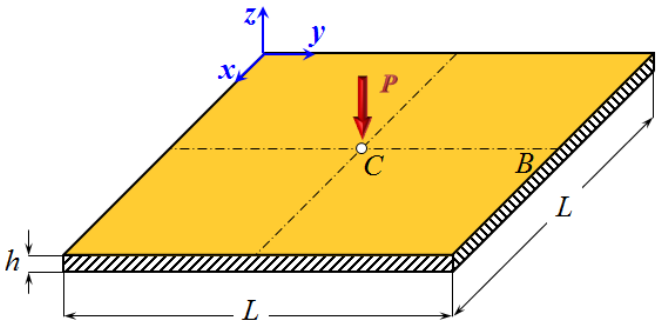

Figure 3.5: Square clamped plate with central point load.

Only a quarter of the plate is modeled due to symmetric boundary conditions and different FE meshes ha ıvergence.

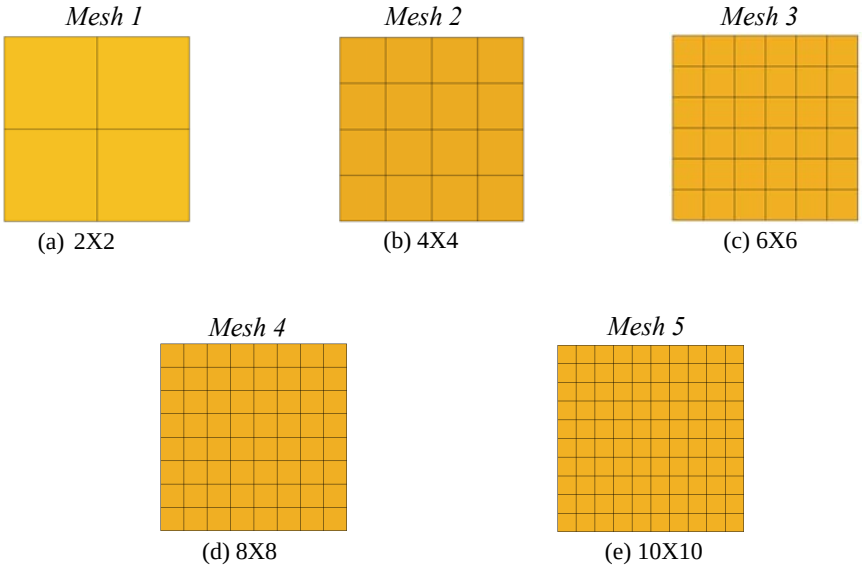

Figure 3.6: Five different meshes of the plate.

Deflection contour plots of Mesh 1 and Mesh 5 are presented in Figure 3.7. In Mesh 1, ABAQUS S4 element and developed shell element show the same deflection values with an error of 13.47%. For the refined Mesh 5, our developed shell element shows better solution with 0.42% error compared to ABAQUS with 0.46%.
The central normalized deflection W/W_{exact} is plotted function of number of elements per edge as depicted in Figure 3.8. Similar results have been obtained compared to the S4 of ABAQUS.

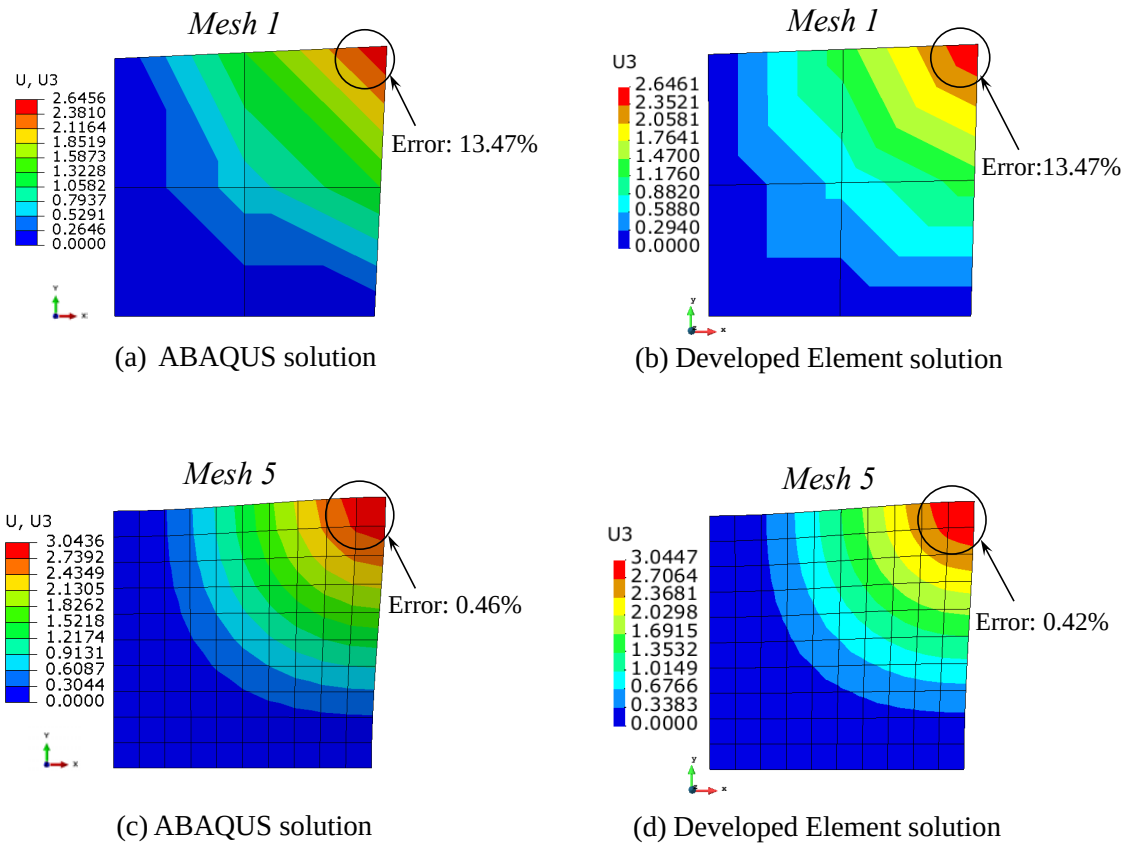

Figure 3.7: Deflection contour plots of the plate.

For quantitative comparison, the central deflection with normalized values are given in Table

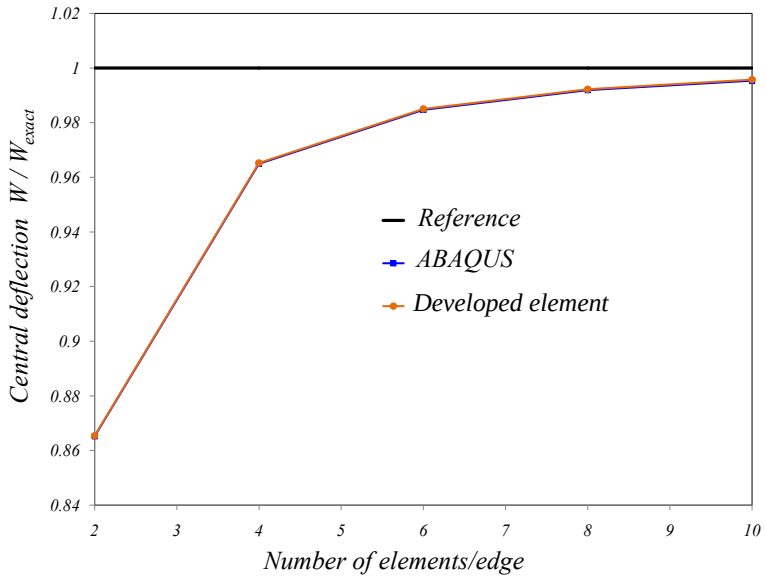

Figure 3.8: Central deflection comparison (Our developed element vs. ABAQUS S4).

3.1, where our solution is compared to the reference solution and to the ABAQUS S4 element.

One can observe from Table 3.1, that very good agreement have been obtained between the

Table 3.1: Central deflection comparison (our element vs. ABAQUS S4)

Number of elements/edge	Reference	ABAQUS	Developed Element
2	1.0000	0.8652	0.8654
4	1.0000	0.9650	0.9653
6	1.0000	0.9847	0.9850
8	1.0000	0.9919	0.9923
10	1.0000	0.9954	0.9958

developed shell element and the solution of ABAQUS S4 shell element using the same 2×2 integration quadrature in the plane of the element. This result can confirm the good and free-error implementation of our shell element in Ls-dyna commercial software.

3.1.6.2 Pinched cylindrical shell

The dimensions of the pinched cylindrical shell including a rigid diaphragm support are shown in Figure 3.9 with a length $L = 6m$, a radius $R = 3m$ and a thickness $h = 0.03m$. The material properties correspond to $E = 3 \times 10^6 kN/m^2$, $\nu = 0.3$ and two concentrated loads $P = 1kN$. Only the 1/8 of the cylinder is modeled due to symmetry. Symmetrical boundary conditions are applied on the AB, BC and DC edges whereas clamped at edge AD. The reference analytical deflection at point C is $U_{ref} = -\dfrac{Ehw_C}{P} = 164.24$.

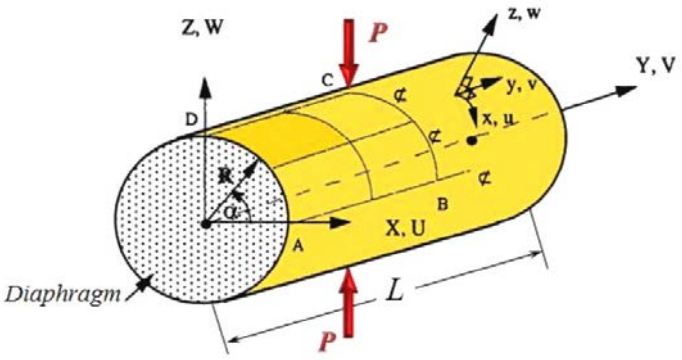

Figure 3.9: Geometry of the pinched cylindrical shell.

Eight different meshes are generated as depicted in the Figure 3.10 in order to study the convergence of results. As in the previous example, to study the accuracy of developed shell element, results are compared with S4 shell element of ABAQUS which uses the same 2×2 integration quadrature in the plane.
Deflection contour plots of Mesh 1 and Mesh 8 are presented in Figure 3.11. In Mesh 8, our element shows better solution accuracy with an error of 0.95% much less than the one of ABAQUS 6.73%.
Figure 3.12 shows the graphical comparison between our shell element and ABAQUS where the deflection U/U_{ref} at point C is plotted as a function of number of elements per edge. Our shell element shows better results and provides faster convergence compared to ABAQUS. The deflection values at point C are given in Table 3.2, which shows that convergence of our developed shell element is faster than the ABAQUS S4 shell element which uses the same 2×2 integration quadrature in the plane of the element. This result can confirm the importance of the quadratic enrichment introduced in our formulation.

Table 3.2: Central deflection comparison (our element vs. ABAQUS S4)

Number of elements/edge	Reference	ABAQUS	Developed element
2	1.0000	0.0425	0.0470
4	1.0000	0.3883	0.3835
6	1.0000	0.6217	0.6292
8	1.0000	0.7544	0.7755
10	1.0000	0.8321	0.8651
12	1.0000	0.8801	0.9229
14	1.0000	0.9114	0.9622
16	1.0000	0.9328	0.9905

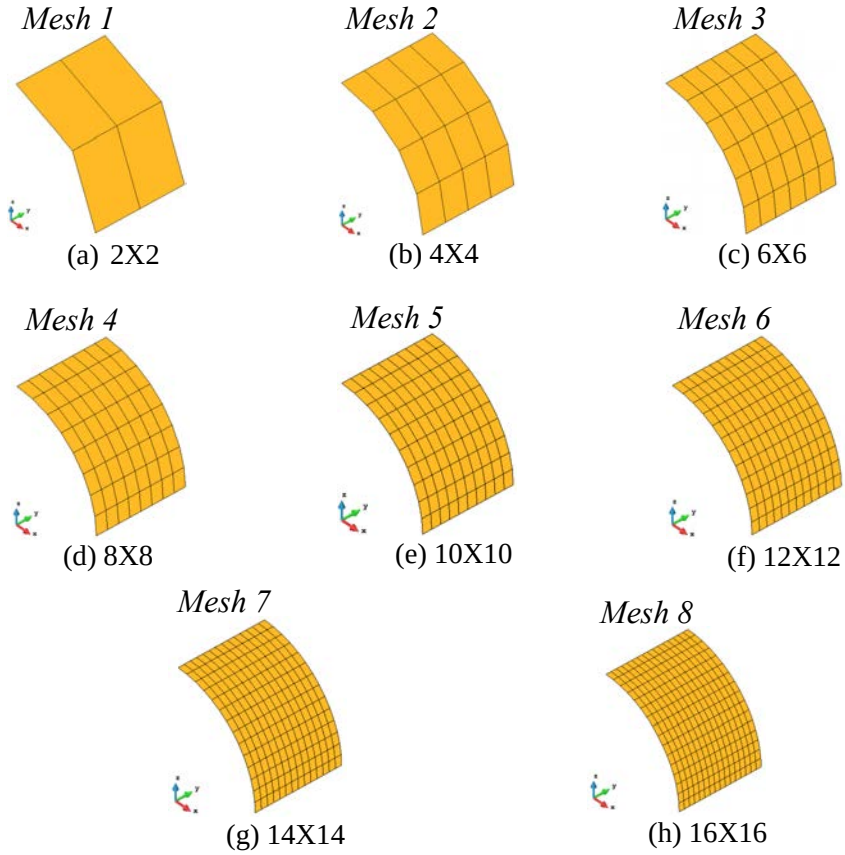

Figure 3.10: Eight different meshes of the pinched cylindrical shell.

3.1.6.3 Pinched hemispherical shell

The hemispherical shell structure of Figure 3.13 is pinched by two concentrated forces $P = 2kN$. The hemispherical radius is $R = 10m$ and its thickness $h = 0.04m$.
The material properties are $E = 6.825 \times 10^7 kN/m^2$, $\nu = 0.3$. Only a 1/8 of the hemispherical shell is modeled due to the symmetry. At point B, $W = 0$ whereas symmetrical boundary conditions are applied on edges AC and BD. The reference solution of deflection at point A is $U_A = -V_B = 0.094m$.
Seven different mesh schemes are generated as depicted in Figure 3.14 to study the convergence. Deflection at point A obtained using our element is compared with ABAQUS solution. Figure 3.15 shows the deflection contour maps of Mesh 1 and Mash 7. In Mesh 1, we can observe that our element shows more accurate solution with an error of 10.32% smaller than the one of ABAQUS with25.74%. In refined Mesh 7, solution error is 0.53% better than the ABAQUS solution of 1.17% error.
Graphical comparison of deflection at point A is given in Figure 3.16. Deflection results show a faster convergence of our element compared to S4 of ABAQUS, which again show the importance of the quadratic enrichment introduced in our formulation. Table 3.3 shows deflection values at point A in different mesh schemes obtained by developed shell and S4 elements of ABAQUS.

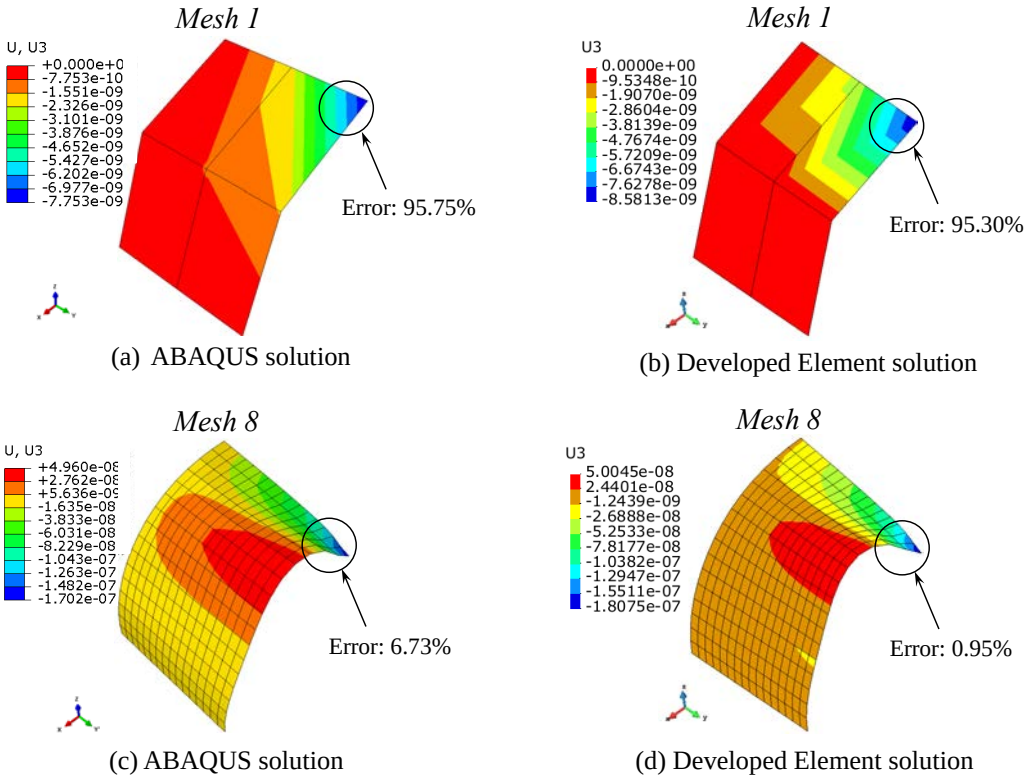

Figure 3.11: Deflection contour plots of pinched cylindrical shell.

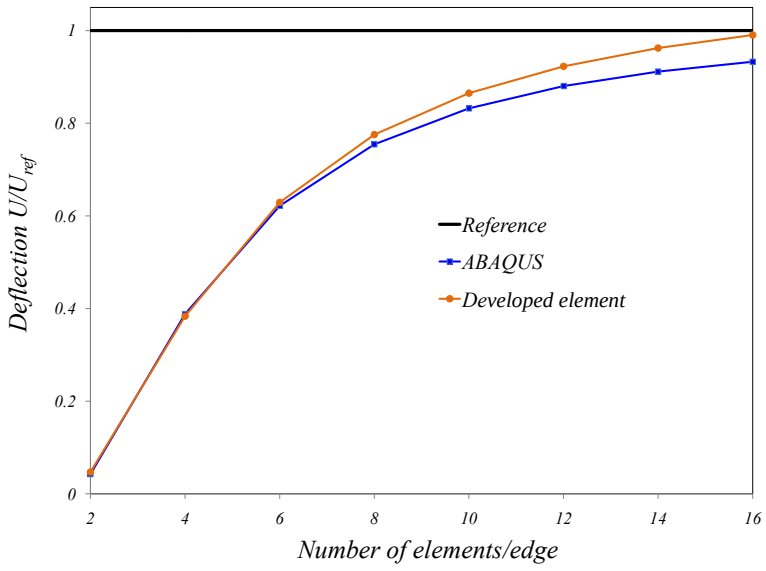

Figure 3.12: Deflection comparison (Our developed element vs. ABAQUS S4)

3.2 Enrichment using the interpolation covers method

The FE method is an effective technique where the key success is probably due to the fact that meshes can be used to span over complex parts geometries. However, the solution accuracy is highly depending on the mesh quality, therefore special mesh refinement is usually required, to

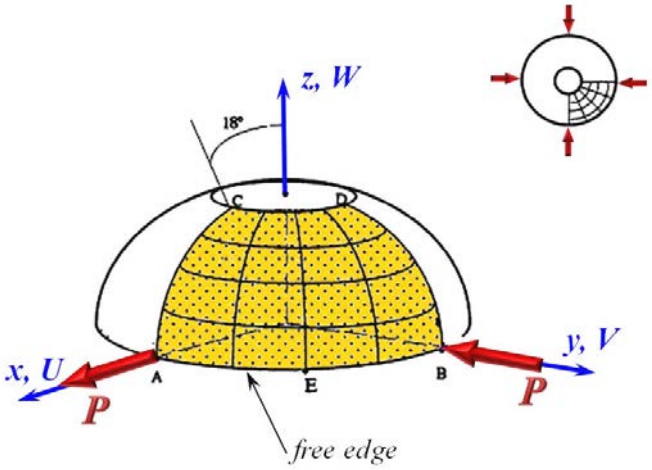

Figure 3.13: Geometry of the pinched hemispherical shell.

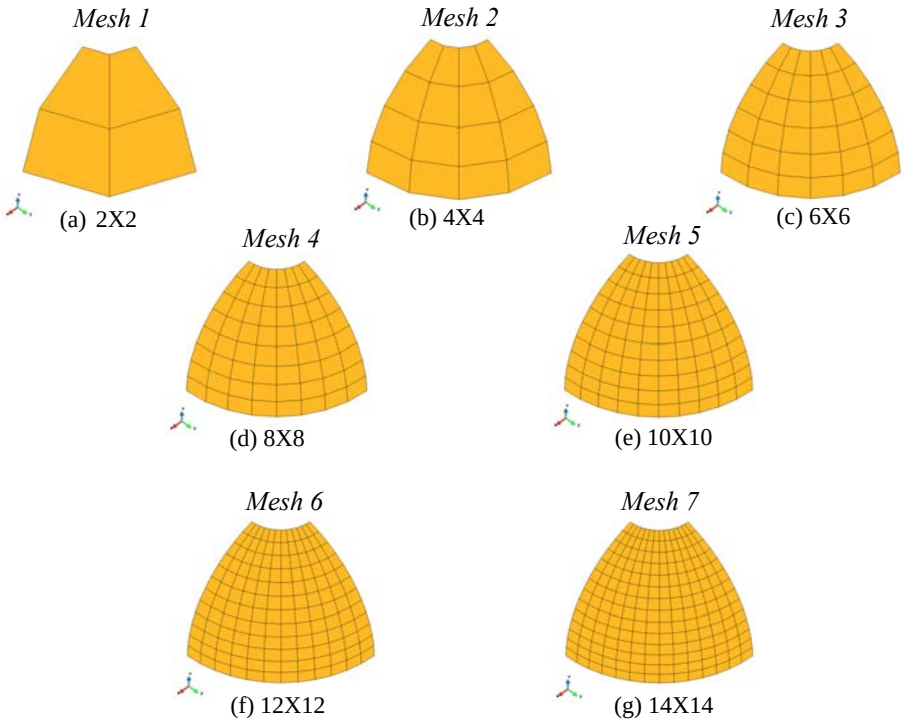

Figure 3.14: Different meshes of the pinched hemispherical shell

insure reliable solution with desired accuracy.
Among the numerous methods used for solution improvement using mesh refinement, Kim and Bathe [44, 46] proposed recently a FE enriching technique called the "*Interpolation Covers Method*" (ICM). In the ICM the solution accuracy of the standard low-order FE discretization is improved without any increase of the number of elements. Therefore, the major advantage of the ICM is that the higher order enrichment can be achieved without introducing additional dof, by the use of surrounding nodes belonging to the target shell element e as shown in Figure 3.17.
Let $\boldsymbol{Q}^n = \{\boldsymbol{x}_i\}_{i=1}^n$ be a set of position vectors of n given neighboring nodes expressed in the local framework $(\boldsymbol{t}_1, \boldsymbol{t}_2, \boldsymbol{n})$ of the target element e, given by:

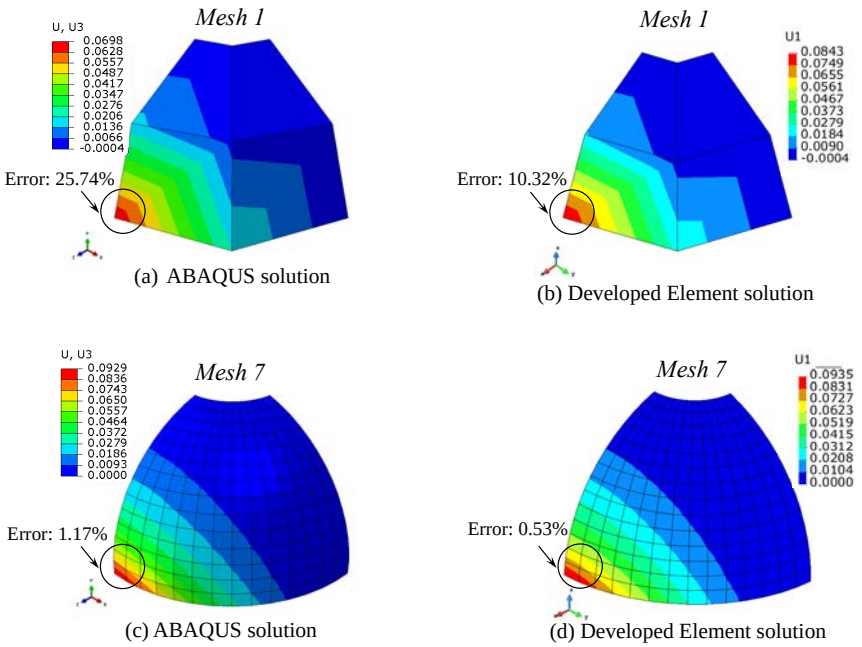

Figure 3.15: Deflection contour plots of the pinched hemispherical shell

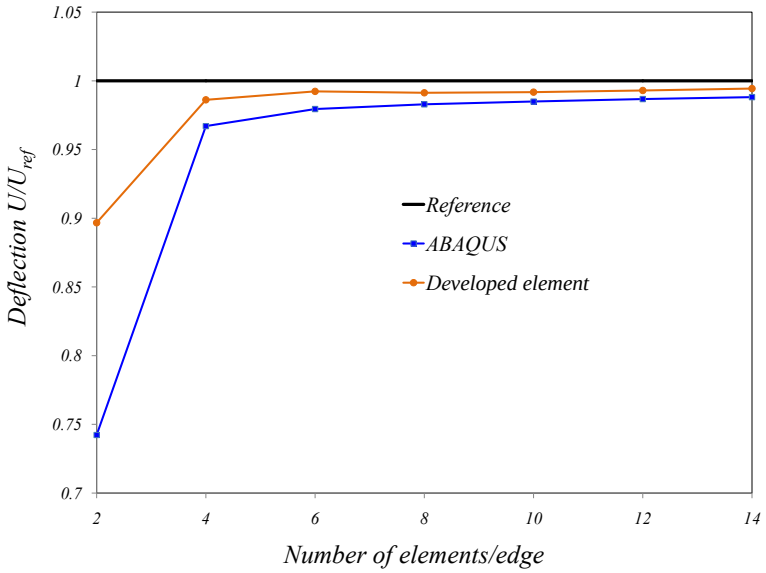

Figure 3.16: Deflection comparison (Our shell element vs. ABAQUS S4)

$$\boldsymbol{x}_i = \mathbb{Q}^T \, \boldsymbol{X}_i \tag{3.52}$$

with $\boldsymbol{X}_i$ the position vector of node i surrounding the target element e, and $\mathbb{Q} = \left[\boldsymbol{t}_1 \vdots \boldsymbol{t}_2 \vdots \boldsymbol{n}\right]$ the orthonormal basis of the target element e, defined previously. To enrich the standard FE interpolation for the solution variable $\boldsymbol{x}$, we use interpolation cover functions

$$\mathcal{P}_i^p \left[u\right] = u_i + \{\xi,\ \eta,\ \xi^2,\ \xi\eta,\ \eta^2,\ \cdots,\ \eta^p\}^T \hat{\boldsymbol{u}}_i \tag{3.53}$$

Table 3.3: Central deflection comparison (our element vs. ABAQUS S4)

Number of elements/edge	Reference	ABAQUS	Developed element
2	1.0000	0.7424	0.8967
4	1.0000	0.9671	0.9862
6	1.0000	0.9794	0.9923
8	1.0000	0.9829	0.9913
10	1.0000	0.9850	0.9918
12	1.0000	0.9867	0.9930
14	1.0000	0.9881	0.9944

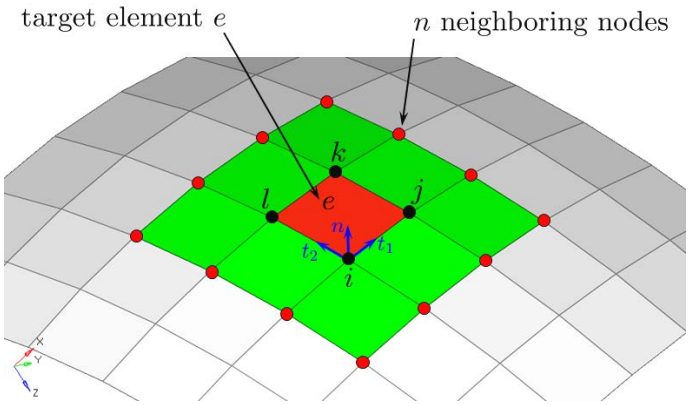

Figure 3.17: Description of sub-domains for enriched cover interpolations.

where u_i is the standard quadrilateral nodal dof, $\hat{\boldsymbol{u}}_i = \{\hat{u}_i^{\xi},\ \hat{u}_i^{\eta},\ \hat{u}_i^{\xi^2},\ \hat{u}_i^{\xi_i\eta_i},\ \hat{u}_i^{\eta_i^2},\ \cdots,\ \hat{u}_i^{\eta_i^p}\}^T$ lists of additional degrees of freedom per cover region and p is the order of the complete polynomial used.

The enriched cover approximation of the field variable u is represented by :

$$u = \sum_{e=1}^{nelt} \sum_{i \in i_c(e)} N_i\ \mathcal{P}_i^p\,[u] = \sum_{e=1}^{nelt} \left(\sum_{i \in i_c(e)} N_i\ u_i + \sum_{i \in i_c(e)} \widetilde{\boldsymbol{N}}_i\ \hat{\boldsymbol{u}}_i \right) \tag{3.54}$$

with $i_c(e)$ the set of cover indices and $\widetilde{\boldsymbol{N}}_i$ the enriched high degree shape function

$$\widetilde{\boldsymbol{N}}_i = N_i\ \{\xi,\ \eta,\ \xi^2,\ \xi\eta,\ \eta^2,\ \cdots,\ \eta^p\}^T \tag{3.55}$$

Considering eq(3.55), the enriched cover approximation consists of the standard FE interpolation plus additional higher order terms. To obtain a well-conditioned stiffness matrix, we use the local parametric coordinate systems (ξ, η) of the target element, instead of the cartesian coordinates (x, y).

If $\mathcal{P}_i^p\,[u] = u_i$, then the scheme reduces to the standard linear interpolation. Indeed we can regard the enriched interpolation as the standard finite element interpolation plus additional higher order terms.

An arbitrary degree of polynomial bases can be adopted in the cover interpolations. However, since high order covers yield more unknowns, we use up to quadratic covers in this work, i.e. we shall use $p \leq 2$.

3.2.1 ICM applied to the quadrilateral element

As reported previously, the standard FE approximation of solution of the 4-node shell element is

$$\delta \boldsymbol{u}_q = \delta \boldsymbol{u} + z\ \delta \boldsymbol{\beta} = \sum_{i=1,4} N_i\ \delta \boldsymbol{u}_i + z \sum_{i=1,4} N_i\ \left(-\boldsymbol{t}_{2i}\ \delta\theta_{1i} + \boldsymbol{t}_{1i}\ \delta\theta_{2i}\right) \tag{3.56}$$

where $N_i(\xi,\eta)$ are the planar shape functions of the Q4 shell element,

$$N_i(\xi,\eta) = \frac{1}{4}\left(1+\xi_i\,\xi\right)\left(1+\eta_i\,\eta\right); \qquad i = 1,4 \tag{3.57}$$

where $\delta\boldsymbol{u} = \{\delta U, \delta V, \delta W\}^T$ is the virtual translational vector and $\delta\boldsymbol{\beta} = \{\delta\theta_1, \delta\theta_2\}^T$ the virtual rotational vector, which can be written in cartesian components
Following eq(3.54), the virtual components of displacements $\delta U, \delta V, \delta W$ and rotations $\delta\theta_1, \delta\theta_2$ can be enriched using the ICM over the set of covers of target element e, as follows :

$$\delta U^{(e)} = \sum_{i\in i_c(e)} \left(N_i\ \delta U_i + \widetilde{\boldsymbol{N}}_i\ \delta\hat{\boldsymbol{U}}_i\right); \qquad \text{same for: } \delta V^{(e)}, \delta W^{(e)}, \delta\theta_1^{(e)}, \delta\theta_2^{(e)} \tag{3.58}$$

where δU_i are the usual four nodal values at the for nodes of the quadrilateral shell element, and the $\delta\hat{\boldsymbol{U}}_i$ is the list of additional unknown dof which are belonging to the n neighboring nodes.
For linear covers, we need to put $p = 1$ in eq(3.55), this will enrich the shell element from standard bilinear approximation of eq(3.57) to a quadratic approximation, then we have:

$$\widetilde{\boldsymbol{N}}_i = N_i\ \{\xi,\ \eta\}^T \tag{3.59}$$

and for quadratic covers, we have also from from eq(3.55) by using $p = 2$:

$$\widetilde{\boldsymbol{N}}_i = N_i\ \{\xi,\ \eta,\ \xi^2,\ \xi\eta,\ \eta^2\}^T \tag{3.60}$$

The finite element approximation of virtual displacements for the full Q4 shell element leads to the matrix form, using nodal degrees of freedom at four nodes and some of the surrounding nodes.

$$\delta\boldsymbol{u}_q = \mathbb{N}\ \delta\boldsymbol{u}_n + \tilde{\mathbb{N}}\ \delta\hat{\boldsymbol{u}}_n \tag{3.61}$$

with

$$\begin{aligned}
&\delta\boldsymbol{u}_n = \{..., \delta U_i, \delta V_i, \delta W_i, \delta\theta_{1i}, \delta\theta_{2i}, ...\}^T;\\
&\mathbb{N}_{3\times 20} = \left[\begin{array}{c|ccc|c|c} \dots & N_i & 0 & 0 & zN_i\boldsymbol{V}_X{}^T & \dots \\ & 0 & N_i & 0 & zN_i\boldsymbol{V}_Y{}^T & \\ & 0 & 0 & N_i & zN_i\boldsymbol{V}_Z{}^T & \end{array}\right]; \quad i = 1,4\\
&\boldsymbol{V}_X = \{-t_{2Xi},\ t_{1Xi}\}^T; \qquad \boldsymbol{V}_Y = \{-t_{2Yi},\ t_{1Yi}\}^T; \qquad \boldsymbol{V}_Z = \{-t_{2Zi},\ t_{1Zi}\}^T
\end{aligned} \tag{3.62}$$

If we use linear covers of eq(3.59), then we need two extra surrounding nodes numbered here 5 and 6, therefore the enrichment matrices are as follows

$$\begin{aligned}
&\delta\hat{\boldsymbol{u}}_n = \{..., \delta U_j, \delta V_j, \delta W_j, \delta\theta_{1j}, \delta\theta_{2j}, ...\}^T;\\
&\tilde{\mathbb{N}}_{3\times 10} = \left[\begin{array}{c|ccc|c|c} \dots & \tilde{N}_j & 0 & 0 & z\tilde{N}_j\boldsymbol{V}_X{}^T & \dots \\ & 0 & \tilde{N}_j & 0 & z\tilde{N}_j\boldsymbol{V}_Y{}^T & \\ & 0 & 0 & \tilde{N}_j & z\tilde{N}_j\boldsymbol{V}_Z{}^T & \end{array}\right]; \quad j, 5, 6\\
&\boldsymbol{V}_X = \{-t_{2Xj},\ t_{1Xj}\}^T; \qquad \boldsymbol{V}_Y = \{-t_{2Yj},\ t_{1Yj}\}^T; \qquad \boldsymbol{V}_Z = \{-t_{2Zj},\ t_{1Zj}\}^T
\end{aligned} \tag{3.63}$$

Using properly arranged unknowns in vectors, the enriched virtual displacement vector takes the following expression

$$\delta \boldsymbol{u}_q = \left[\mathbb{N} \vdots \tilde{\mathbb{N}}\right]_{(3\times 30)} \left\{ \begin{array}{c} \delta \boldsymbol{u}_n \\ \delta \hat{\boldsymbol{u}}_n \end{array} \right\}_{(30\times 1)} = \overline{\mathbb{N}}\, \delta \overline{\boldsymbol{u}}_n \tag{3.64}$$

$\overline{\mathbb{N}}$ are the new augmented enriching shape functions, which are obtained for the enriched target element e, which uses now 30 degrees of freedom (in case of linear covers), resulting from adding 10 extra dof of two surrounding nodes.
Once $\overline{\mathbb{N}}$ are obtained, then the standard procedure of generating the FE matrices for the virtual strains remain the same as shown previously. The only difference is to replace $\mathbb{N}$ by the new augmented shape functions $\overline{\mathbb{N}}$.
The internal force vector given by eq(3.41) remains exactly the same, by substituting $\mathbb{B}$ matrices by $\overline{\mathbb{B}}$ as follows

$$\begin{aligned} \boldsymbol{f}^e_{int} = & \int_{\xi=-1}^{\xi=+1}\int_{\eta=-1}^{\eta=+1}\int_{\zeta=-1}^{\zeta=+1} \left(\overline{\mathbb{B}}_o^T + \frac{h}{2}\zeta\, \overline{\mathbb{B}}_1^T + \frac{h^2}{4}\zeta^2\, \overline{\mathbb{B}}_2^T\right) \boldsymbol{\sigma}_s\, J_o\, \frac{h}{2}\, d\zeta\, d\eta\, d\xi + \\ & \int_{\xi=-1}^{\xi=+1}\int_{\eta=-1}^{\eta=+1}\int_{\zeta=-1}^{\zeta=+1} \left(\overline{\mathbb{B}}_{so}^T + \frac{h}{2}\zeta\, \overline{\mathbb{B}}_{s1}^T\right) \boldsymbol{\tau}\, J_o\, \frac{h}{2}\, d\zeta\, d\eta\, d\xi \end{aligned} \tag{3.65}$$

Contrarily to the standard formulation, now the integration of the internal force vector given in eq(3.65) is done in the mid-surface (ξ, η) using $n_g \times n_g$ Gauss quadrature points. Where n_g is the number of integration points, its value has to be fixed by the user. For linear covers, value of $n_g = 3$ has been found to be a good value for stable results. When using higher degrees covers, then the value n_g has to be high resulting in an increase of CPU computing time.
The integration through the thickness direction (ζ) will remain done using 5 or more Lobatto quadrature points, depending on the degree of plastic strains and the desired accuracy.
It has to be noticed, that the mass matrix of the enriched element is remaining the same as the standard form given by eq(3.45). Therefore no enrichment has been done for the evaluation of the mass matrix. The same procedure is also applied to generate the lumped mass matrix.

3.2.2 Assembly procedure for the enriched shell element

In the following it will be shown the general special procedure needed for the assembly of the internal force vector of enriched elements. Indeed by introducing extra-nodes surrounding the target enriched element, the resulting internal force vector will depend on the dof of its four standard nodes but also on the surrounding nodes which have been used for the enrichment.

Let consider the target element e which has to be enriched using surrounding extra-nodes as indicated in Figure 3.18. Let suppose that the target element has nodes $1, 2, 3, 4$ and assuming that surrounding nodes $U_6, U_7, U_9, U_{10}, U_{12}, U_{13}, U_{15}, U_{16}$ are used for enrichment. In this case and following Eq(3.58, 3.59), the new enriched FE approximation reads,

$$\delta U^{(e)} = \sum_{i\in i_c(e)} \left(N_i\, \delta U_i + \widetilde{\boldsymbol{N}}_i\, \delta \hat{\boldsymbol{U}}_i\right); \qquad \text{same for: } \delta V^{(e)}, \delta W^{(e)}, \delta\theta_1^{(e)}, \delta\theta_2^{(e)} \tag{3.66}$$

where δU_i are the usual four nodal values at the for nodes of the quadrilateral shell element, and the $\delta\hat{\boldsymbol{U}}_i$ is the list of additional unknown dof which are belonging to the n neighboring nodes. Using linear covers $(\widetilde{\boldsymbol{N}}_i = N_i\ \{\xi,\ \eta\}^T)$ to enrich the shell element from standard bilinear approximation of Eq(3.57) to a quadratic approximation, then Eq(3.66) can be written explicitly for the particular example of Figure 3.18 as follows

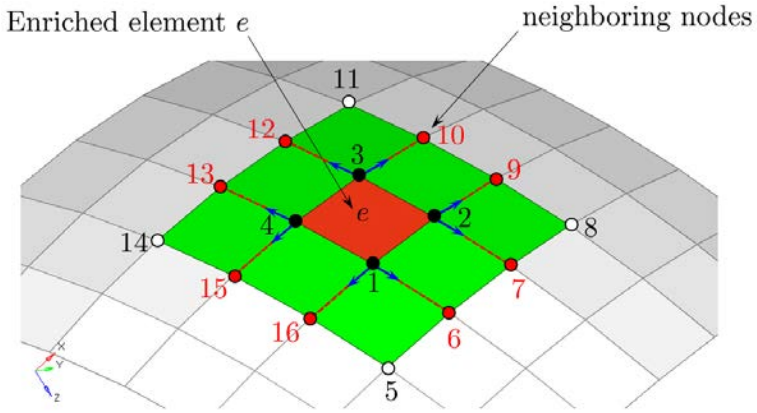

Figure 3.18: Assembly procedure for the enriched shell element.

$$\begin{aligned} \delta U^{(e)} = \; & N_1\,\delta U_1 + N_2\,\delta U_2 + N_3\,\delta U_3 + N_4\,\delta U_4 + \\ & N_1\,\xi\,\delta U_6 + N_1\,\eta\,\delta U_7 + N_2\,\xi\,\delta U_9 + N_2\,\eta\,\delta U_{10} + \\ & N_3\,\xi\,\delta U_{12} + N_3\,\eta\,\delta U_{13} + N_4\,\xi\,\delta U_{15} + N_4\,\eta\,\delta U_{16} \end{aligned} \tag{3.67}$$

In Eq(3.67), $U_1, ..., U_4$ are standard dof of the quadrilateral shell element and $U_6, U_7, U_9, U_{10}, U_{12}$, U_{13}, U_{15}, U_{16} are extra-dof of surrounding nodes as depicted in Figure 3.18.

The FE approximation used for the first displacement component $\delta U^{(e)}$ in Eq(3.67) can be repeated for the remaining four kinematic field components namely $\delta V^{(e)}, \delta W^{(e)}, \delta\theta_1^{(e)}, \delta\theta_2^{(e)}$. As a result, for the case of enriched element e given in Figure 3.18, one can have $8 \times 5 = 40$ extra-do. Knowing that the standard quadrilateral shell element has $5 \times 4 = 20$ dof, then as a result the enriched element will have a total of $40 + 20 = 60$ dof in the local framework and after transformation to global framework by adding the θ_z dof, it increases to a total $48 + 24 = 72$ dof.
Let consider now the expression of the internal virtual work of a standard quadrilateral shell element given by Eq(3.39) and using Eq(3.51), then we can write

$$W_{int}^{e} = \underbrace{\delta \boldsymbol{u}_n^T}_{1\times 24}\,\underbrace{\boldsymbol{F}_{int}^{e}}_{24\times 1} \tag{3.68}$$

Here $\boldsymbol{u}_n$ is the vector of global dof of size 24×1, given by $\boldsymbol{u}_n = \{\ldots, U_i, V_i, W_i, \theta_{Xi}, \theta_{Yi}, \theta_{Zi}, \ldots\}^T$, for $i = 1, 4$.
The internal virtual work of the enriched element of Figure 3.18 will be written as

$$W_{int}^{e} = \underbrace{\delta \boldsymbol{u}_n^T}_{1\times 24}\,\underbrace{\boldsymbol{F}_{int}^{e}}_{24\times 1} + \underbrace{\delta \hat{\boldsymbol{u}}_n^T}_{1\times 48}\,\underbrace{\hat{\boldsymbol{F}}_{int}^{e}}_{48\times 1} \tag{3.69}$$

In a symbolic writing by showing matrix positions of each node, the standard internal force vector maybe written as follows

$$\underbrace{(\boldsymbol{F}_{int}^{e})^T}_{1\times 24} = \{\underbrace{(\boldsymbol{F}_1)^T}_{1\times 6}, \underbrace{(\boldsymbol{F}_2)^T}_{1\times 6}, \underbrace{(\boldsymbol{F}_3)^T}_{1\times 6}, \underbrace{(\boldsymbol{F}_4)^T}_{1\times 6}\} \tag{3.70}$$

where $\boldsymbol{F}_1, ..., \boldsymbol{F}_4$ are nodal internal force vectors. In the same manner, the internal force vector of surrounding nodes can be written as follows,

$$\underbrace{\left(\hat{\boldsymbol{F}}^e_{int}\right)^T}_{1\times 48} = \{\underbrace{(\boldsymbol{F}_6)^T}_{1\times 6}, \underbrace{(\boldsymbol{F}_7)^T}_{1\times 6}, \underbrace{(\boldsymbol{F}_9)^T}_{1\times 6}, \underbrace{(\boldsymbol{F}_{10})^T}_{1\times 6}, \underbrace{(\boldsymbol{F}_{12})^T}_{1\times 6}, \underbrace{(\boldsymbol{F}_{13})^T}_{1\times 6}, \underbrace{(\boldsymbol{F}_{15})^T}_{1\times 6}, \underbrace{(\boldsymbol{F}_{16})^T}_{1\times 6}\} \tag{3.71}$$

For the assembly procedure, let consider the patch of elements and nodes from $1, ...16$ as shown in Figure 3.18, the corresponding global internal force vector of size $16 \times 6 = 96$ which results from the assembly procedure is always stored in chronological order of nodes $1, 2, 3, ..., 16$.

Therefore, during the assembly process of enriched element e, one has to localize the right number of equation corresponding to each extra-dof in the global table, which can be represented as follows,

$$\begin{aligned}\underbrace{(\boldsymbol{F}_{int})^T}_{1\times 96} = \{&\underbrace{(\boldsymbol{F}_1)^T}_{1\times 6}, \underbrace{(\boldsymbol{F}_2)^T}_{1\times 6}, \underbrace{(\boldsymbol{F}_3)^T}_{1\times 6}, \underbrace{(\boldsymbol{F}_4)^T}_{1\times 6}, \underbrace{\boldsymbol{0}}_{1\times 6}, \underbrace{(\boldsymbol{F}_6)^T}_{1\times 6}, \underbrace{(\boldsymbol{F}_7)^T}_{1\times 6}, \underbrace{\boldsymbol{0}}_{1\times 6},\\ &\underbrace{(\boldsymbol{F}_9)^T}_{1\times 6}, \underbrace{(\boldsymbol{F}_{10})^T}_{1\times 6}, \underbrace{\boldsymbol{0}}_{1\times 6}, \underbrace{(\boldsymbol{F}_{12})^T}_{1\times 6}, \underbrace{(\boldsymbol{F}_{13})^T}_{1\times 6}, \underbrace{\boldsymbol{0}}_{1\times 6}, \underbrace{(\boldsymbol{F}_{15})^T}_{1\times 6}, \underbrace{(\boldsymbol{F}_{16})^T}_{1\times 6}\}\end{aligned} \tag{3.72}$$

As it can be seen from Eq(3.51), localization number of starting internal force vector of surrounding node number 6 is in this case $31 = 5 \times 6 + 1$ and for example localization number of starting internal force vector of surrounding node number 15 is in this case $85 = 14 \times 6 + 1$.

As it can be observed, the above assembly procedure is complex, and it represents probably one of the major drawbacks of the interpolation covers method. This is mainly true when one needs to implement it in commercial codes using the parallel multi thread computing. In fact Faurecia Automotive Seating imposes the use of the Massively Parallel Processing (MPP) version of Ls-dyna 6.1.2 and unfortunately it was not possible to retrieve the localization numbers of surrounding nodes. Indeed, nodes are distributed randomly between different processors and it was not possible to have access to the desired node localization during the assembly procedure.

Nevertheless, the above assembly procedure for enriched elements, has been developed for the general case and has been implemented in an in-house code.

3.2.3 Numerical validation

Some numerical academic applications are presented here to show the effectiveness of the ICM. Results will be compared to those obtained using reference analytical solutions and to those obtained using refined mesh solutions of Ls-dyna commercial code.

3.2.3.1 Plate with a hole

The first numerical application concerns a plate with a central hole under tensile loading given in Figure 3.19.
Plane stress condition is used with material data corresponding to $E = 72E9Pa$, $\nu = 0$ and distributed load $p = 100N/m$ and thickness is taken as unity. Only quarter of the plate is modeled due to symmetry. Seven different mesh schemes are opted to get converged solution and four of them are shown in Figure 3.20. There are 74000, 115625 and 462500 number of elements used to model the Mesh 5, Mesh 6 and Mesh 7, respectively.

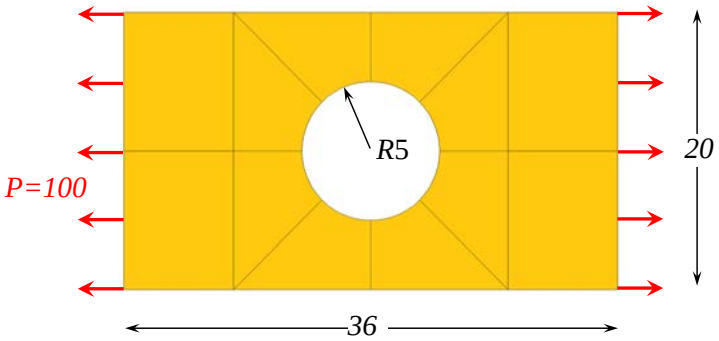

Figure 3.19: Plate with a central hole under tensile loading.

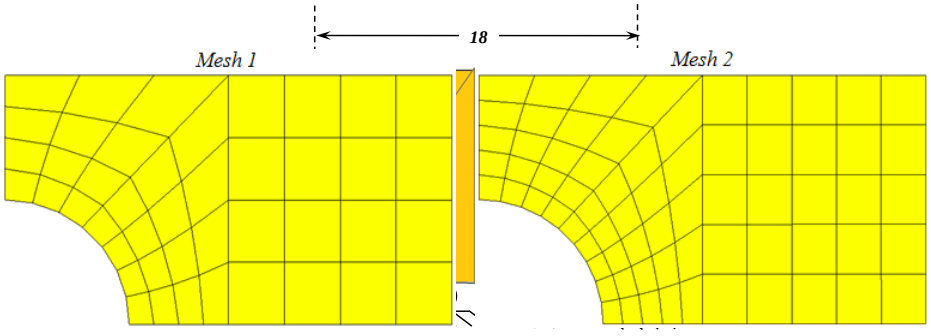

(a) Total number of elements are 44. (b) Total number of elements are 70.

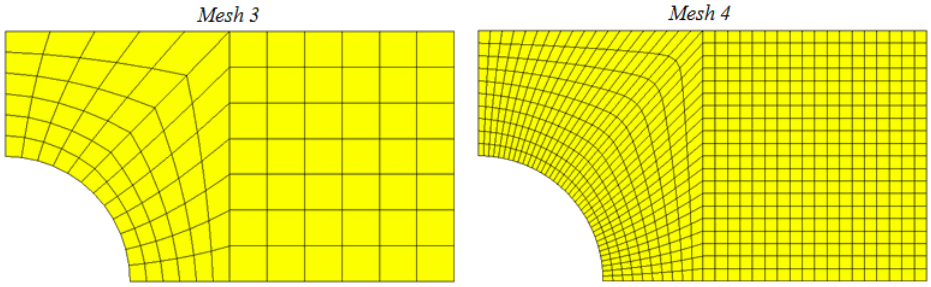

(c) Total number of elements are 114. (d) Total number of elements are 750.

Figure 3.20: Plate with a hole featuring four different mesh schemes.

The von-Mises stress distribution along the Y-axis, are plotted in Figure 3.21, for the different meshes of Ls-dyna. We can observe the converged solution of Ls-dyna is obtained for Mesh 7, it will be taken as reference solution for comparison.

Von-Mises stress obtained by ICM in Mesh 1 case is compared with Ls-dyna in Figure 3.22. Four nearest neighboring nodes are selected to enrich one element highlighted by black circle as depicted in Figure 3.22(a) with an error of -1.15% compared to Ls-dyna result with -28.74% error with the same mesh (Figure 3.22(b)).

Von-Mises stresses of ICM and Ls-dyna are compared with the reference solution and plotted along Y-axis from the hole in Figure 3.23.

In Mesh 2, the solution of ICM shows improved von-Mises stress with a decreased error of 0.11% whereas it is of 24.14% for Ls-dyna (Figure 3.24). von-Mises stress solutions of ICM and Ls-dyna are plotted and compared to the reference solution are given in Figure 3.25.

When using the Mesh 3, the ICM solution gives an error of 1.07% while Ls-dyna solution is still

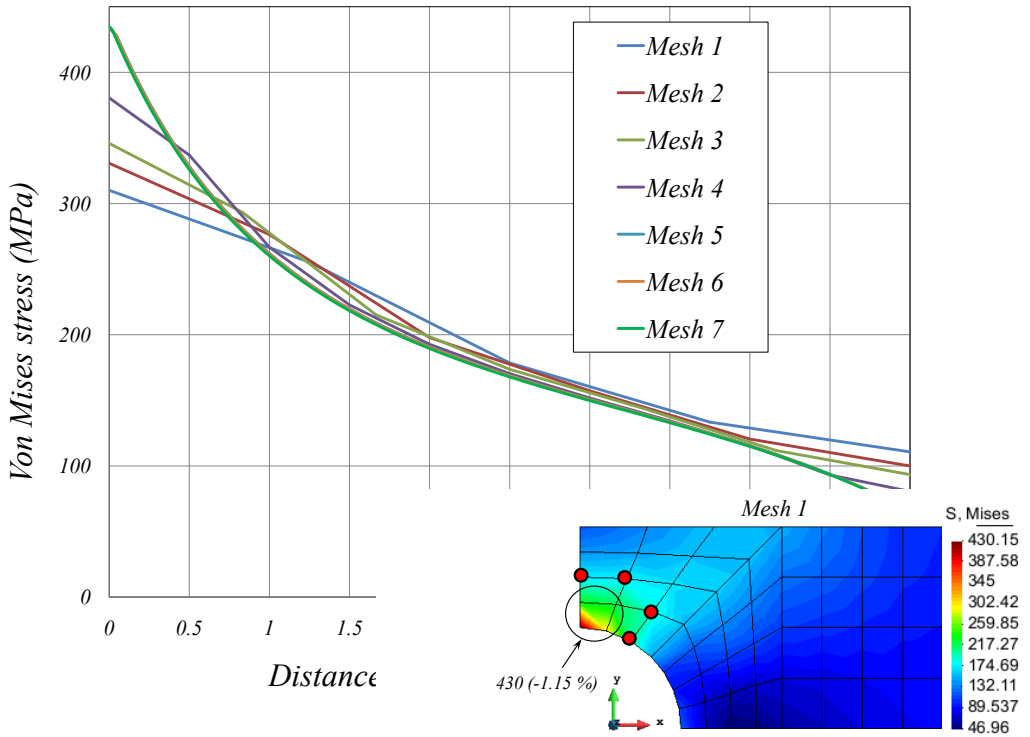

Figure 3.21: von-M

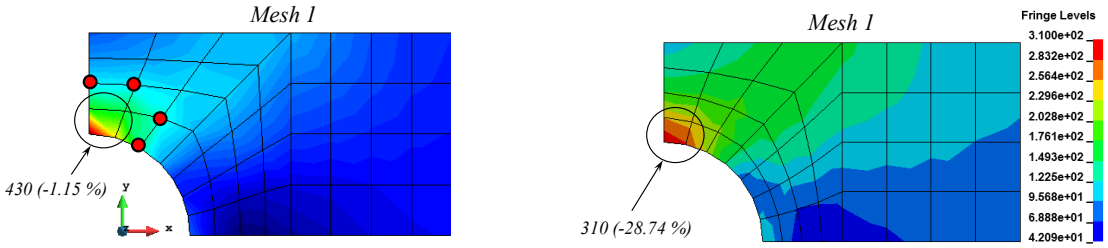

(a) ICM solution.

(b) Ls-dyna solution.

Figure 3.22: von-Mises stress distribution along Y-axis for Mesh 1.

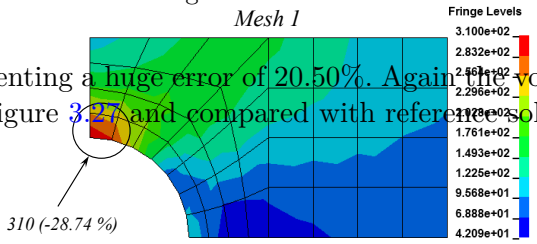

presenting a huge error of 20.50%. Again the von-Mises stresses of ICM and Ls-dyna are plotted in Figure 3.27 and compared with reference solution corresponding to the refine mesh.

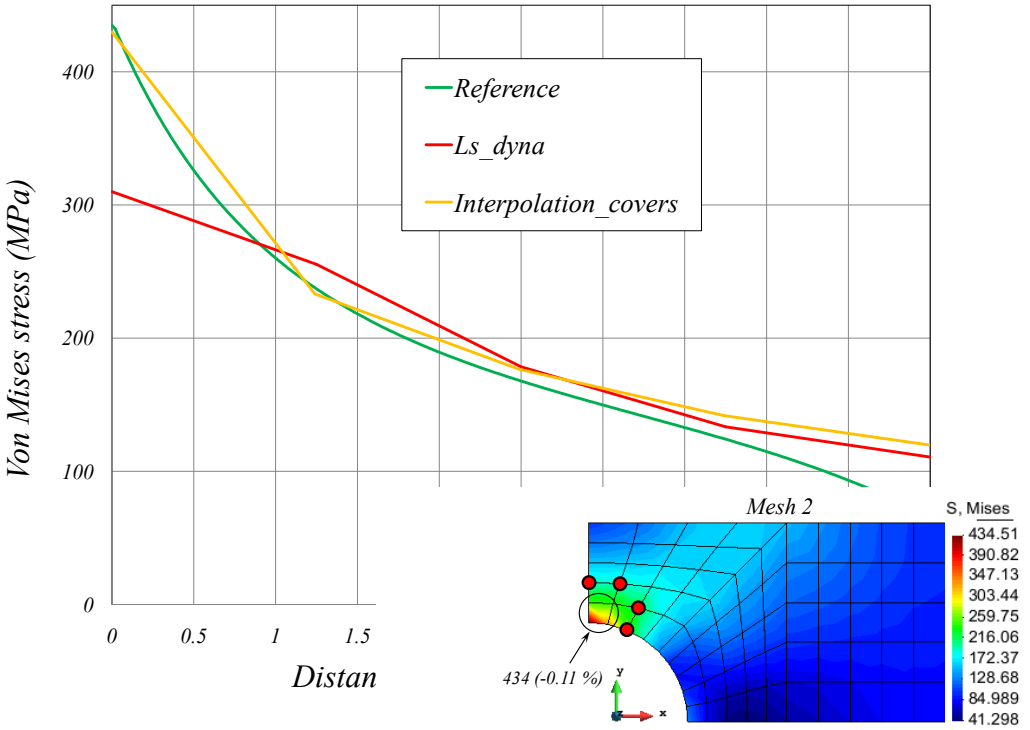

Figure 3.23: von-Mises st

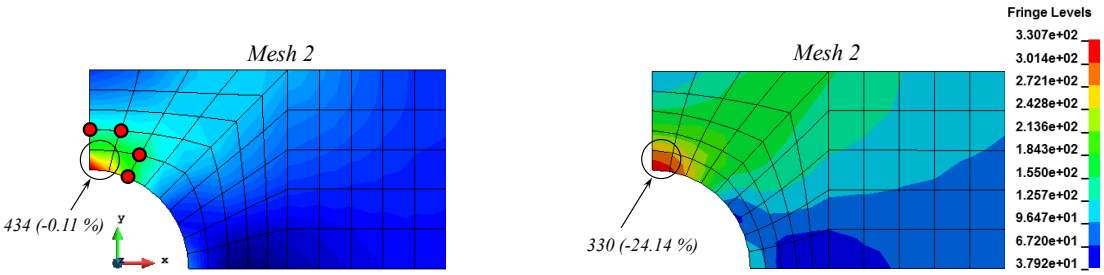

(a) ICM solution. (b) Ls-dyna solution.

Figure 3.24: von-Mises stress distribution along Y-axis for Mesh 2.

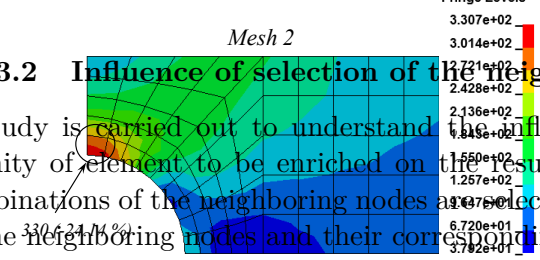

3.2.3.2 Influence of selection of the neighboring nodes

A study is carried out to understand the influence of selection of surrounding nodes in the vicinity of element to be enriched on the results in ICM. Mesh 3 is used and three different combinations of the neighboring nodes are selected for this investigation. All three combinations of the neighboring nodes and their corresponding von-Mises stresses are given in Figure 3.28. Figure 3.29 shows the von-Mises stress variation along Y-axis, we can observe that neighboring nodes to enrich the element can influence the results and the best possible results can be obtained by choosing the closest nodes (1st nearest) to the target element.

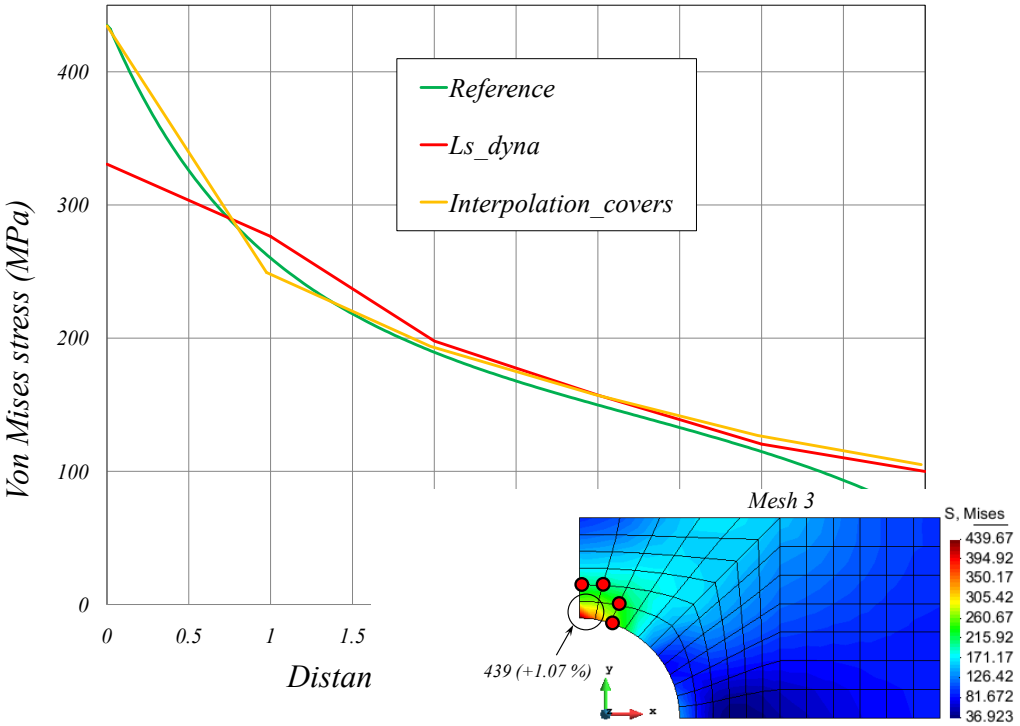

Figure 3.25: von-Mises st

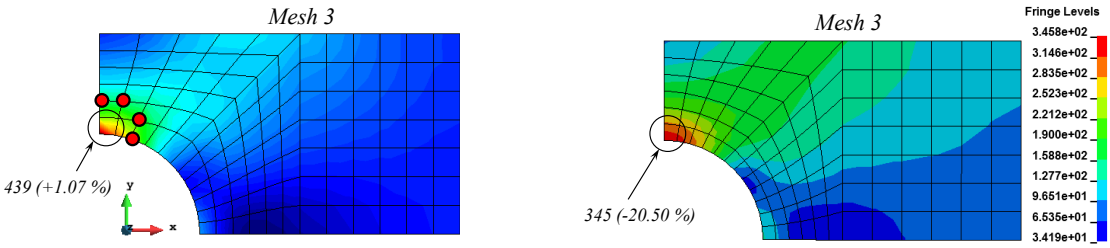

(a) ICM solution. (b) Ls-dyna solution.

Figure 3.26: von-Mises stress distribution along Y-axis for Mesh 3.

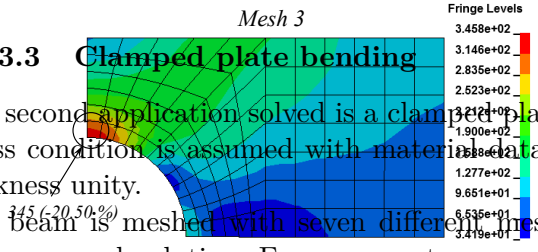

3.2.3.3 Clamped plate bending

The second application solved is a clamped plate under bending as shown in Figure 3.30. Plane stress condition is assumed with material data of $E = 72E9Pa$, $\nu = 0$ and $F = 100N$ with a thickness unity.

The beam is meshed with seven different mesh schemes by doing gradual refinement to find the converged solution. Four amongst seven meshes with their total number of elements are presented in the Figure 3.31. There are 1080, 27000 and 108000 number of elements used to model the Mesh 5, Mesh 6 and Mesh 7, respectively. Von-Mises stress plots corresponding to all these seven mesh schemes are shown in the Figure 3.32. Von-Mises stress obtained by Mesh 7 with 108000 total number of elements is taken as reference solution.

Mesh 1, Mesh 2 and Mesh 3 from the Figure 3.31 are selected to study and compare the results between ICM and Ls-dyna. At first, two corner elements near the clamp, where maximum stress concentration is witnessed, in Mesh 1 are enriched by using four additional surrounding nodes for

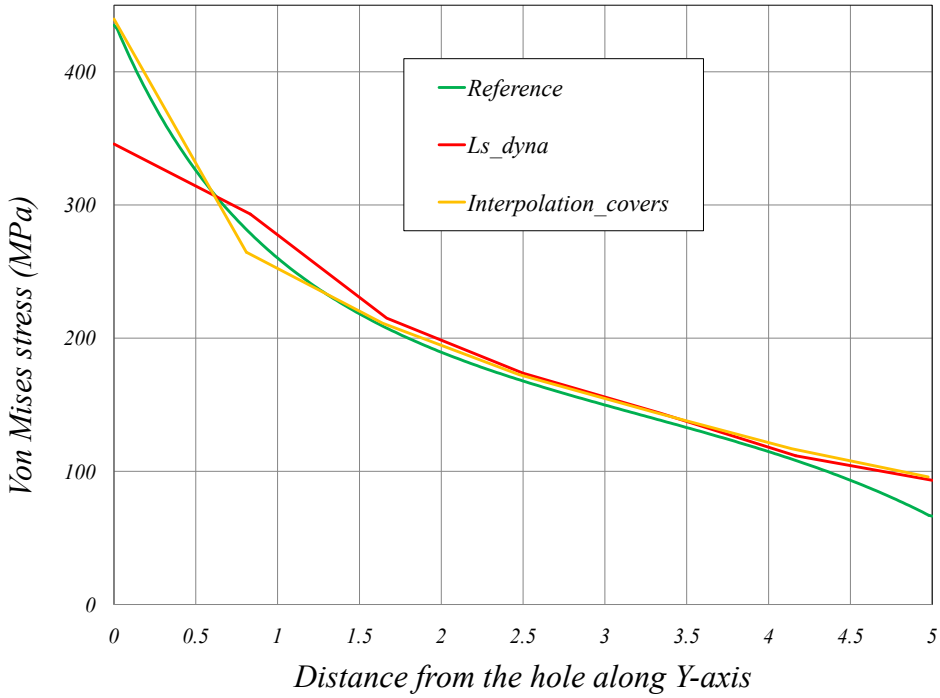

Figure 3.27: von-Mises stress distribution along Y-axis for Mesh 3.

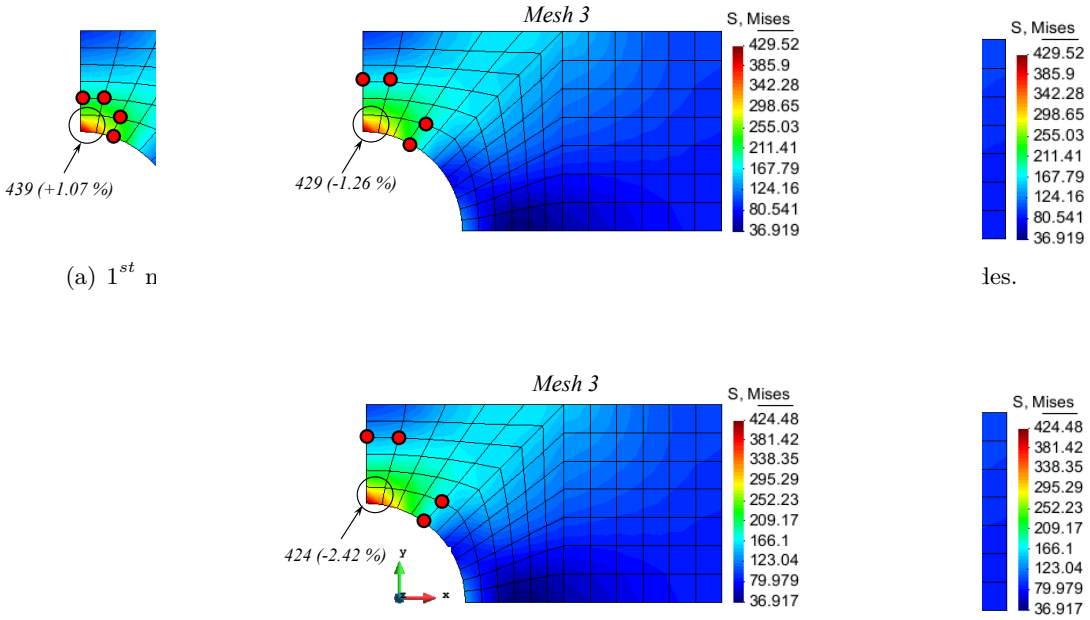

(a) 1^{st} n

les.

(c) 3^{rd} nearest neighbouring nodes.

Figure 3.28: Von-Mises stress distribution: influence of neighboring nodes.

each element. Two elements that need to be enriched are highlighted by black circles in Figure 3.33(a). In Mesh 1 case, ICM shows improvement in von-Mises stress compared to Ls-dyna and error percentage is -15.29% whereas it is -31.62% in Ls-dyna solution as shown in Figure 3.33. Von-Mises stresses of ICM and Ls-dyna are plotted and compared with the reference in Figure

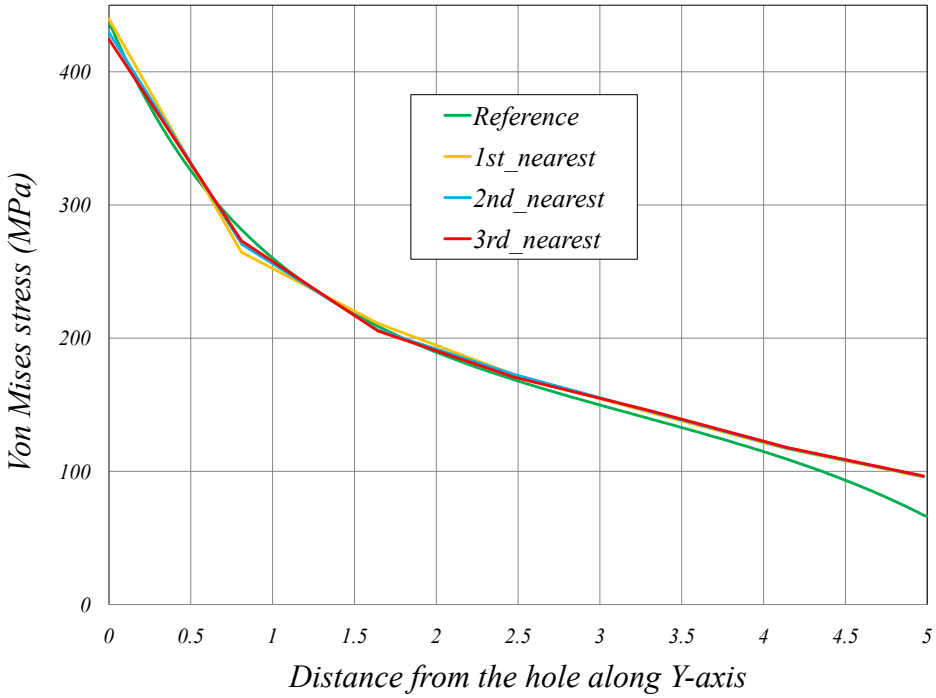

Figure 3.29: Von-Mises stress distribution along Y-axis in Mesh 3.

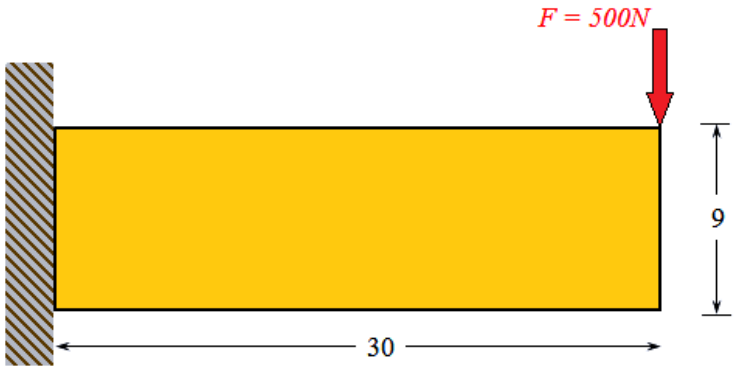

Figure 3.30: Clamped beam under application of transverse load.

3.34.

Von-Mises stress is increased by using ICM in Mesh 2 and error percentage is decreased from -24.34% in Ls-dyna solution to -9.93% as shown in Figure 3.35. Von-Mises stresses obtained by ICM and ls-dyna are plotted as a function of distance along Y-axis and compared with reference solution in Figure 3.36.

In Mesh 3, even more improved von-Mises stress is obtained by using ICM and error percentage is decreased from -20.12% in Ls-dyna solution to -7.04% as depicted in Figure 3.37. Von-Mises plot comparison between ICM and Ls-dyna solution and reference solution is shown in Figure 3.38.

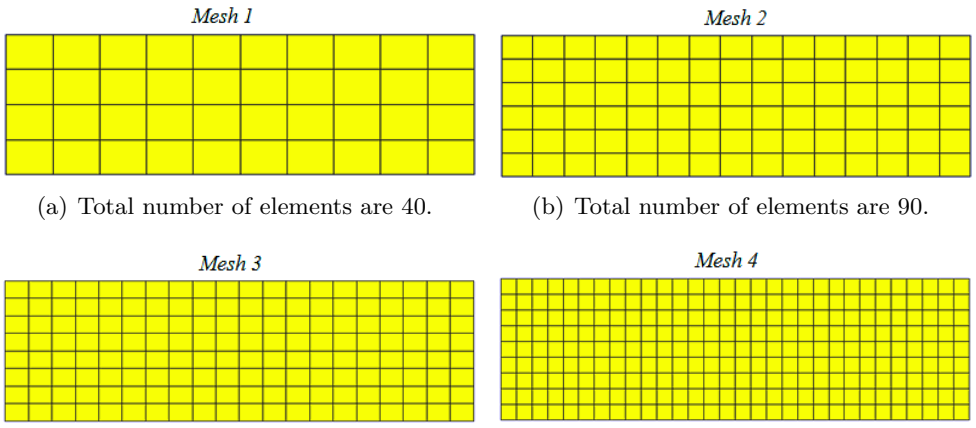

(a) Total number of elements are 40. (b) Total number of elements are 90.

(c) Total number of elements are 160. (d) Total number of elements are 270.

Figure 3.31: Clamped beam featuring four different mesh schemes.

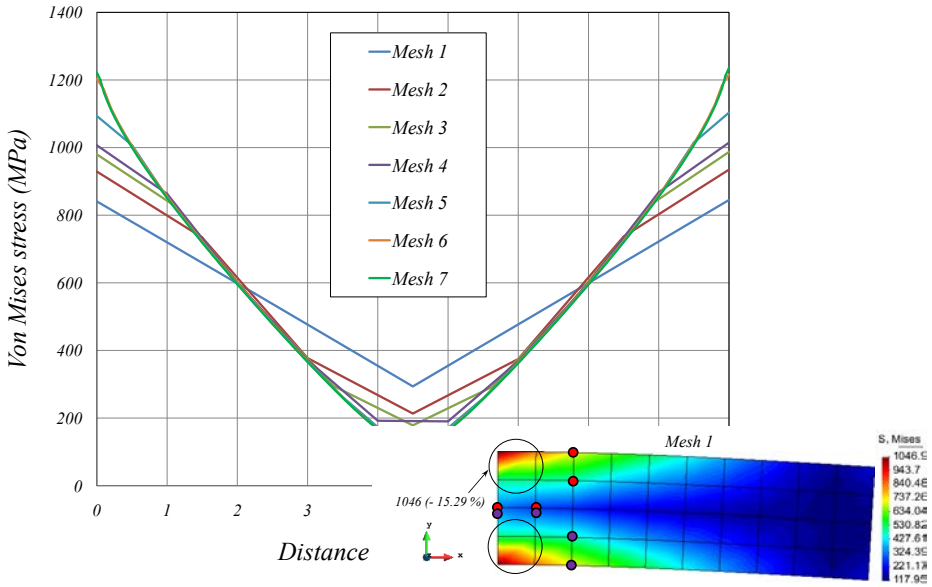

Figure 3.32: Von-Mises stress distrik

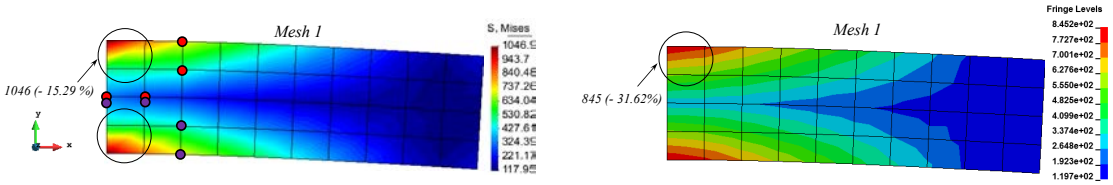

(a) ICM solution. (b) Ls-dyna solution.

Figure 3.33: Von-Mises stress contour maps of clamped beam in Mesh 1.

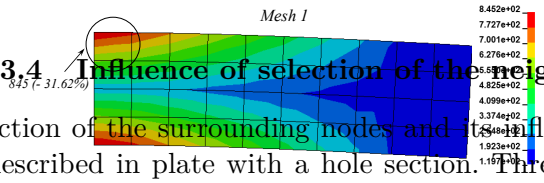

3.2.3.4 Influence of selection of the neighboring nodes

Selection of the surrounding nodes and its influence on the results is studied in the same way as described in plate with a hole section. Three different combinations of neighbouring nodes selection of Mesh 3 are examined as illustrated in Figure 3.39. Von-Mises stresses of ICM and

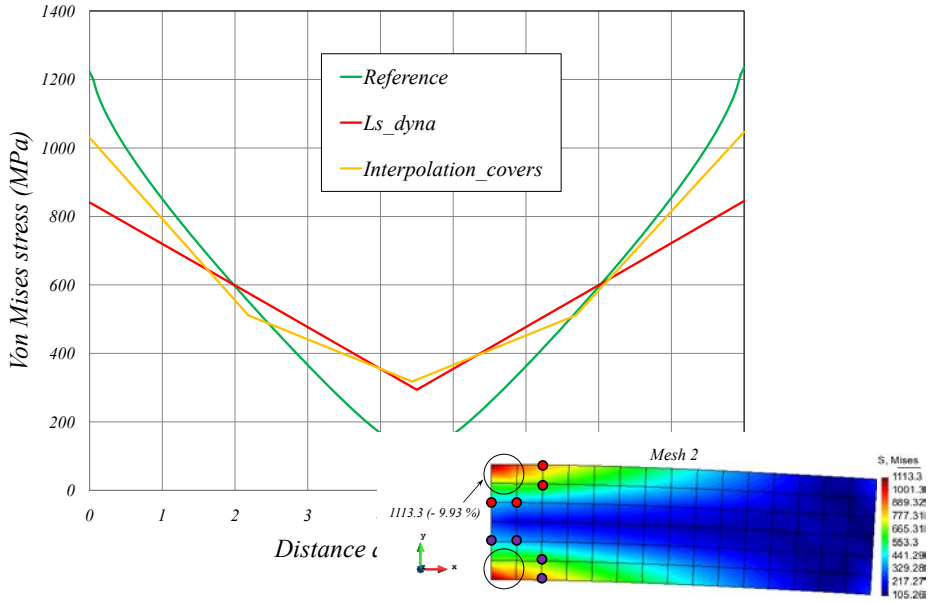

Figure 3.34: Von-Mises stress distribution

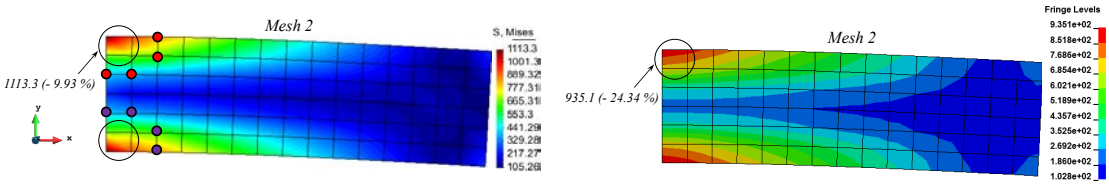

(a) ICM solution. (b) Ls-dyna solution.

Figure 3.35: Von-Mises stress contour maps of clamped beam in Mesh 2.

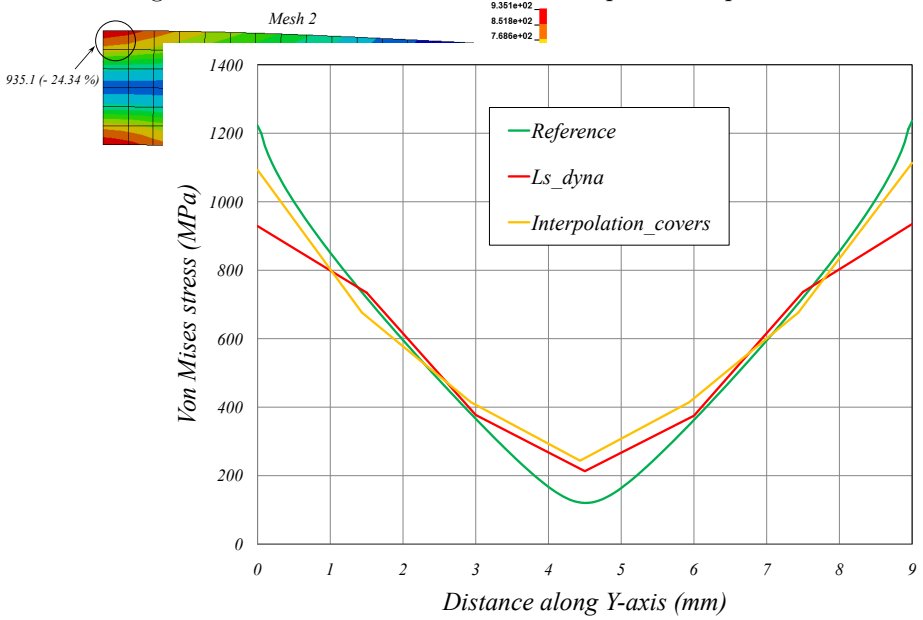

Figure 3.36: Von-Mises stress distribution of clamped beam along Y-axis in Mesh 2.

Ls-dyna are plotted as a function of distance along Y-axis and compared with reference result

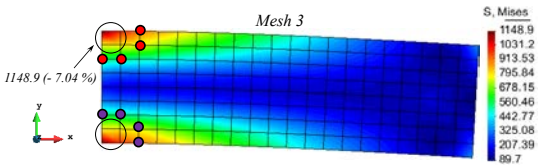

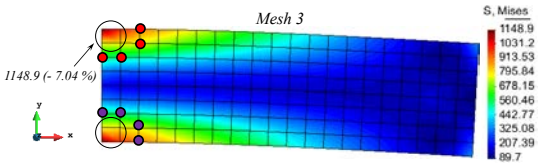

(a) ICM solution.

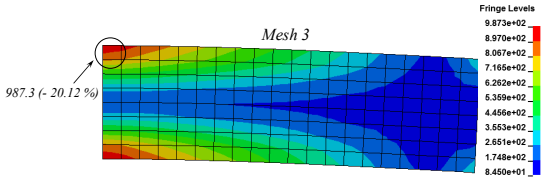

(b) Ls-dyna solution.

Figure 3.37: Von-Mises stress contour maps of clamped beam in Mesh 3.

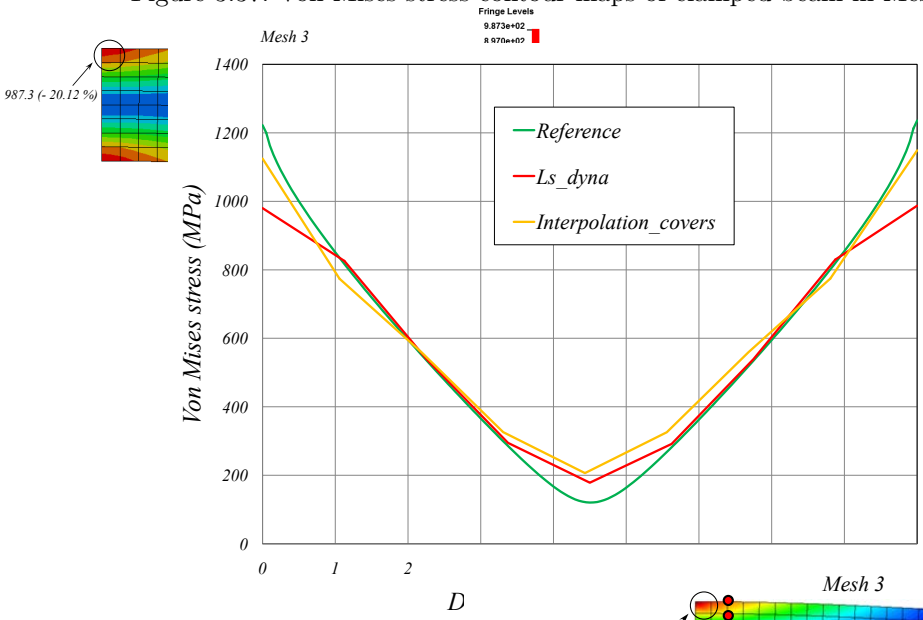

Figure 3.38: Von-Mises stress distr

as shown in Figure 3.40.

It is observed that the selection of 1*st* ne
value and decreased error percentage c
combinations. Von-Mises stress value sta
from the element that need to be enriche

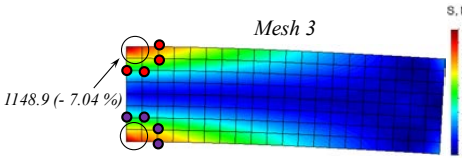

(a) 1^{st} nearest neighbouring nodes.

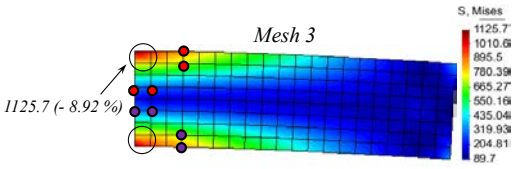

(b) 2^{nd} nearest neighbouring nodes.

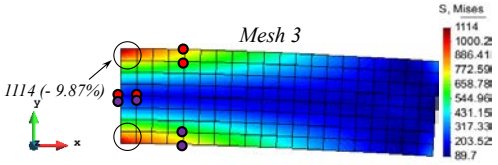

(c) 3^{rd} nearest neighbouring nodes.

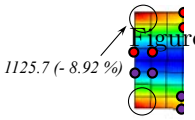

Figure 3.39: Von-Mises stress distribution: influence of surrounding nodes.

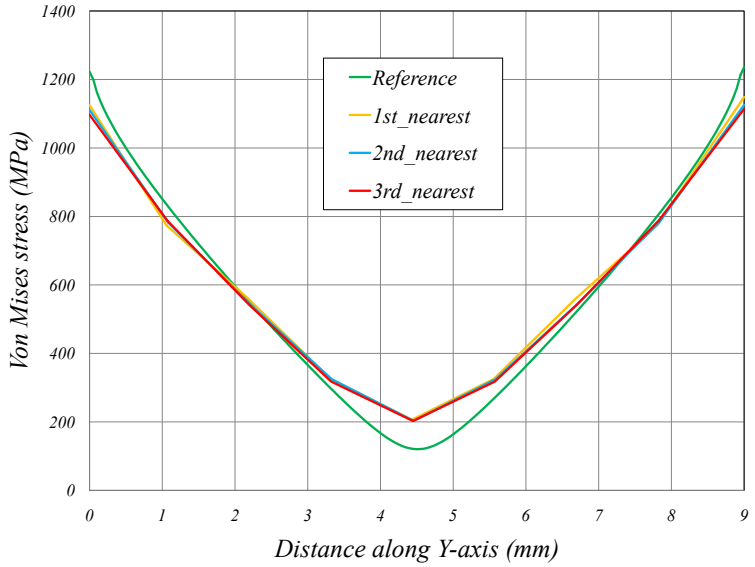

Figure 3.40: Von-Mises stress distribution along Y-axis in Mesh 3.

3.2.3.5 Tool jig

The third application concerns a tool jig plate under bending as shown in Figure 3.41. Plane stress condition is taken with material data of $E = 72E9Pa$, $\nu = 0$ and a distributed load of $p = 10N/m$. Tool jig structure is clamped from the left side and also one point is clamped at a distance of $20m$ from the left side.

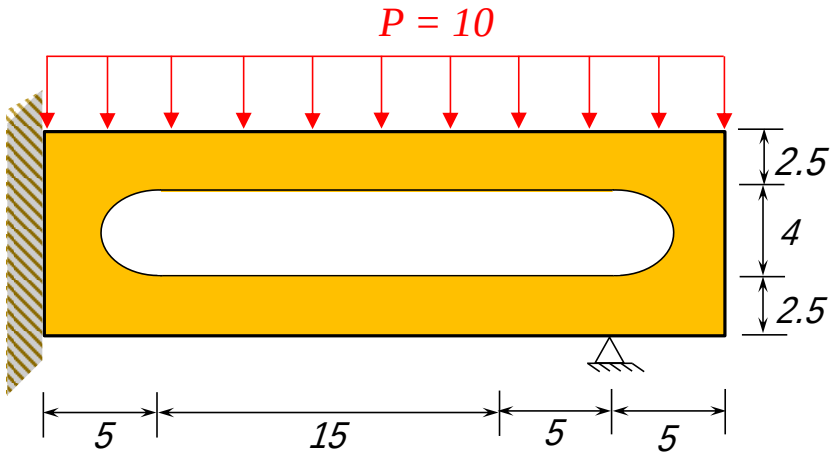

Figure 3.41: Tool jig geometry and boundary conditions.

Two different mesh schemes have been carried out as illustrated in Figure 3.42. The reference solution of the tool jig problem has been reported by Payen D.J. and Bathe K.J. [64] where the reference von-Mises stress on the right circular side is $609Pa$, whereas on the left circular side it is $563Pa$.

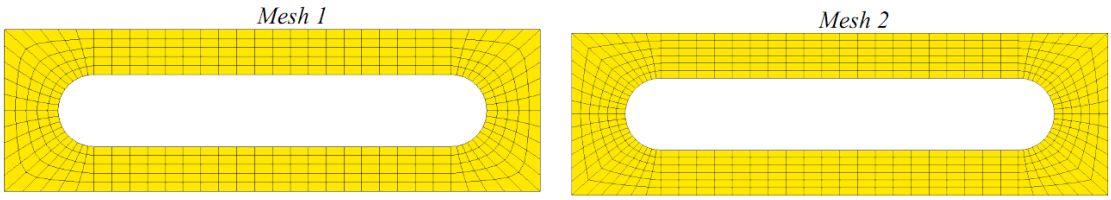

(a) Total number of elements are 400.

(b) Total number of elements are 528.

Figure 3.42: Tool jig problem featuring two different mesh schemes.

Figure 3.43(b) shows the von-Mises stress obtained by Ls-dyna where the maximum von-Mises stress values on the right and left circular sides of $408Pa$ and $377Pa$, respectively with an error of 33% on both sides. ICM improves the von-Mises stress as illustrated in Figure 3.43(a) with 12.5% and 8.9% respectively.
In Mesh 2 as illustrated in Figure 3.44(b), Ls-dyna shows von-Mises stress values of $451Pa$ on the right circular side with 25.9% error and $405Pa$ on the left circular side with 28.1%. ICM allows enhancement of the von-Mises stress as depicted in Figure 3.44(a) with values $584.8Pa$ and $547Pa$ with very low errors of 3.9% and 2.8% using the same mesh. This show the efficiency of the ICM in capturing stress gradients.

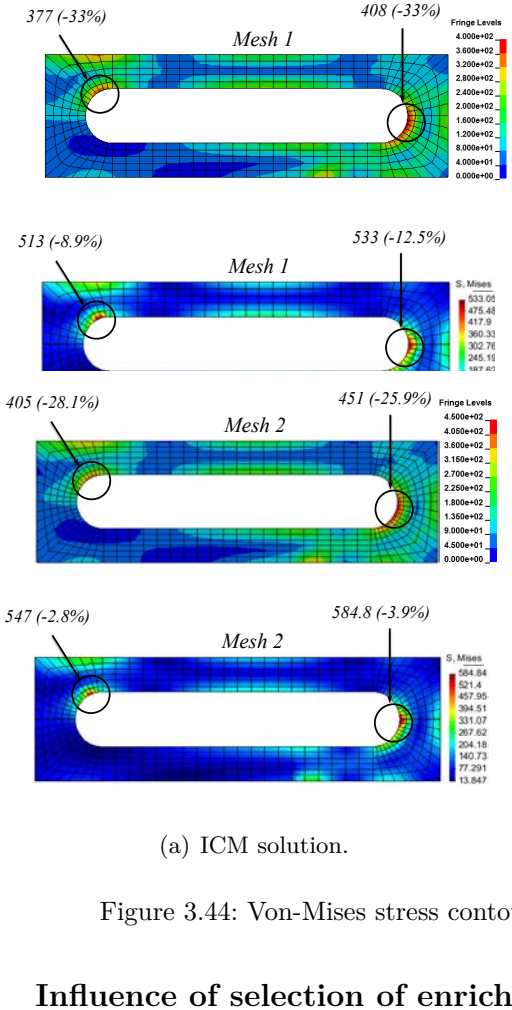

(a) ICM solution.

(b) Ls-dyna solution.

Figure 3.44: Von-Mises stress contour maps of tool jig problem in Mesh 1.

(a) ICM solution.

(b) Ls-dyna solution.

Figure 3.44: Von-Mises stress contour maps of tool jig problem in Mesh 2.

3.2.4 Influence of selection of enrichment terms

In this section, the influence of the enrichment polynomial basis is discussed. In the above section, four additional polynomial terms were selected for enrichment and it is designated as $Poly8$. In $Poly8$, four additional terms were added to the four classical terms of the standard Q4 shell element. These additional terms are

$$\widetilde{\boldsymbol{N}}_i = N_i \{\xi,\ \eta,\ \xi^2\eta,\ \xi\eta^2\}^T \tag{3.73}$$

These enrichment terms are extended to five in $Poly9$ as

$$\widetilde{\boldsymbol{N}}_i = N_i \{\xi,\ \eta,\ \xi^2\eta,\ \xi\eta^2,\ \xi^2\eta^2\}^T \tag{3.74}$$

In this case five extra nodes need to select for enrichment. The third case is $Poly10$ where six additional enrichment terms are added which are

$$\widetilde{\boldsymbol{N}}_i = N_i \{\xi,\ \eta,\ \xi^2\eta,\ \xi\eta^2,\ \xi^2\eta^2,\ \xi^n\eta^n\}^T \tag{3.75}$$

where the power n can be adjusted by the user to different values from $n = 3, 4, ...$ In $Poly10$, six additional nodes need to be selected to enrich one element.

Plate with a hole numerical application is seleted to study the all three enrichment cases of ICM. Von-Mises stress comparison between all the three cases is shown in Figure 3.45 where the maximum von-Mises stress value is not varying too much and error percentage is upto 1% in all the cases. The highest value of von-Mises stress is obtained by selecting four surrounding nodes in $Poly8$ whereas a little reduced von-Mises value is obtained in $Poly10$ where six surrouning nodes are used for enrichment. Selecting surrounding nodes far from the enriched element results reduced von-Mises stress value in $Poly10$.

Von-Mises stress comparison between three enrichment cases of ICM, Ls-dyna and reference solution is carried out in three numerical applications as illustrated in Table 3.4. The selection of the number of surrounding nodes may influence slightly the results. For instance in plate with

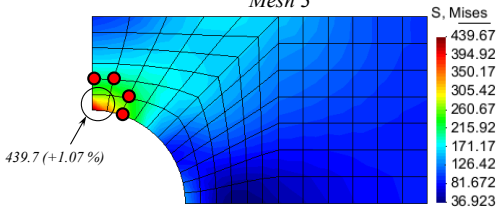

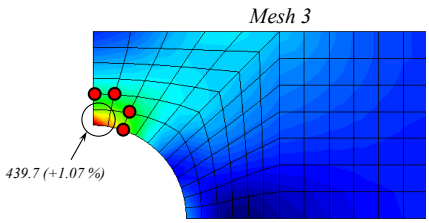

(a) Poly8.

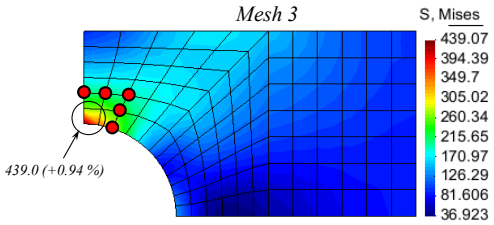

(b) Poly9.

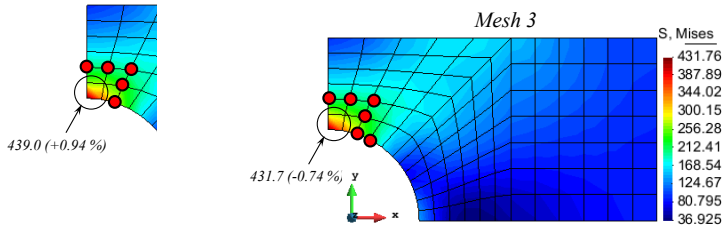

(c) Poly10.

Figure 3.45: Von-Mises stress distribution : Influence of polynomial enrichment bases.

Table 3.4: Von-Mises stress comparison : ICM vs. Ls-dyna

	Plate with a hole	Error %	Clamped beam	Error %	Tool jig	Error %
Reference	435		1236		609	
Ls-dyna	345.8	-20.5%	987.3	-20.12%	450	-26.11%
Poly8	439.67	+1.07%	1148.9	-7.04%	584.8	-3.97%
Poly9	439.07	+0.94%	1150.9	-6.89%	585	-3.94%
Poly10	431.76	-0.74%	1154.3	-6.61%	613	+0.66%

a hole example, even *Poly*8 shows improved von-Mises stress close to reference solution whereas in tool jig numerical application, six surrounding nodes need to select for enrichment e.g. *Poly*10 to get von-Mises stress closer to the reference solution.

3.3 Concluding remarks

In the beginning of this chapter, the formulation of developed shell element is presented. The formulation of the developed shell element is based on the Reissner–Mindlin assumptions of "material fibres originally straight and normal to the shell mid-surface do not stretch and remain straight" and "zero stress normal to the shell mid-surface". This four node shell element possess six degrees of freedom per node with a quadratic representation on z of the strains and implicit integration along the thickness. This element can be used for the analysis of thin and thick shells and it is also capable to solve linear and non linear problems effectively. Three different numerical applications of developed shell elements are presented and their results are compared with ABAQUS shell elements S4 and with analytical reference solutions. The developed shell elements showed more accurate results and gave faster solution convergence compared to ABAQUS S4 shell elements.

Interpolation covers method (ICM) is detailed to enrich the standard 4-node shell elements. The

ICM is capable to improve the solution accuracy without mesh refinement procedure. The main idea of the ICM is to use new set of interpolation cover functions developed over patches of elements along with standard FE shape functions. The efficiency of the proposed enrichment method is demonstrated by using three different numerical applications. The results obtained by ICM are compared with the Ls-dyna and reference solutions which showed that ICM is capable to capture the stresses accurately even with the coarser mesh size.
The influence of the selection of nearest neighbouring nodes on the solution accuracy is also studied and the investigation showed that the solution accuracy decreased by selecting the nodes which are far from the enriched element. Three ICM enrichment techniques named $Poly8$, $Poly9$ and $Poly10$ depending on the number of the neighbouring nodes selected for enrichment are presented and comparison of results is carried out between these three enrichment techniques.

Multimaterial model for laser welding

This chapter presents the formulation of a multimaterial nonlinear model based on an elasto-plastic behavior including ductile damage. The interest here is to be able to develop a multimaterial model which can be used within the same shell element to be able to model with the same element the realistic behavior of both HAZ and BM zone of a welded joint. The multimaterial model has been implemented within the Ls-dyna commercial software as a UMAT.
The need of such UMAT development was necessary because Faurecia Automotive Seating company needed to use a very coarse mesh with the ability to represent correctly the physical behavior of the welded joints, especially at the transition zone between BM and the HAZ where fracture has been observed experimentally. This first part of development allowed to obtain a numerical model which improves the stress and plastic strain gradient at the transition zone.
In order to be able to capture the initiation of material failure, which has been observed experimentally, a damage model has been developed and implemented within the multimaterial model. The damage model belongs to the phenomenological family known in the literature as the Generalized Incremental Stress State dependent damage Model. In order to be able to take into account correctly triaxiality of stresses an approximation of the transverse stress (through thickness) has been introduced. The accuracy of damage model used with the "*Shell Coarse Model*" is shown through the use of academic two-beam bending problem as well as on the WSII benchmark.

4.1 User defined material model

Prior to the description of the multimaterial model, a first step was the development of a User defined Material model based on elasto-plastic behavior has been developed within Ls-dyna commercial software. Indeed this User material model will be used to evaluate stresses and plastic strains of the BM and the HAZ separately.

4.1.1 Basic assumptions

As the used materials for car seat are mostly based on steel families ($S420$, $S500$,...), a choice of ductile behavior has been done based on the following assumptions:

- The plastic behavior is based on the incremental flow theory.
- The formulation is based on plane stress condition.
- Assumption of an isotropic hardening is retained.
- The classical von-Mises criterion is retained.

- The stresses integration is carried out implicitly insuring iteratively the consistency condition.

4.1.2 Stress integration for elasto-plastic Shells

The starting point for elasto-plastic relations applied for shell structures is the fundamental assumption of strain rate split into elastic part $\dot{\boldsymbol{\varepsilon}}^e$ and a plastic one $\dot{\boldsymbol{\varepsilon}}^p$, as

$$\dot{\boldsymbol{\varepsilon}} = \dot{\boldsymbol{\varepsilon}}^e + \dot{\boldsymbol{\varepsilon}}^p \tag{4.1}$$

where $\dot{\boldsymbol{\varepsilon}}$ is the strain rate 5×1 vector as decribed in the previous chapter. It accounts for the three local in-plane strain rate components $\dot{\varepsilon}_x, \dot{\varepsilon}_y, \dot{\gamma}_{xy}$ and two shear strain rate components namely $\dot{\gamma}_{xz}$ and $\dot{\gamma}_{yz}$, hence we have $\dot{\boldsymbol{\varepsilon}} = \{\dot{\varepsilon}_x, \dot{\varepsilon}_y, \dot{\gamma}_{xy}, \dot{\gamma}_{xz}, \dot{\gamma}_{yz}\}^T$.
Taking into account Eq.(4.1), the elastic stress-strain relationship can be rewritten as

$$\dot{\boldsymbol{\sigma}} = \mathbb{D}^e \ (\dot{\boldsymbol{\varepsilon}} - \dot{\boldsymbol{\varepsilon}}^p) \tag{4.2}$$

where $\dot{\boldsymbol{\sigma}}$ is the stress rate vector accounting for five stress rate components according to the plane stress condition ($\dot{\sigma}_z = 0$) i.e. $\dot{\boldsymbol{\sigma}} = \{\dot{\sigma}_x, \dot{\sigma}_y, \dot{\sigma}_{xy}, \dot{\sigma}_{xz}, \dot{\sigma}_{yz}\}^T$; $\mathbb{D}^e$ is the material elastic tensor supposed here isotropic and homogeneous and can be defined by the Young's modulus E and the Poisson ratio ν.
Plastic strain rates for associated plasticity are assumed to follow the normality relation

$$\dot{\boldsymbol{\varepsilon}}^p = \dot{\lambda}\, \boldsymbol{a}; \qquad \text{with} \qquad \boldsymbol{a} = \frac{\partial F}{\partial \boldsymbol{\sigma}} \tag{4.3}$$

with F the plastic potential surface expressed here as the classical von-Mises criterion, $\dot{\lambda}$ the plastic multiplier or consistency parameter which represents the magnitude of plastic flow satisfying the condition $\dot{\lambda} \geq 0$, $\boldsymbol{a}$ is the flow direction which is obtained upon differentiation of the plastic potential function with respect to stress components. The use of an associated flow rule ensures that plastic strain-increments are perpendicular to the flow surface.
The consistency condition $\dot{F} = 0$ allows to write $\boldsymbol{a}^T \cdot \dot{\boldsymbol{\sigma}} = 0$ and hence we have :

$$\dot{\lambda} = \frac{\boldsymbol{a}^T\, \mathbb{D}^e\, \dot{\boldsymbol{\varepsilon}}}{\boldsymbol{a}^T\, \mathbb{D}^e\, \boldsymbol{a}} \tag{4.4}$$

It is important to notice that equation Eq.(4.4) is nonlinear since the vector $\boldsymbol{a}$ is dependent on the stress state which are dependent on $\dot{\lambda}$ through Eq.(4.3).
Substituting Eq.(4.4) into Eq.(4.3), we have

$$\dot{\boldsymbol{\varepsilon}}^p = \frac{\boldsymbol{a}^T\, \mathbb{D}^e\, \dot{\boldsymbol{\varepsilon}}}{\boldsymbol{a}^T\, \mathbb{D}^e\, \boldsymbol{a}}\, \boldsymbol{a} \tag{4.5}$$

Finally by substituting Eq.(4.5) into Eq.(4.2), we obtain the continuum elastoplastic tangent modulus, given by:

$$\dot{\boldsymbol{\sigma}} = \mathbb{D}^{ep}\, \dot{\boldsymbol{\varepsilon}} \qquad \text{with} \qquad \mathbb{D}^{ep} = \mathbb{D}^e - \frac{\mathbb{D}^e\, \boldsymbol{a}\, \boldsymbol{a}^T\, \mathbb{D}^e}{\boldsymbol{a}^T\, \mathbb{D}^e\, \boldsymbol{a}} \tag{4.6}$$

4.1.3 Numerical integration of stresses

Relations given above have been determined as rates of strains and stresses and it is important to calculate the finite stress/strain increments between two time step increments n and $n+1$.

At the beginning of time step $n+1$, the strain increments $\Delta\boldsymbol{\varepsilon}$ are being given, then a trial stress state can be evaluated using :

$$\boldsymbol{\sigma}_{n+1}^{trial} = \boldsymbol{\sigma}_n + \mathbb{D}^e \, \Delta\boldsymbol{\varepsilon} \tag{4.7}$$

Then the potential flow criterion should be checked

$$F_{n+1} = F\left(\boldsymbol{\sigma}_{n+1}\right) \leq 0 \quad ? \tag{4.8}$$

If condition Eq.(4.8) is satisfied then no plastic strain occurred and stress state increment is accepted. Contrarily if the flow criterion Eq.(4.8) is violated, a plastic correction is needed in order to calculate the plastic multiplier increment $\Delta\lambda$ and the corresponding stress increment $\Delta\boldsymbol{\sigma}$.
To this end, we write the plastic strain and the yield condition updates in

$$\begin{array}{l} \boldsymbol{\varepsilon}_{n+1}^p = \boldsymbol{\varepsilon}_n^p + \Delta\lambda \, \boldsymbol{a} \Rightarrow \boldsymbol{r} = -\boldsymbol{\varepsilon}_{n+1}^p + \boldsymbol{\varepsilon}_n^p + \Delta\lambda \, \boldsymbol{a} = \boldsymbol{0} \\ F = F_{n+1} = F\left(\boldsymbol{\sigma}_{n+1}\right) = 0 \end{array} \tag{4.9}$$

Linearizion of Eq.(4.8) allows the use of Newton-Raphson iterative prediction of the plastic multiplier increment $\Delta\lambda$ and the corresponding stress state $\boldsymbol{\sigma}$ at each iteration (k) as follows:

$$\begin{array}{l} \Delta\lambda^{(k+1)} = \Delta\lambda^{(k)} + \delta\lambda^{(k)} \\ \boldsymbol{\sigma}^{(k+1)} = \boldsymbol{\sigma}^{(k)} + \Delta\boldsymbol{\sigma}^{(k)} \end{array} \tag{4.10}$$

with

$$\begin{aligned} \delta\lambda^{(k)} &= \frac{F_{(k)} - \boldsymbol{a}^{(k)^T} \, \mathbb{R}^{(k)} \, \boldsymbol{r}^{(k)}}{\boldsymbol{a}^{(k)^T} \, \mathbb{R}^{(k)} \, \boldsymbol{a}^{(k)}} \\ \mathbb{R}^{(k)} &= \left[\mathbb{I} + \Delta\lambda^{(k)} \mathbb{D}^e \frac{\partial \boldsymbol{a}^{(k)}}{\partial \boldsymbol{\sigma}}\right]^{-1} \mathbb{D}^e \end{aligned} \tag{4.11}$$

Once the plastic multiplier is obtained the stress increment can be deduced iteratively using:

$$\Delta\boldsymbol{\sigma}^{(k)} = -\mathbb{R}^{(k)} \left(\boldsymbol{r}^{(k)} + \delta\lambda^{(k)} \, \boldsymbol{a}^{(k)}\right) \tag{4.12}$$

During the iteration process, the consistent elasto-plastic tensor can be calculated at each iteration by

$$\mathbb{D}^{ep} = \mathbb{R}^{(k)} - \frac{\mathbb{R}^{(k)} \, \boldsymbol{a}^{(k)} \, \boldsymbol{a}^{(k)^T} \, \mathbb{R}^{(k)}}{\boldsymbol{a}^{(k)^T} \, \mathbb{R}^{(k)} \, \boldsymbol{a}^{(k)}} \tag{4.13}$$

4.1.4 Thickness change calculation

During impact and crash simulation large membrane stretching often occur and as consequence large thickness change has to be taken into account. The general procedure used to update the thickness is based on an accurate calculation of the normal strain component ε_z in a post-processing step. This strain component requires an iterative update for an elasto-plastic material behaviour.

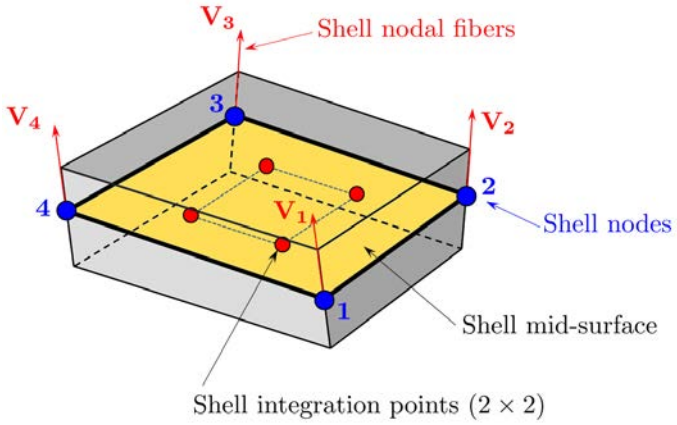

Figure 4.1: Thickness change calculation in a 4-node shell element.

At first, the strain increment tensor $\Delta\boldsymbol{\varepsilon}_n$ over a time step n is computed at each integration point based on the use of plane stress condition in shells. The mean value of $\Delta\boldsymbol{\varepsilon}_n$ over each fiber $\boldsymbol{V_i}$ of the shell element (Figure 4.1) is then computed.

$$\overline{\Delta\boldsymbol{\varepsilon}}_n = \frac{1}{2}\int_{-1}^{+1} \Delta\boldsymbol{\varepsilon}_n d\zeta \tag{4.14}$$

The normal strain increment $\Delta\varepsilon_{zi}$ is then calculated at each node i by projecting the mean strain tensor increment $\overline{\Delta\boldsymbol{\varepsilon}}_n$ onto the fiber direction $\boldsymbol{V_i}$ of each node i using

$$\begin{aligned} \Delta\varepsilon_{zi} &= \boldsymbol{V_i}^T\, \overline{\Delta\boldsymbol{\varepsilon}}_n\, \boldsymbol{V_i} \qquad \text{for} \quad i = 1,4 \\ &= < V_{ix},\, V_{iy},\, V_{iz} > \begin{bmatrix} \overline{\Delta\varepsilon}_x & \overline{\Delta\varepsilon}_{xy} & \overline{\Delta\varepsilon}_{xz} \\ \overline{\Delta\varepsilon}_{xy} & \overline{\Delta\varepsilon}_y & \overline{\Delta\varepsilon}_{yz} \\ \overline{\Delta\varepsilon}_{xz} & \overline{\Delta\varepsilon}_{yz} & 0 \end{bmatrix} \begin{Bmatrix} V_{ix} \\ V_{iy} \\ V_{iz} \end{Bmatrix} \end{aligned} \tag{4.15}$$

Finally the normal strain increment $\Delta\varepsilon_z(\xi,\eta)$ over the element surface, is determined by interpolation using the in-plane shape functions $N_i(\xi,\eta)$ of the quadrilateral shell element

$$\Delta\varepsilon_z(\xi,\eta) = \sum_{i=1}^{4} N_i(\xi,\eta)\ \Delta\varepsilon_{zi} \tag{4.16}$$

At each time step n, after calculating the five components of plastic strain increment $\Delta\boldsymbol{\varepsilon}_n$ and the stress increment $\Delta\boldsymbol{\sigma}_n$using Eq.(4.9) and Eq.(4.12), then Eq.(4.15) is used to estimate the normal strain increments as a post-processing operation to obtain the new thickness change. Finally the thickness change is calculated as follows

$$h = h_0\ \exp(\varepsilon_z) \qquad \text{with} \qquad \varepsilon_z = \varepsilon_{zn} + \Delta\varepsilon_z \tag{4.17}$$

with h_0 the initial thickness of the shell.

4.1.5 Multimaterial model

The previous section described the plastic flow modeling for a classical single material, namely the $S500$ steel and the $S420$ one. In a typical U-shape laser beam welding as the one shown in

Figure 4.2, there exist physically three material zones having different properties. Namely the melting zone (MZ), then the heat affected zone (HAZ) and the base material (BM).
In an industrial context of modeling, generally the HAZ size is so small compared to the MZ, that it cannot be meshed nor represented even by a single element when using the "*Shell Coarse Model*". The reason is that the time step calculation will decrease dramatically resulting in a very long simulation time, which is not convenient in an industrial context.

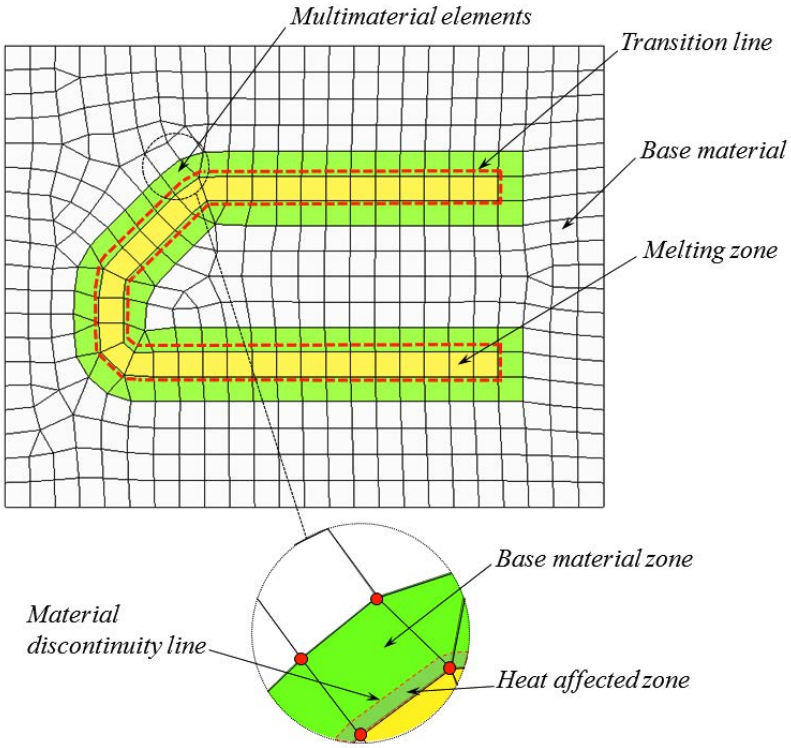

Figure 4.2: Multimaterial element including both base material and heat affected zone material.

Therefore, it appears clearly there is a need for a multimaterial shell element having a size compatible with a "*Shell Coarse Model*" but this element should contain both HAZ and BM as shown in Figure 4.2. As a consequence, the multimaterial shell element will include a material discontinuity line as shown in Figure 4.2. This kind of discontinuity is know as a "*weak discontinuity*", because only the gradients (stresses and strains) are discontinuous but the velocity field remain continuous.

4.1.5.1 Weak discontinuity treatment

As stated before the displacement field is continuous within the shell multimaterial element, but the plastic strains and stresses are discontinuous because of the material discontinuity caused by the presence of HAZ and base material within the same element as depicted in Figure 4.3.
Several mathematical functions have been proposed in the literature to take into account the weak discontinuity. Among all available functions, the "*signed distance function*" is a suitable choice for our problem.
As shown in Figure 4.3, the distance d from any point located by its position vector $\boldsymbol{x}$ to the discontinuity line Γ between HAZ and BM can be defined by,

$$d = \|\boldsymbol{x} - \boldsymbol{x}_\Gamma\| \tag{4.18}$$

where $\boldsymbol{x}_\Gamma$ is the normal projection of $\boldsymbol{x}$ on Γ (Figure 4.3). The signed distance function $\psi(\boldsymbol{x})$ can then be defined as,

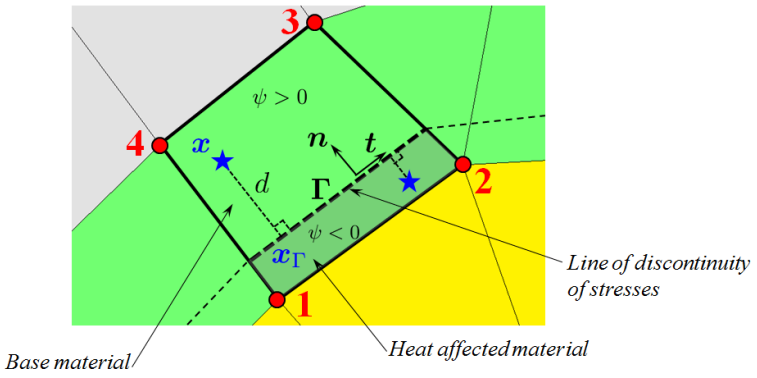

Figure 4.3: Weak discontinuity of material : *signed distance function* ψ.

$$\psi(\boldsymbol{x}) = min\|\boldsymbol{x} - \boldsymbol{x}_\Gamma\| \; sign\left(\boldsymbol{n} \cdot (\boldsymbol{x} - \boldsymbol{x}_\Gamma)\right) \tag{4.19}$$

where $\boldsymbol{n}$ is the unit normal vector to the discontinuity line Γ.

4.1.5.2 Element partitioning and numerical integration

For numerical evaluation of the internal force vector given by Eq.(3.41) described in the previous chapter, the Gauss quadrature rule is used within the mid-surface of the multimaterial element. As it is known, for non-polynomial integrands, Gauss quadrature rule may result in substantial error when using a small number of Gauss points.

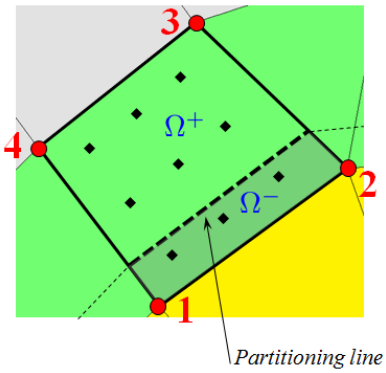

(a) Standard Gauss quadrature rule

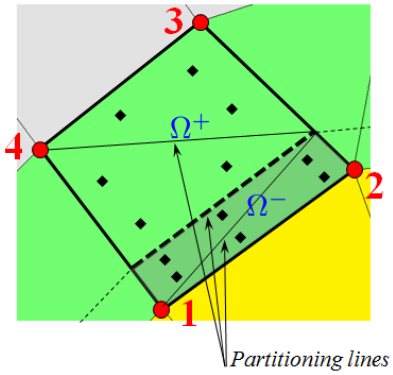

(b) Partitioning into triangles: Hammer quadrature rule

Figure 4.4: Two methods for partitioning the multimaterial element.

The introduction within the same multimaterial element, of two materials having different mechanical properties, i.e. a HAZ where stresses are high with a BM where stresses are low, transforms the stress field into highly nonlinear field. As a result, it is important to define accurately the necessary integration points needed for the integration within the multimaterial element.
There exist mainly two techniques for partitioning the multimaterial element in order to perform the integration of the residual force vector accurately. The first method is depicted in Figure

4.4(a), it consists in creating enough standard integration points using the Gauss quadrature rule, then by using the signed distance function ψ Eq.(4.19), it becomes easy to distinguish between Gauss points relying to BM (zone Ω^+) and those relying to the HAZ (zone Ω^-).
The second method is depicted in Figure 4.4(b), it consists in subdividing the multimaterial element at both sides of the discontinuity line into sub-triangles whose edges are adapted to discontinuity sides. Then the Hammer quadrature rule is applied withing each sub-triangle to perform the integration over all the element.
In the present investigation, the first technique is retained mainly because it is easy to use and it is well adapted for a HAZ of a quadrilateral shape area in our case. In this case the calculation of the internal force vector in Eq.(3.41), reads

$$\boldsymbol{f}^e_{int} = \int_\Omega \left(\mathbb{B}^T_{mb} \boldsymbol{\sigma}_s + \mathbb{B}^T_s \boldsymbol{\tau} \right) J_o \frac{h}{2} \, d\Omega \tag{4.20}$$

where $\Omega = \Omega^+ + \Omega^-$ is the element volume in the parametric configuration. The integral of Eq.(4.20) is performed using the signed distance function ψ using the two domain parts, one covering the BM with domain Ω^+ and the other covering the HAZ with domain Ω^-.

$$\boldsymbol{f}^e_{int} = \int_{\Omega^+} \left(\mathbb{B}^T_{mb} \boldsymbol{\sigma}_s + \mathbb{B}^T_s \boldsymbol{\tau} \right) J_o \frac{h}{2} \, d\Omega^+ + \int_{\Omega^-} \left(\mathbb{B}^T_{mb} \boldsymbol{\sigma}_s + \mathbb{B}^T_s \boldsymbol{\tau} \right) J_o \frac{h}{2} \, d\Omega^- \tag{4.21}$$

By using Gauss quadrature rule, we obtain

$$\begin{aligned} \boldsymbol{f}^e_{int} \;=\; J_o \frac{h}{2} \sum_{k=1}^{np_L} \omega_k \Bigg(& \sum_{i=1}^{np^+_G} \sum_{j=1}^{np^+_G} \omega^+_i \, \omega^+_j \, \left(\mathbb{B}^T_{mb}(\xi^+_i, \eta^+_j, \zeta_k) \, \boldsymbol{\sigma}^+_s + \mathbb{B}^T_s(\xi^+_i, \eta^+_j, \zeta_k) \, \boldsymbol{\tau}^+ \right) + \\ & \sum_{i=1}^{np^-_G} \sum_{j=1}^{np^-_G} \omega^+_i \, \omega^-_j \, \left(\mathbb{B}^T_{mb}(\xi^-_i, \eta^-_j, \zeta_k) \, \boldsymbol{\sigma}^-_s + \mathbb{B}^T_s(\xi^-_i, \eta^-_j, \zeta_k) \, \boldsymbol{\tau}^- \right) \Bigg) \end{aligned} \tag{4.22}$$

where np^+_G and np^-_G are the numbers of Gauss integration points in the plane of the element from zone Ω^+ and Ω^- respectively. np_L is the number of Lobatto integration points through the shell thickness. It has to be noticed, that during our investigation, several numbers of Gauss integration points have been tested to evaluate their influence upon the final results.
The size of the HAZ is $0.4mm$ in the reference solid refined model and the same size is kept in the multimaterial shell element which is shown in Figure 4.5. The ratio between BM and HAZ is adjusted by changing the isoparametric weight of the Gauss integration points, accordingly.

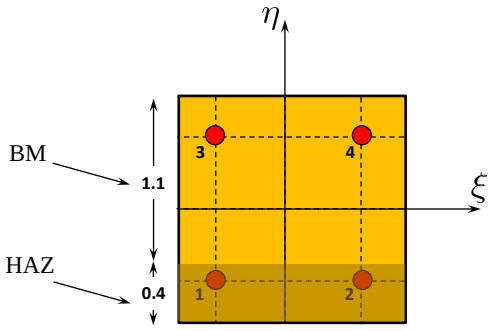

Figure 4.5: Size of BM and HAZ in the multimaterial shell element.

4.2 Examples of validation of the multimaterial element

In order to evaluate the effectiveness of the multimaterial element, several numerical applications are treated and their results are compared with the one obtained using a "*Refined Solid Model*" within Ls-dyna. All the numerical applications are closely related to the welding where the developed material model is used to represent the BM and HAZ in the multimaterial element of the shell models.

4.2.1 Elasto-plastic bending of a clamped plate

This application consists in the elato-plastic bending of a clamped plate under transverse loading. The geometrical dimensions of the plate are shown in Figure 4.6 where a Length of $9mm$, a width $1mm$ and a thickness of $2.5mm$. The material data are $E = 2.1 \times 10^5 MPa$, $\nu = 0.3$ and $\rho = 7.85 \times 10^{-3} g/mm^3$. The plate is loaded with a maximal force of $150N$ applied on the right side (Figure 4.6).
Two solid models using refine mesh (sizes of $0.2mm$ and $0.05mm$) are taken as reference to compare the results quality of the multimaterial "*Coarse Shell Model*". Two shell models with the same mesh size $1.5mm$ are prepared and the difference in both shell models is to use

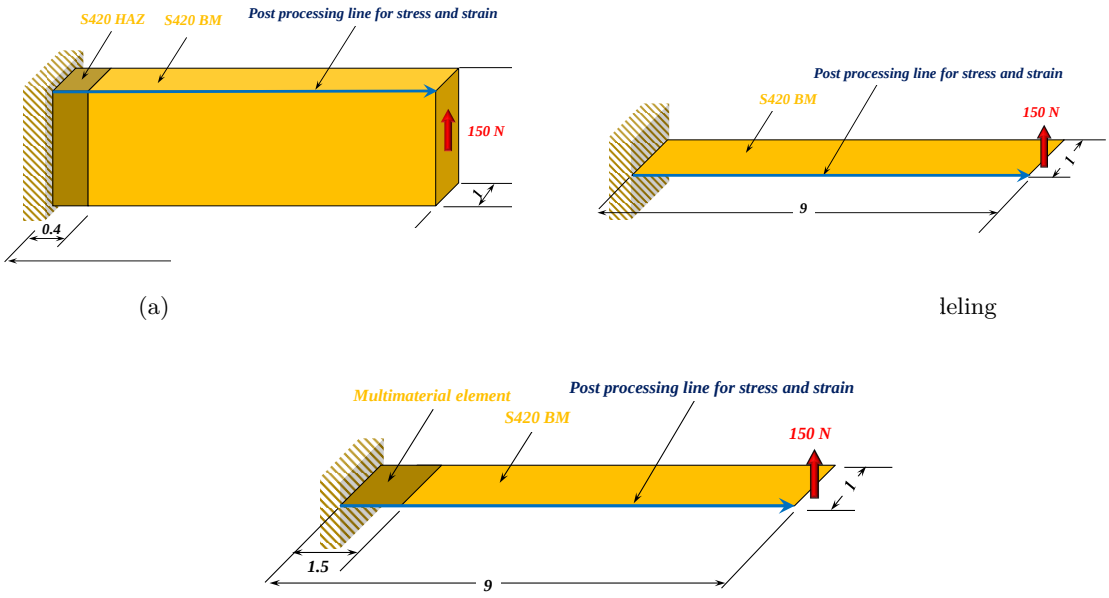

(a)

leling

(c) Shell modeling using a multimaterial element

Figure 4.6: Elasto-plastic bending of a clamped plate: Geometry and boundary conditions

In the "*Coarse Shell Model*" the first element on the clamp is a multimaterial element, having two materials (HAZ and BM) provided by user element and user material subroutines. von-Mises contour plots of solid and shell models are shown in Figure 4.7 and their graphical results are illustrated in Figure 4.8.
It can be seen that "*Refine Solid Model*" predicts a maximum von-Mises stress value $847MPa$ near the clamp and the standard "*Coarse Shell Model*" using just base material can predict $694MPa$ with -18% error. When using the multimaterial "*Coarse Shell Model*" it captures a maximum von-Mises stress value $852MPa$ with $+0.5\%$ error which is very close to the reference

solution and the curve behavior shows the similar trend as the reference one.

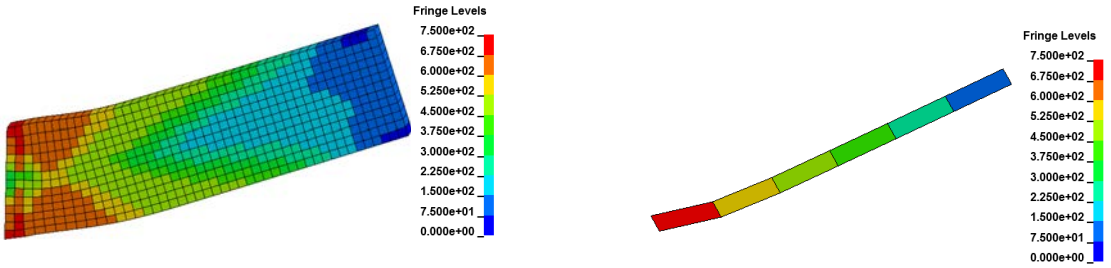

(a) Refine Solid model 0.2mm (b) Coarse Shell Model 1.5mm (multimaterial model)

Figure 4.7: von-Mises stress distribution.

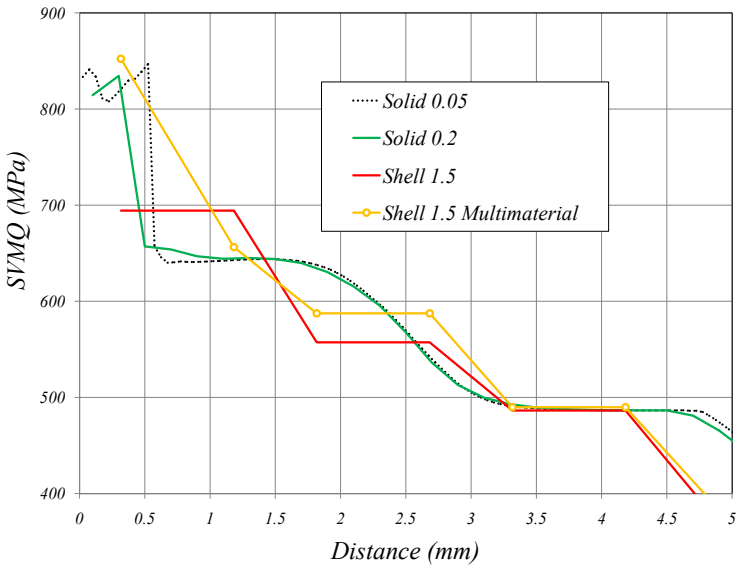

Figure 4.8: von-Mises stress comparison between Refine Solid and Coarse Shell models.

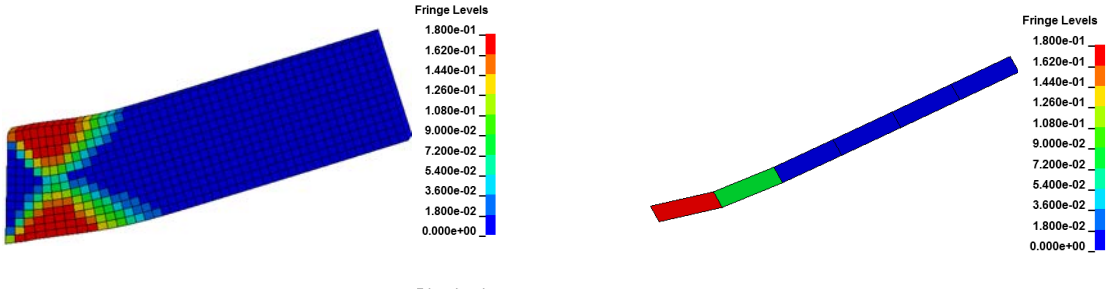

(a) Refine Solid model 0.2mm (b) Coarse Shell Model 1.5mm (multimaterial model)

Figure 4.9: Effective plastic strain distribution.

Effective plastic strain distribution of solid and shell models are depicted in the Figure 4.9 and graphical comparison is shown in Figure 4.10. The maximum effective plastic strain 20.9% is

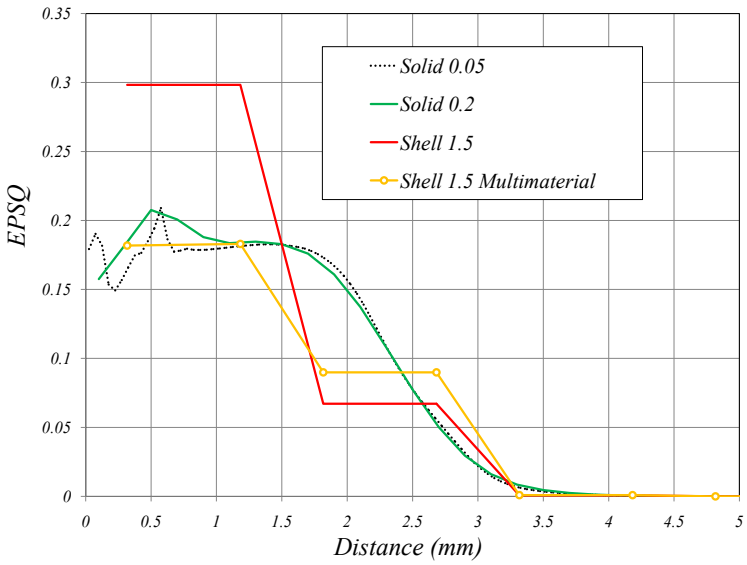

Figure 4.10: Effective plastic strain comparison between Refine Solid and Coarse Shell models.

observed at the interface of HAZ and BM in the solid models whereas the shell model with BM overestimates effective plastic strain with 29.8% error. The "*Coarse Shell Model*" using a multimaterial element can predict the effective plastic strain 18.3% which is closer to the reference solution.
In conclusion the "*Coarse Shell Model*" using the multimaterial element allows a good estimation of stress and plastic strain compared to a reference solution obtained using the "*Solid Refine Model*".

4.2.2 Two-plate elasto-plastic bending

This application concerns the elasto-plastic bending of a two-plate clamped structure with material properties $E = 2.1 \times 10^5 MPa$, $\nu = 0.3$ and $\rho = 7.85 \times 10^{-3} g/mm^3$. This application is very close to the laser welding WSII benchmark and hence the dimensions of different material zones are taken equal to those of the WSII model.
The geometrical dimensions of the structure are shown in Figure 4.11, where Length is $9.72mm$, width is $1mm$ and thickness of the $S420$ and $S500$ plate layers are $2.5mm$ and $1.8mm$ respectively. The structure is subjected to maximal deflection of $5mm$ in both opposite directions so the maxim

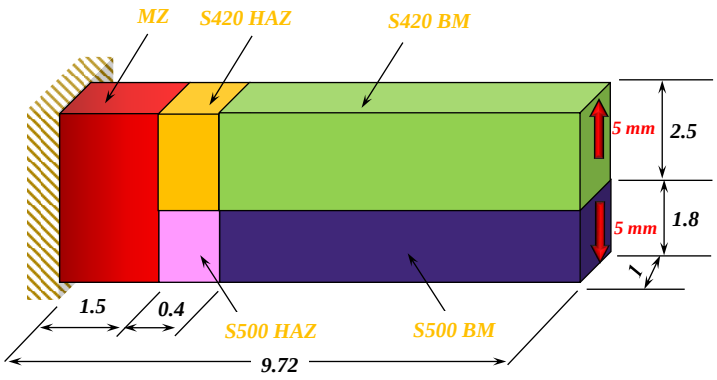

Figure 4.11: Elasto-plastic bending of a clamped plate: Geometry and boundary conditions

Two solid models are prepared with mesh sizes $0.2mm$ and $0.05mm$ and taken as reference to compare the results with the shell models. The element size $1.5mm$ is used to prepare two shell models. The difference in both shell models is the use of multimaterial element in one case as

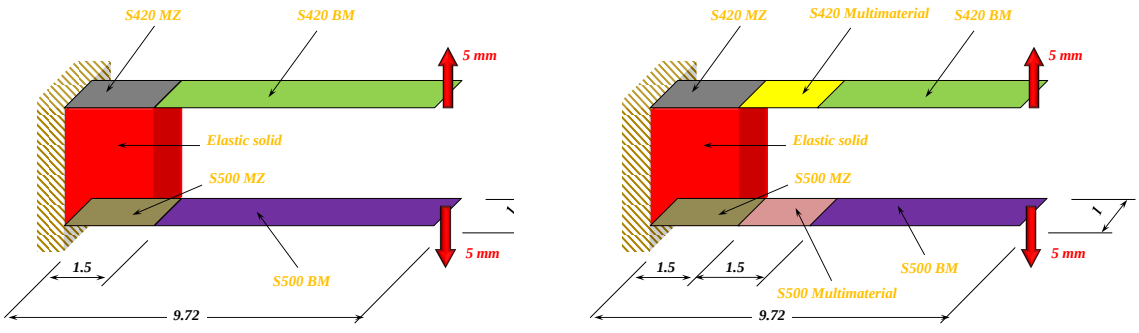

(a) Standard Coarse shell modeling (b) multimaterial Coarse shell modeling

Figure 4.12: "*Coarse Shell Modeling*" of a Two-plate bending

Both materials HAZ and BM are used to model the multimaterial zone and here two multimaterial elements are used because of $S420$ and $S500$ materials in two-plate structure. The size of BM and HAZ in the multimaterial element is kept same as in the solid models and supplied by the User material subroutine.

The von-Mises stress and effective plastic strain results of "*Solid Refine Model*" and "*Coarse Shell Models*" are compared and post-processing is carried out corresponding to the black arrows shown in each contour plot.

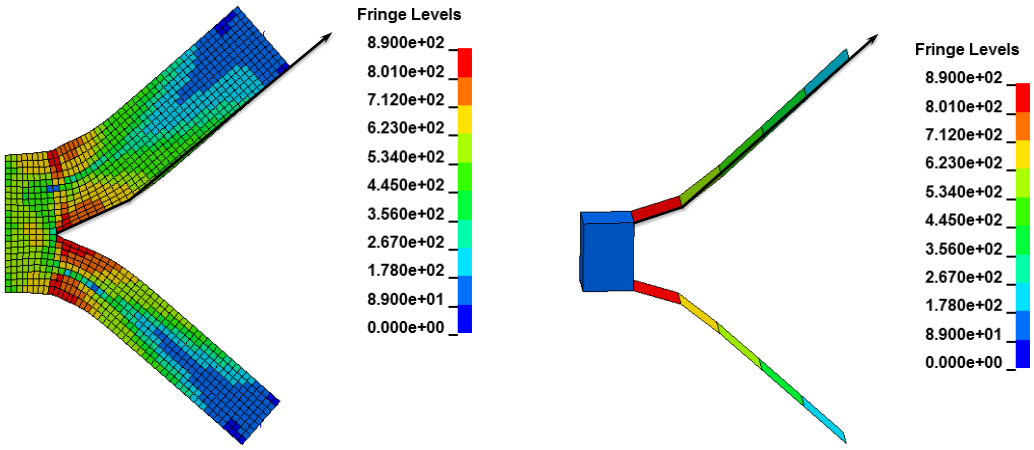

(a) Refine Solid model 0.2mm

(b) Coarse Shell Model 1.5mm (multimaterial model)

Figure 4.13: von-Mises stress distribution (side of S420).

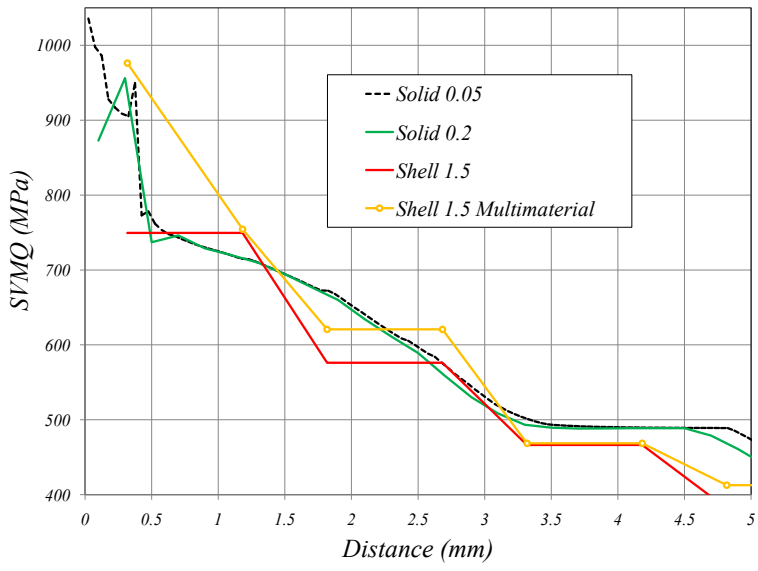

Figure 4.14: von-Mises stress comparison between Refine Solid and Coarse Shell models (side of $S420$).

At first, von-Mises stress is compared on the side of $S420$ and contour plots of von-Mises stress of solid and shell models are depicted in Figure 4.13. The graphical representation of the von-Mises stress comparison is illustrated in the Figure 4.14. The maximum von-Mises stress found in the HAZ of solid 0.05 and solid 0.2 models are $1040MPa$ and $956MPa$, respectively. The standard "*Coarse Shell Models*" predicts a maximum von-Mises stress value $749MPa$ with an

error of -22% compared to the "*Solid Refine Model*". von-Mises stress is improved by using our multimaterial element in the "*Coarse Shell Models*" and the maximum value of von-Mises stress approaches to $976MPa$ with just $+2\%$ error in comparison with the "*Solid Refine Model*".

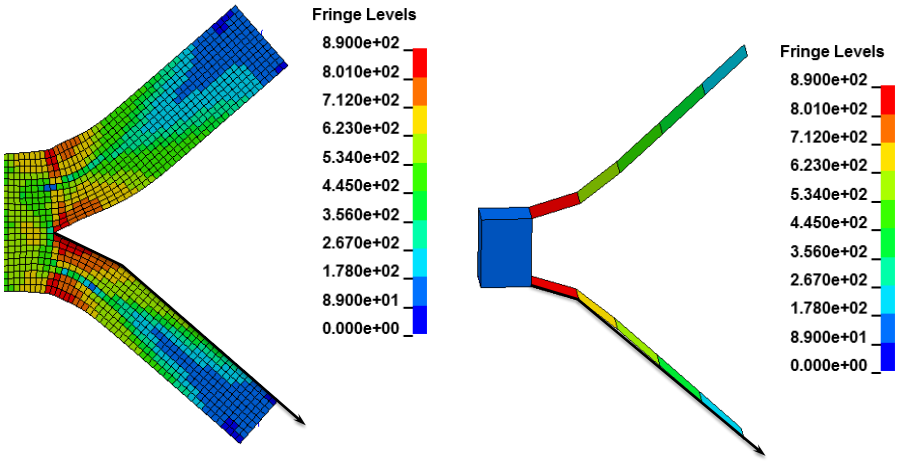

(a) Refine Solid model $0.2mm$ (b) Coarse Shell Model $1.5mm$ (multimaterial model)

Figure 4.15: von-Mises stress comparison between Refine Solid and Coarse Shell models (side of $S500$).

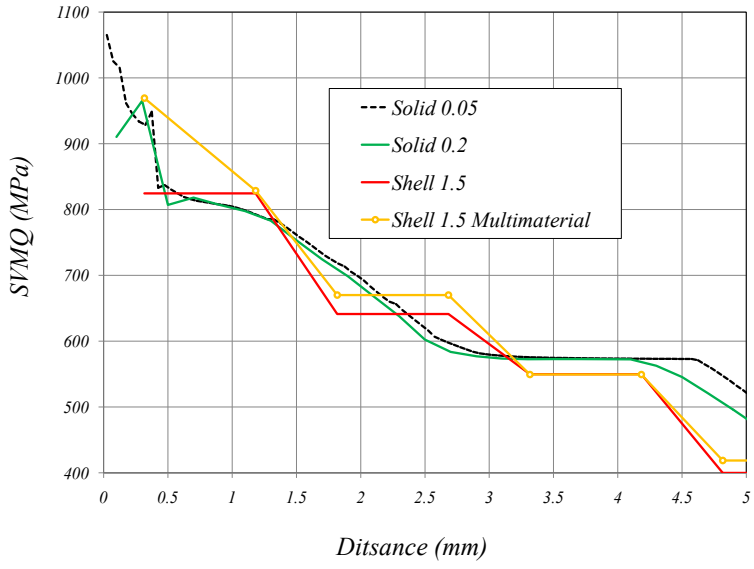

Figure 4.16: von-Mises stress comparison between Refine Solid and Coarse Shell models (side of S500).

von-Mises stress distributions obtained by using "*Solid Refine Model*" and "*Coarse Shell Model*" are shown in Figure 4.15. and black arrows on the side of $S500$ describes the post processing lines. "*Solid Refine Model*" predicts maximum von-Mises stress values in the HAZ of $S500$ are $1070MPa$ and $965MPa$, as mentioned in the von-Mises stress graph in Figure 4.16. The maximum value of von-Mises stress in the shell model with just BM is $824MPa$ with error

percentage -14.6% by taking solid $0.2mm$ as reference. The shell model featuring multimaterial element shows improvement in the von-Mises stress and the maximum value found is $969MPa$ with just $+0.4\%$ error.

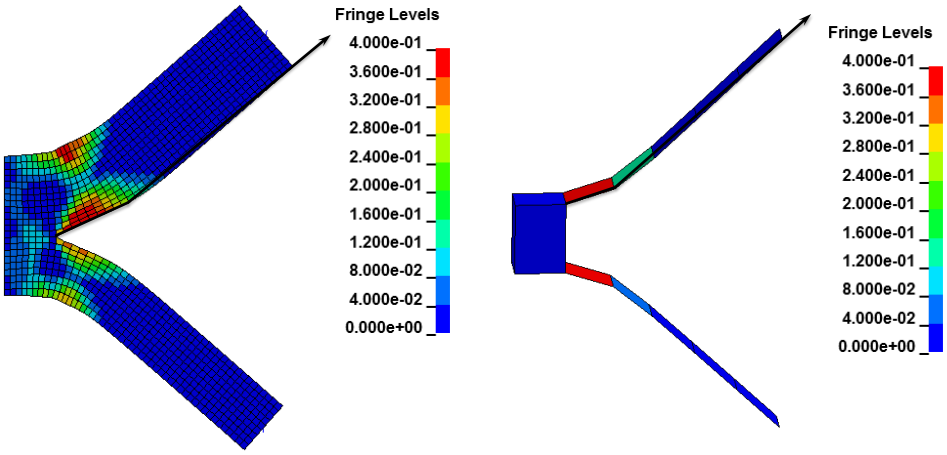

(a) Refine Solid model $0.2mm$ (b) Coarse Shell Model $1.5mm$ (multimaterial model)

Figure 4.17: Effective plastic strain comparison between Refine Solid and Coarse Shell models (S420).

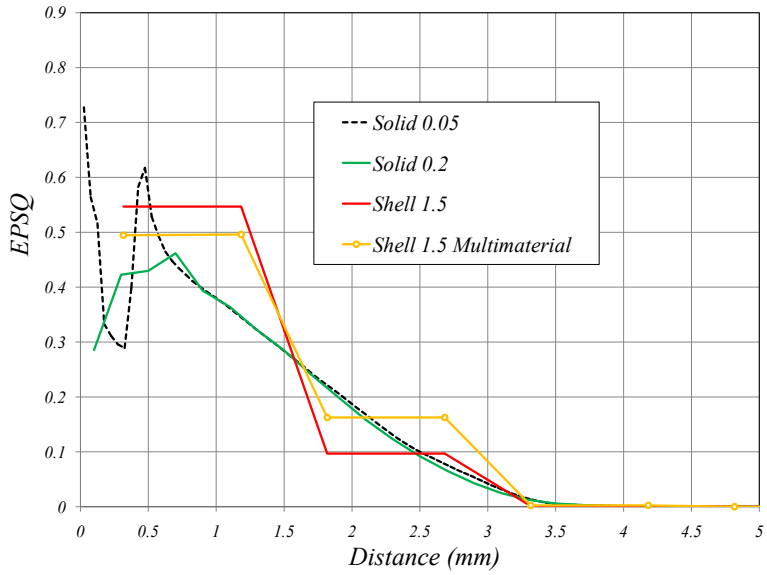

Figure 4.18: Effective plastic strain comparison between Refine Solid and Coarse Shell models (S420).

Effective plastic strain comparison is carried out on the side of $S420$ plate where distributions are depicted in the Figure 4.17. The maximum values of effective plastic strain found in "*Solid Refine Models*" are 72.8% and 46.2%. The concentration of plastic strain is observed at the interface of HAZ and BM in the solid 0.2 model. The "*Coarse Shell Model*" with only BM shows 54.7% effective plastic strain with 18.39% error compared to solid 0.2 model. More plastic strain

is due to the missing of HAZ that is stronger material compared to BM. The effective plastic strain value goes closer to the solid 0.2 by using multimaterial element in the shell model. The maximum value of plastic strain in the "*Coarse Shell Model*" using multimaterial element found is 49.4% with 6.9% error only.

4.2.3 WSII laser welded benchmark

The third numerical application concerns the WSII laser welded industrial benchmark. Arcan setup is used to apply a peeling load to the WSII weld by applying a constant velocity to the structure. The specimen is clamped from the bottom side ($S500$) by means of screws and subjected to velocity of $0.2m/s$ from the top side ($S420$) as illustrated in Figure 4.19.

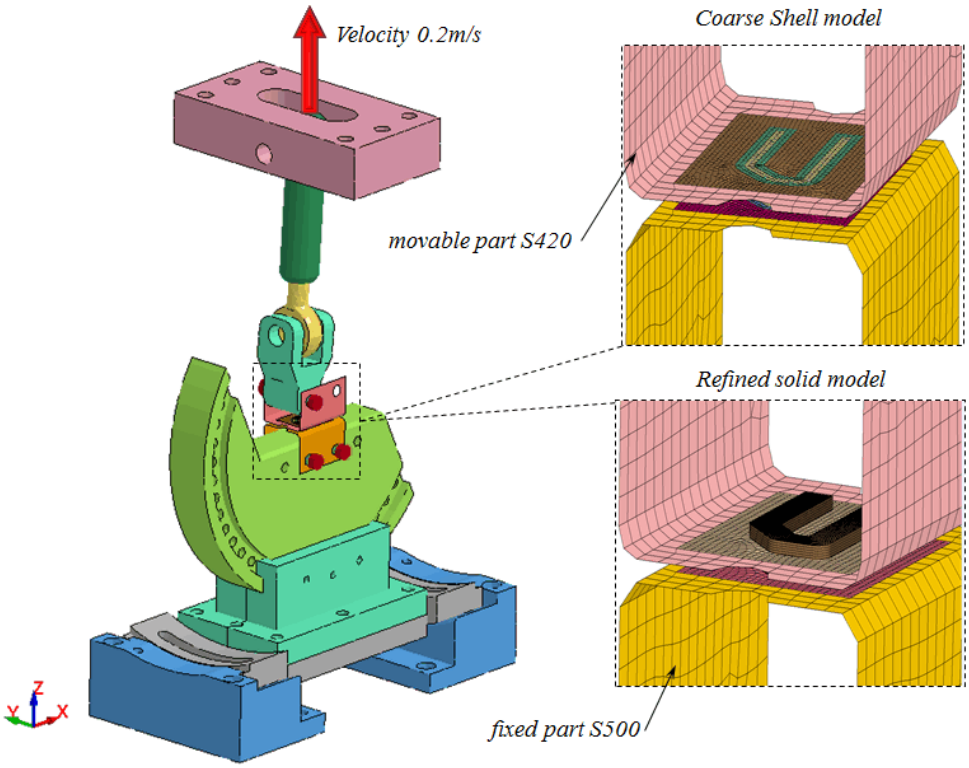

Figure 4.19: WSII laser welded benchmark subjected to peeling load.

The "*Solid Refine Model*" is composed of solid elements with mesh size $0.2mm$ featuring all the three zones necessary to model the welding line as shown in the Figure 4.20(a). The "*Coarse Shell Model*" is based on a mesh of $1.5mm$ element size, it uses two variants : baseline version and multimaterial version as shown in Figure 4.20(b).
The geometrical dimensions, material curves of different zones and difference between solid refine and shell coarse models have been discussed in the chapter 2 in detail.
For the comparison of the results between solid refine and shell coarse models, section cuts are taken from the corner of the welding line as illustrated in the Figure 4.21. Post processing for von-Mises stress and effective plastic strain is carried out at $13kN$.
At first, von-Mises stress is compared between solid refine and shell coarse models on the side of S420. von-Mises contour plots of both models are shown in Figure 4.22 where arrows corresponds to the postprocessing lines. Graphical representation of von-Mises stress comparison is depicted in the Figure 4.23. The maximum value of von-Mises stress predited by solid refine model

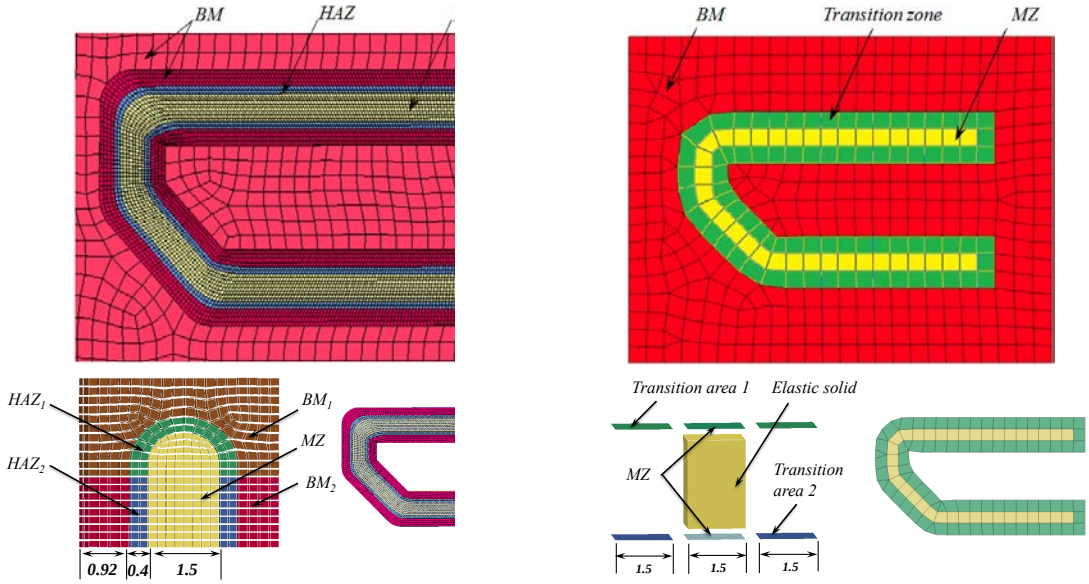

(a) "*Solid Refine Model*" (b) "*Coarse Shell Model*"

Figure 4.20: Description of the WSII Laser welding line : Refine solid vs. Coarse shell

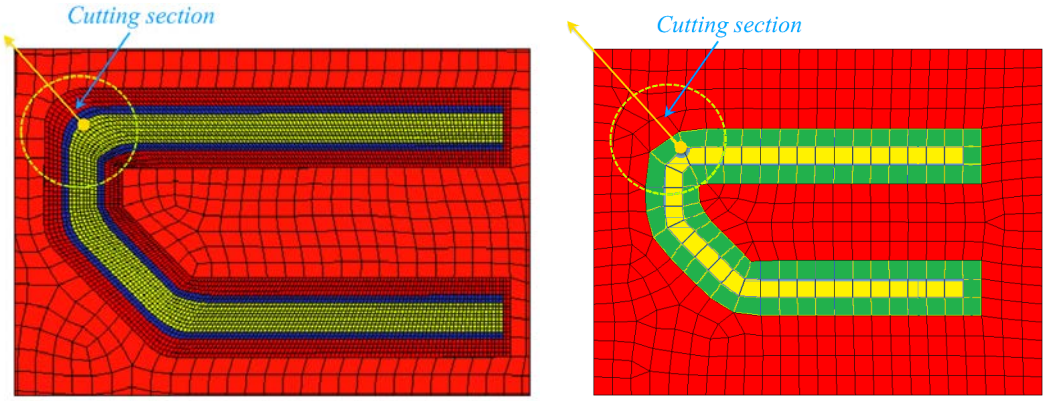

(a) "*Solid Refine Model*" (b) "*Coarse Shell Model*"

Figure 4.21: Section cutting line in the reference solid refine and shell coarse models.

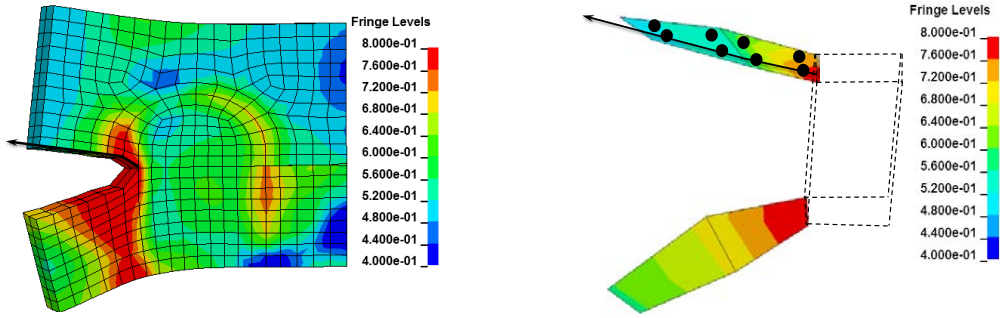

(a) "*Solid Refine Model*" (b) "*Coarse Shell Model*"

Figure 4.22: von-Mises stress comparison on the side of S420 plate.

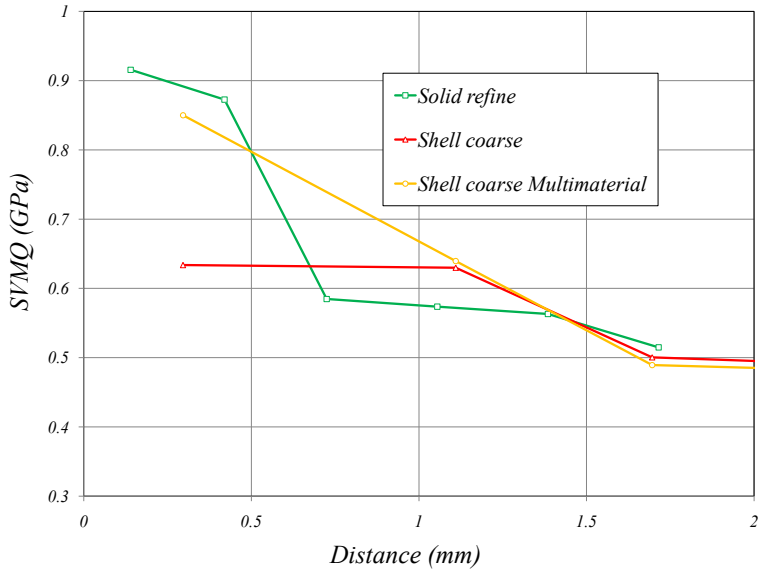

Figure 4.23: von-Mises stress comparison on the side of S420 plate.

is $915MPa$ and it is concentrated in the HAZ. The shell coarse model with only BM can capture maximum von-Mises stress $633MPa$ with error percentage -31% after comparing with the reference solid refine model. This error percentage is reduced to -7% in the shell coarse multimaterial model by capturing maximum von-Mises stress values $850MPa$.

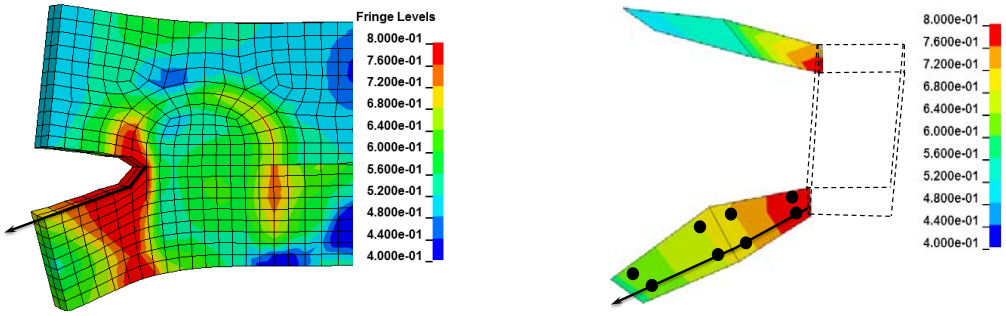

(a) "*Solid Refine Model*" (b) "*Coarse Shell Model*"

Figure 4.24: von-Mises stress comparison on the side of S500 plate.

von-Mises stress comparison between solid refine and shell coarse models on the side of S500 is carried. Figure shows the von-Mises stress contour plots of both models and graphical comparison is depicted in the Figure. The maximum concentration of von-Mises stress is found in the HAZ in the solid refine model with $1043MPa$. The shell coarse model with just BM predicted maximum von-Mises stress value $805MPa$ that results in -22.8% error. The maximum von-Mises stress captured by shell coarse multimaterial model is $962MPa$ that reduces the error percentage to -7.7%.

It can be noted that stress concentration is more on the side of S500 compare to the S420 because S500 is stronger material than S420.

Effective plastic strain is compared between solid refine and shell coarse models on the side of S420. Contour plots of plastic strain are depicted in Figure 4.26 where arrows shows the postprocessing lines. Plastic strain is concentrated in the HAZ in the solid refine model as

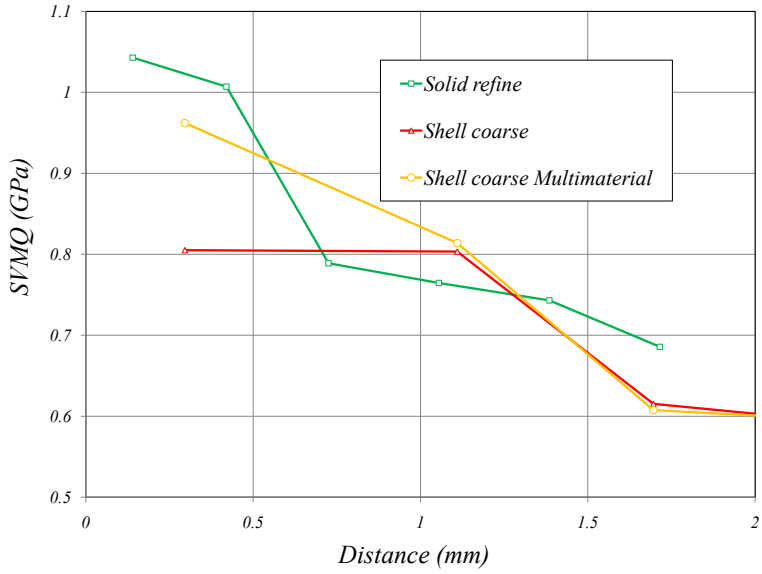

Figure 4.25: von-Mises stress comparison on the side of S500 plate.

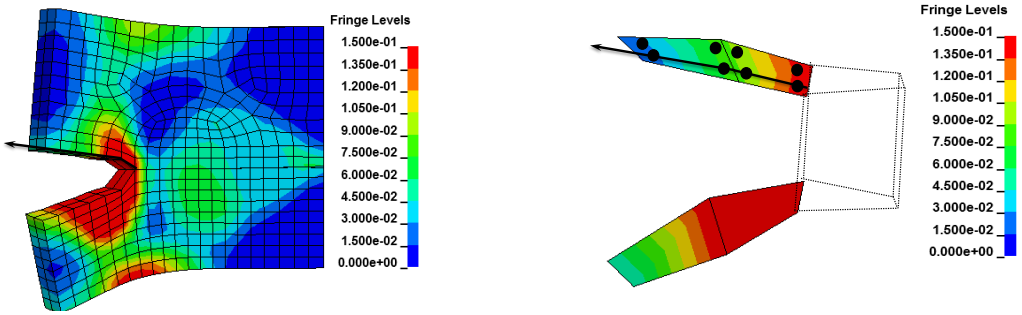

(a) "*Solid Refine Model*" (b) "*Coarse Shell Model*"

Figure 4.26: Effective plastic strain comparison on the side of S420 plate.

shown in the Figure 4.27 and maximum value that can be captured by solid refine model is 30.8%. Effective plastic strain comparison is carried out in the graph and it is presented in the Figure. The shell model with only BM can predict 16.2% plastic strain value and it improves to 19.1% by using multimaterial elements in the shell coarse model.

4.3 Damage model for laser welding failure prediction

In order to predict failure of the laser welded joints, it is necessary to define a damage model. In the literature there exist several ductile damage models applied to metallic materials. Among all damage models, Neukamm et al. [102–104] proposed a phenomenological damage model based on stress state dependent failure strain formulation. This damage model has been adopted and implemented into a User Material subroutine within Ls-dyna software. In the following sections, detailed formulation of this damage model will be given.

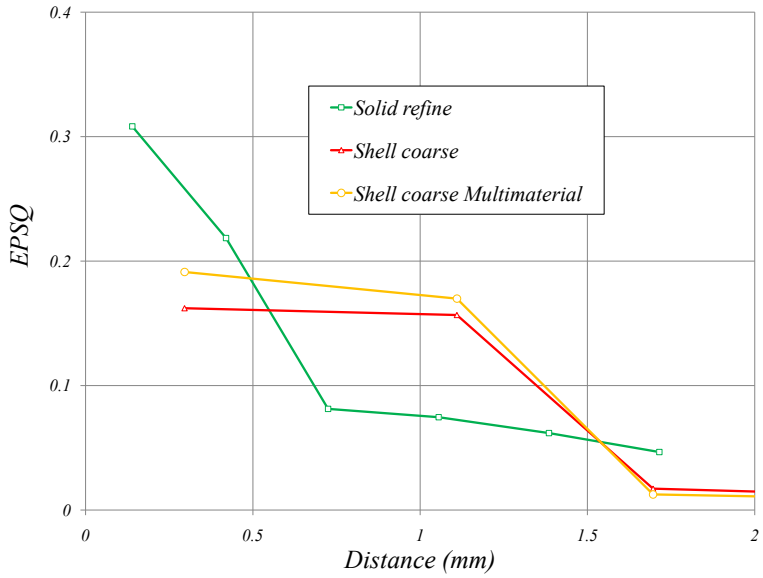

Figure 4.27: Effective plastic strain comparison on the side of S420 plate.

4.3.1 Stress state characterization

For an isotropic material the stress tensor $\boldsymbol{\sigma}$ has six components but it is convenient to represent it in the Haigh-Westergaard space $\{\sigma_1, \sigma_2, \sigma_3\}$. Figure 4.28) shows mainly the form for a combination of principal stress components and does not consider the orientation of the principal stress compo

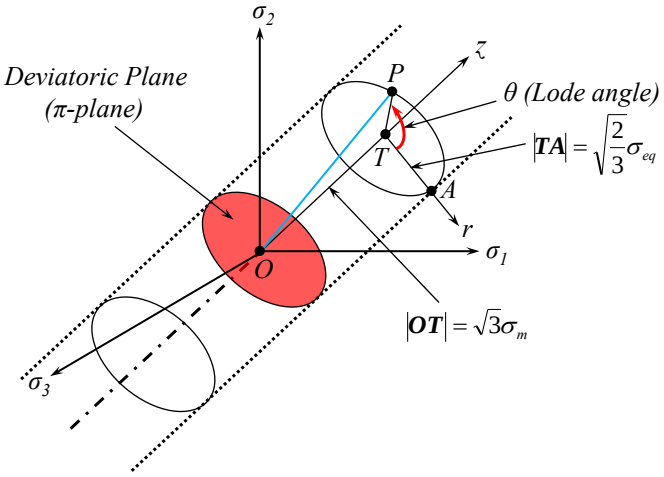

Figure 4.28: Representation of the stress state in Haigh-Westergaard space $\{\sigma_1, \sigma_2, \sigma_3\}$ and cylindrical coordinates $\{r, \theta, z\}$.

The stress vector $\boldsymbol{OP}$ can be represented in cylindrical coordinate system $\{r, \theta, z\}$, as shown in Figure 4.28. The $z - axis$ is called hydrostatic axis, where all the principal stresses are equal. The plane, which is passing through the origin O and is perpendicular to $z - axis$, is called the $\pi - plane$.
In cylindrical coordinate system the stress vector $\boldsymbol{OP}$ can be decomposed into two components as hydrostatic part $\boldsymbol{OT}$ and deviatoric part $\boldsymbol{TP}$. The vector $\boldsymbol{OT}$ is perpendicular to octahedral

plane and the vector $\boldsymbol{TP}$ is in the octahedral plane. The magnitude $|\boldsymbol{OT}|$ is linearly related to hydrostatic stress.

$$|\boldsymbol{OT}| = \sqrt{3}\,\sigma_m \tag{4.23}$$

where σ_m is the mean stress, defined by

$$\sigma_m = \frac{1}{3}\left(\sigma_1 + \sigma_2 + \sigma_3\right) \tag{4.24}$$

The magnitude $|\boldsymbol{TA}|$ is linearly related to the equivalent stress

$$|\boldsymbol{TA}| = \sqrt{\frac{2}{3}}\,\sigma_{eq} \tag{4.25}$$

where σ_{eq} is the von-Mises equivalent stress, defined as

$$\sigma_{eq} = \sqrt{\frac{(\sigma_1 - \sigma_2)^2 + (\sigma_1 - \sigma_3)^2 + (\sigma_2 - \sigma_3)^2}{2}} \tag{4.26}$$

The third coordinate θ differentiates the stress state between tension, shear and compression. In literature the Lode angle influence is usually used as Lode dependence and for the Lode angle there are different definitions.
The stress state definition in cylindrical coordinate system can be also expressed with stress invariants uniquely. Above discussed three cylindrical dimensions σ_m, σ_{eq} and θ are described through

$$\sigma_m = \frac{1}{3}\,J_1 \tag{4.27}$$

$$\sigma_{eq} = \sqrt{3\,J_2} \tag{4.28}$$

$$\theta = \frac{1}{3}\arccos\left(\frac{3\sqrt{3}}{2}\frac{J_3}{J_2^{3/2}}\right) \tag{4.29}$$

where J_1 is the first stress invariant, J_2 and J_3 are second and third deviatoric stress invariants. It should be noted that with three stress invariants the stress state at a material point can be defined uniquely. It is convenient to work with the dimensionless pressure η, which is defined as the ratio of hydrostatic pressure to equivalent stress

$$\eta = \frac{\sigma_m}{\sigma_{eq}} \tag{4.30}$$

The parameter η, often referred to "*stress triaxiality*", has been used extensively in the ductile damage investigations [141–146]. A detailed derivation is presented in [148].
Hereinafter the normalized third deviatoric invariant will be called Lode angle parameter, as it is a function of θ. The range of the Lode angle parameter is $0 \leq \xi \leq 1$, since the range of the Lode angle θ is $0 \leq \theta \leq \pi/3$. It can be showed that $\xi = 1$ corresponds to axisymmetric tension, $\xi = 0$ corresponds to generalized shear condition (plane strain). The lower limit value $\xi = -1$ corresponds to axisymmetric compression or equi-biaxial tension [149]. Two dimensionless stress state parameters η and ξ define the direction of the stress vector in Haigh-Westergaard space.

4.3.2 Damage rate evolution

The damage variable was firstly introduced for creep by Kachanov [150] and by Rabotnov [151] in the framework of continuum damage mechanics. In many industrial applications the damage indicator has been modeled as a scalar value and good results have been obtained [152–154]. By assuming the damage as isotropic, it can be defined as

$$D = 1 - \frac{A_{eff}}{A_o} \tag{4.31}$$

where D is isotropic scalar damage, A_o is reference cross sectional area and A_{eff} represents the effective resisting area after subtracting the micro cracks and micro voids from reference area. The very first idea of an incremental accumulation through strain path history has been suggested by Johnson and Cook [145] who adopted a simple accumulation of a failure variable as a function of the fracture curve and of the plastic strain. This can be considered as an evolution equation which depends on the current deformation pattern.

As reported by Bai et al. [157], Xue [158], Tasan [159] and Weck et al. [160, 161], the damage variable is supposed to be given, for proportional loading, by

$$D = \left(\frac{\varepsilon_p}{\varepsilon_f(\eta)} \right)^c \tag{4.32}$$

where D is damage variable, ε_p is the accumulated plastic strain and $\varepsilon_f(\eta)$ is the fracture strain as a function of the current triaxiality η and c is a damage exponent which defines the nonlinearity level of the damage accumulation. This damage is known as GISSMO damage model.
Differentiating Eq.(4.32) with respect to time and assuming constant triaxiality, one gets corresponding damage rate

$$\dot{D} = c \left(\frac{\varepsilon_p}{\varepsilon_f(\eta)} \right)^{c-1} \frac{\dot{\varepsilon}_p}{\varepsilon_f(\eta)} \tag{4.33}$$

By using the definition of Eq.(4.32) and rearranging the terms, we have the general expression

$$\dot{D} = \frac{c}{\varepsilon_f(\eta)} \, D^{\frac{c-1}{c}} \, \dot{\varepsilon}_p \tag{4.34}$$

Eq.(4.34) does not explicitly depend on the current plastic strain, therefore there is no direct dependence of the current plastic strain from the damage evolution. This property is important when dealing with load reversal and cyclic loadings. This damage model evolution is, from a numerical point of view, an incremental accumulation of a failure variable. As a matter of fact, Eq.(4.34) acts as an evolution equation which drives the damage rate for general non-proportional loadings.

4.3.3 Critical stress-damage coupling

Here an additional variable F, which refers to "*instability measure*", is introduced in the same manner as damage variable D. Being a function of critical strain $\varepsilon_{crit}(\eta)$, the derivation for proportional loading reads,

$$H = \left(\frac{\varepsilon_p}{\varepsilon_{crit}(\eta)} \right)^c \tag{4.35}$$

Differentiating with respect to time and assuming constant triaxiality, one gets

$$\dot{H} = \frac{c}{\varepsilon_{crit}(\eta)} H^{\frac{c-1}{c}} \dot{\varepsilon}_p \tag{4.36}$$

where the critical strain curve, $\varepsilon_{crit}(\eta)$, is also a function of the triaxiality and is intended to act as a trigger for coupling damage and stress under proportional loading.
It is assumed that damage affects the stress tensor through

$$\boldsymbol{\sigma} = \left(1 - \widetilde{D}\right) \widetilde{\boldsymbol{\sigma}} \tag{4.37}$$

where $\widetilde{\boldsymbol{\sigma}}$ is undamaged stress tensor and $\widetilde{D}$ can be defined by

$$\widetilde{D} = \begin{cases} 0 & if \quad H < 1 \\ \left(\dfrac{D - D_{crit}}{1 - D_{crit}}\right)^m & if \quad H = 1 \end{cases} \tag{4.38}$$

D_{crit} is the damage when F reaches value 1.0 and is necessary to guarantee a smooth transition from non-coupled to coupled responses. Furthermore, m is a fading exponent intended to better depict the evolution of $\widetilde{D}$ whenever the indicator F has reached the critical value of 1.0.
By substituting Eq.(4.38) into Eq.(4.37), one gets

$$\boldsymbol{\sigma} = \widetilde{\boldsymbol{\sigma}} \left(1 - \left(\frac{D - D_{crit}}{1 - D_{crit}}\right)^m\right) \tag{4.39}$$

From a practical point of view, the critical damage D_{crit} and the fading exponent m provide more flexibility when describing post-critical material behavior using relatively large elements. Contrary to D,which should be interpreted as a general failure variable and accumulates whenever a plastic strain increment is present, $\widetilde{D}$ represents the damaging that takes place when strain localization arises. Therefore, this variable only starts to have some value when F reaches unity.

4.3.4 Mathematical fracture strain criterion

Fracture strain criteria of BM and HAZ of $S420$ and $S500$ materials are obtained after performing a number of tensile and shear tests and these tests are performed by Faurecia Automotive Seating. Tensile tests are performed with several geometries e.g. tensile test with hole, tensile test with notches and erichsen test to get normal fracture parameters.
Similarly, shear fracture parameters are identified by performing shear tests on several geometries e.g. tensile test with grooves at 45^o and 90^o, pure shear test and erichsen test. After performing tensile and shear tests, Faurecia Automotive Seating has used MATFEM material failure model to identify the normal and shear fracture parameters.

On the basis of these parameters, fracture strain surface ε_{crit} of each material was obtained in $3D$ space. Fracture strain surface of HAZ $S500$ is shown in Figure 4.29 where driving force for failure ε_p is plotted as a function of η and ξ.

4.3.5 Numerical implementation of damage model

The incremental damage model given by Eq.(4.34) and Eq.(4.36) has been implemented within Ls-dyna commercial software.
The numerical implementation using an Explicit dynamics scheme is straightforward, because the model is uncoupled from plasticity. Therefore all computations related to failure are performed after convergence of the return mapping plasticity algorithm.

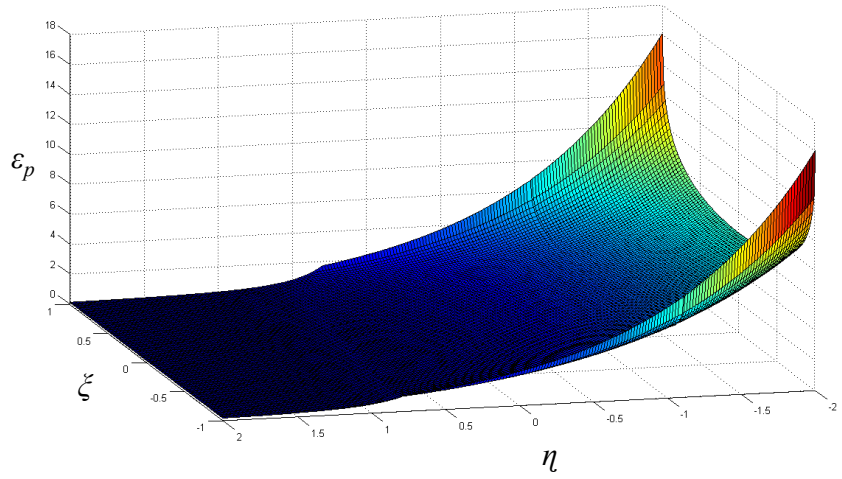

Figure 4.29: Fracture strain surface ε_{crit} of HAZ S500 in 3D space.

At each time step n during Explicit dynamics integration scheme, knowing the damage value D^n and instability function F^n, then Eq.(4.34) and Eq.(4.36) can be rewritten as

$$D^{n+1} = D^n + \Delta D \qquad \text{with} \quad \Delta D = \frac{c}{\varepsilon_f(\eta)} \left(D^n\right)^{\frac{c-1}{c}} \Delta\varepsilon_p \tag{4.40}$$

$$H^{n+1} = H^n + \Delta H \qquad \text{with} \quad \Delta H = \frac{c}{\varepsilon_{crit}(\eta)} \left(H^n\right)^{\frac{c-1}{c}} \Delta\varepsilon_p \tag{4.41}$$

The equations Eq.(4.40) and Eq.(4.41) are calculated for every integration point using the current values of triaxiality η, and increment of plastic strain $\Delta\varepsilon_p$.

When damage reaches $D = 1$, failure is assumed to have taken place and the integration point is no longer able to handle any external loadings.

4.3.6 Validation of stress based damage model

In order to validate the implemented stress based damage model, the "*Coarse Shell Model*" has been used for the modeling of the academic clamped plate application. Results of damage obtained for the implemented version is compared to the available standard `MAT-EROSION` card of Ls-dyna using the same finite element mesh.
Clamped plate benchmark is depicted in Figure 4.30 with the boundary conditions and geometrical dimensions. Length of the beam is $9mm$, width is $1mm$ and thickness is $1.8mm$.
The plate is clamped from the left and force with a magnitude of $F = 150N$ is applied on the right side. HAZ $S500$ material is used with $E = 210GPa$, $\nu = 0.3$ and $\rho = 7850kg/m^3$. Fully integrated shell elements are used in Ls-dyna using $1.5mm$ mesh size.
Damage distribution of clamped plate is shown in Figure 4.31. We can observe that the obtained damage distribution of the implemented model is similar the damage obtained using `MAT-EROSION` Ls-dyna damage card.
The damage evolution function of time is shown in Figure 4.32. It can be seen that damage evolution curve of the implemented stress based damage model is very close to the evolution

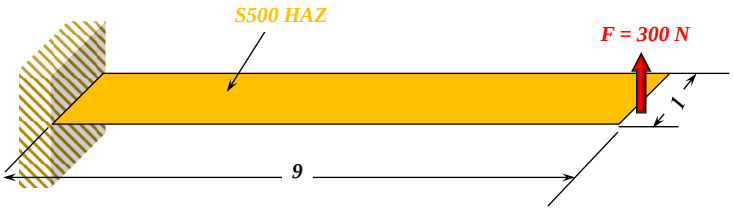

Figure 4.30: Clamped beam under the application of transverse load.

of damage of Ls-dyna using `MAT-EROSION` card. Damage maximum values are also very similar with a small error less than 2% error.

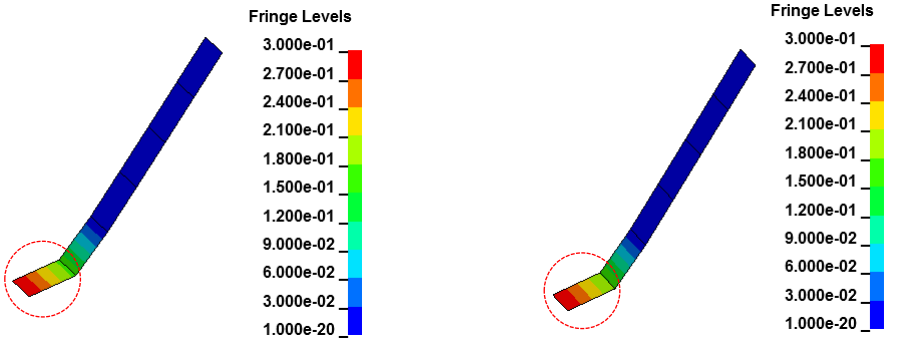

(a) Implemented stress based damage model (b) Ls-dyna GISSMO damage model

Figure 4.31: Damage distribution comparison: Implemented damage vs. Ls-dyna damage models.

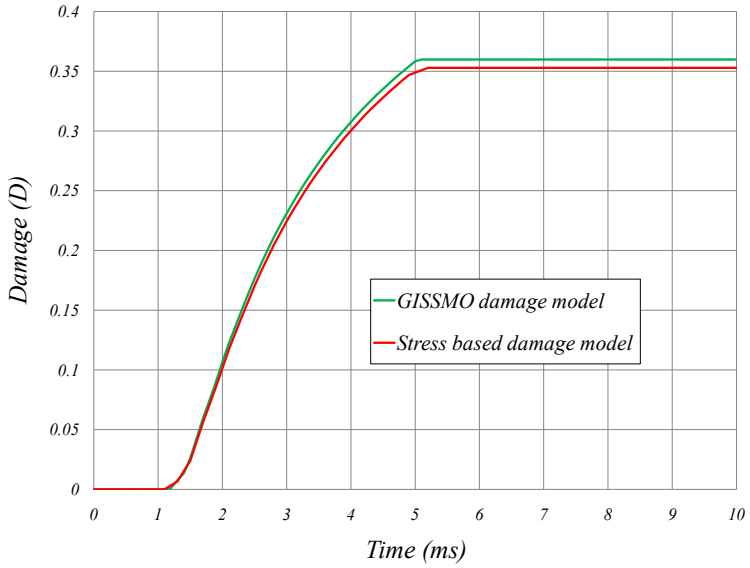

Figure 4.32: Damage evolution comparison: Implemented damage vs. Ls-dyna damage models.

Therefore it is concluded that the implemented stress based damage model using User Material subroutine works accurately and it can be used for the modeling of industrial applications such as the WSII benchmark.

4.4 Transverse stress approximation in the shell modeling

The GISSMO damage presented in the previous section depends on the plastic strain, but also on the $3D$ stress state. Unfortunately, in shell formulation the plane stress $\sigma_z = 0$ assumption is always taken. Therefore, it appears that the implemented GISSMO damage model could not give good results with the absence of transverse stress component σ_z through the shell thickness.

In order to show, the weakness of the GISSMO damage model with standard plane stress shells, the WSII application has been treated using the developed multimaterial shell model using the "*Coarse Shell Model*". For comparison purpose the WSII application has been treated using "*Solid Refine Model*" and its solution is considered as a reference solution.

It is prior knowledge thanks to experiments that failure occurred in the HAZ on the side of $S500$ material and the same phenomenon was observed in the "*Solid Refined Model*". Loading history curve of 1^{st} deleted element in HAZ of $S500$ is plotted against failure surface of the same material and it is shown in Figure 4.33. Lode parameter is fixed to 1 in the failure surface.

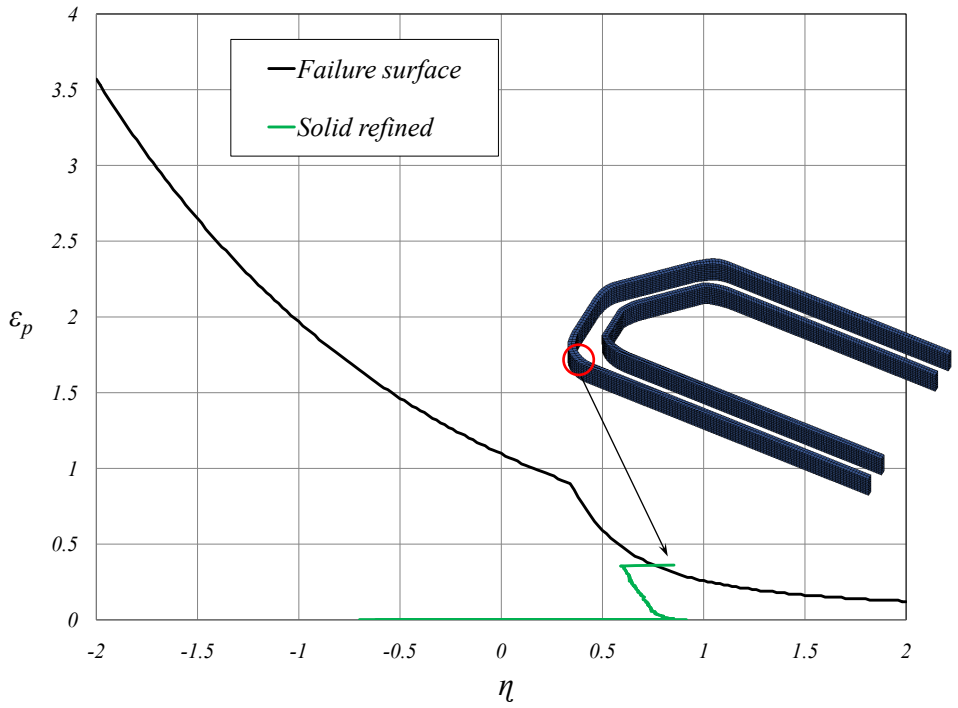

Figure 4.33: Loading history curve of 1st deleted element in the HAZ S500 in solid refined model.

Loading history contains the history of effective plastic strain as a function of stress triaxiality. The element is deleted when the value of damage parameter D reaches 1.0 and loading history curve is close enough to the failure surface. The corresponding load was $8.8kN$ when 1^{st} element was deleted in the "*Solid Refined Model*".
When using the "*Shell Coarse Model*", multimaterial elements are used in the transition area. It was shown in the previous section that von-Mises stress improved by using multimaterial elements. Even with the improved von-Mises stress, "*Coarse Shell Model*" did not show failure. Loading history curve of the corner element in the transition area of shell coarse model is shown in the Figure 4.34. It can be seen that loading history curve is very far from the failure surface. The reason why "*Shell Coarse Model*" does not show failure is because the damage parameter D

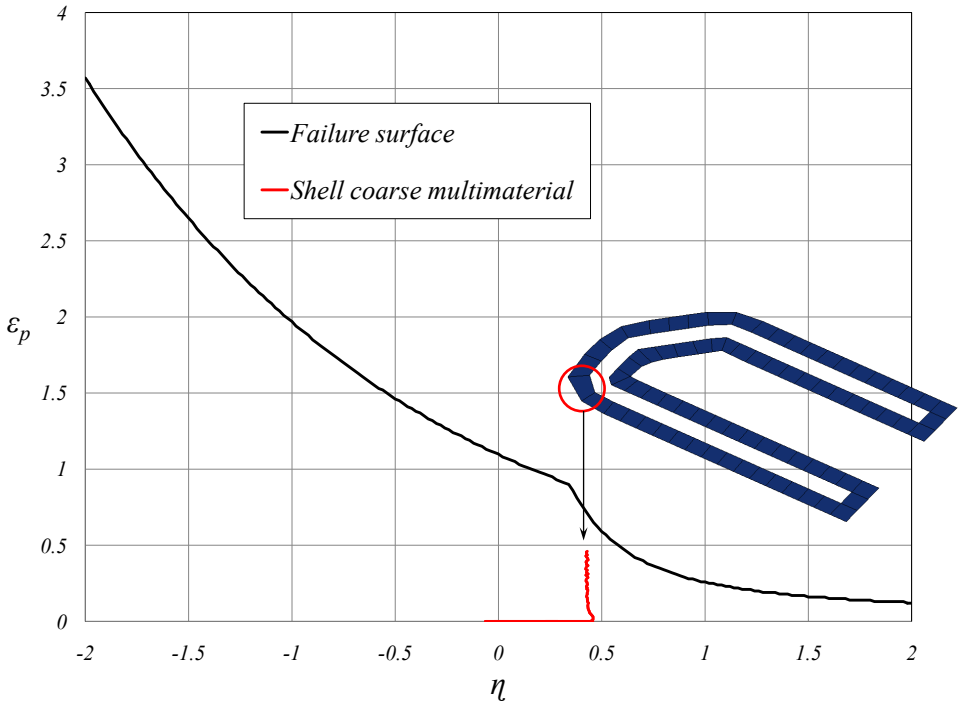

Figure 4.34: Loading history curve of the element in the transition area S500 in shell coarse model.

does not reach unity. The damage evolution with respect to time curves of solid refined and shell coarse models are compared in the Figure 4.35. The value of damage parameter D in the case of "*Solid Refined Model*" reaches unity at $33ms$ simulation time where as damage parameter does not exceed than $D = 0.17$ in the "*Coarse Shell Model*" even at $80ms$ that is termination time of simulation.

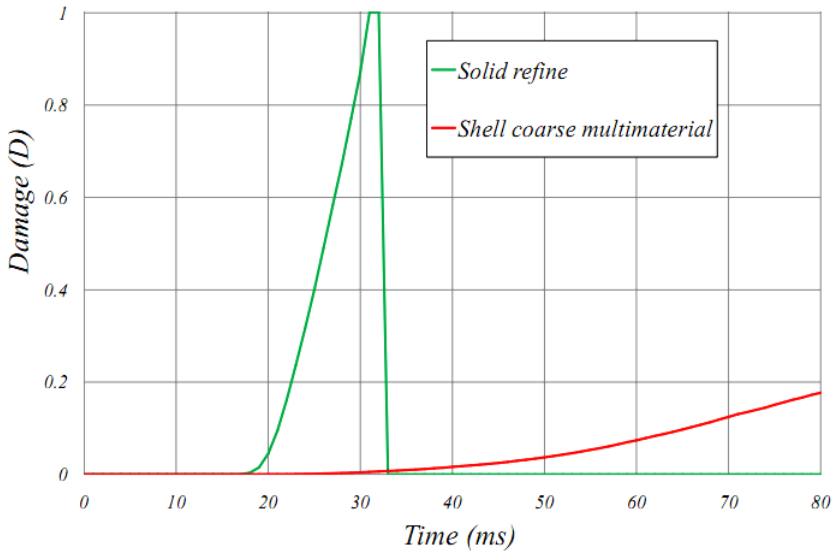

Figure 4.35: Damage evolution comparison : solid refine vs. shell coarse multimaterial model.

In order to enhance the capability of the multimaterial shell element, one needs an approximation of the transverse stress in a post-processing phase after calculation plastic strain and stress state.

This will improve the stress triaxiality and therefore may improve the damage value.

To do so, transverse stress component σ_z has to be estimated in the multimaterial shell model where normally plane stress condition is assumed in the shell formulation allowing $\sigma_z = 0$. To estimate the transverse stress component σ_z, we use the plastic incompressibility assumption in a post-processing phase. The plastic incompressibility condition allows the calculation of the transverse plastic strain ε^p_{33} as follows,

$$\varepsilon^p_{33} = -\varepsilon^p_{11} - \varepsilon^p_{22} \tag{4.42}$$

In Eq.(4.42) the principal plastic strains ε^p_{11} and ε^p_{22} have been calculated using the shell formulation based on plane stress condition. Once the transverse plastic strain ε^p_{33} is calculated, then it becomes possible to estimate a new correction to the equivalent plastic strain ε^p_{eq} by taking new thickness plastic strain ε^p_{33} into account

$$\varepsilon^p_{eq} = \sqrt{\frac{2}{3}\left[(\varepsilon^p_{11})^2 + (\varepsilon^p_{22})^2 + (\varepsilon^p_{33})^2 + 2\left((\varepsilon^p_{12})^2 + (\varepsilon^p_{23})^2 + (\varepsilon^p_{31})^2\right)\right]} \tag{4.43}$$

Once the new equivalent plastic strain ε^p_{eq} has been obtained, then the corresponding new equivalent stress is estimated using the hardening curve f of the HAZ $S500$ material. This can be written as,

$$\sigma_{eq} = f(\varepsilon^p_{eq}) \tag{4.44}$$

The transverse stress component σ_{33} is then calculated by solving the equivalent stress equation

$$(\sigma_{11} - \sigma_{22})^2 + (\sigma_{22} - \sigma_{33})^2 + (\sigma_{33} - \sigma_{11})^2 + 6(\sigma^2_{12} + \sigma^2_{23} + \sigma^2_{31}) - 2\sigma^2_{eq} = 0 \tag{4.45}$$

and therefore the transverse stress can be approximated by,

$$\sigma_{33} = \frac{1}{2}\left(\sigma_{11} + \sigma_{22} \pm \sqrt{4\sigma^2_{eq} - 3(\sigma^2_{11} + \sigma^2_{22} - 2\sigma_{11}\sigma_{22}) - 12(\sigma^2_{12} + \sigma^2_{23} + \sigma^2_{31})}\right) \tag{4.46}$$

This new estimated transverse stress component σ_{33} is used to make $3D$ stress state in the shell and it also cause to enhance the stress triaxiality, to be used for damage model, as

$$\sigma^u_m = \frac{1}{3}\left(\sigma_{11} + \sigma_{22} + \sigma_{33}\right) \tag{4.47}$$

where σ^u_m is new mean stress that take transverse stress σ_{33} into account during calculation.

$$\eta^u = \frac{\sigma^u_m}{\sigma_{eq}} \tag{4.48}$$

where η^u is improved stress triaxiality used in the stress based damage model.

4.5 WSII failure modeling using implemented damage model

Numerical application of the implemented stress based damage model on WSII using the "*Shell Coarse Model*" is carried out in this section and results are compared with WSII using the "*Solid Refined Model*". Improved stress triaxiality $\eta^u = \sigma^u_m/\sigma_{eq}$ is our damage model where the mean stress $\sigma^u_m = (\sigma_{11} + \sigma_{22} + \sigma_{33})/3$ is calculated by adding transverse stress component.

Loading history curve of corner element in S500 transition area of "*Coarse Shell Model*" is plotted against failure surface and is illustrated in Figure 4.36. Loading history curve of element

5796 is close enough to the failure surface that element is deleted and rupture happens. This is the result of improved stress triaxiality used in the implemented stress based damage model.

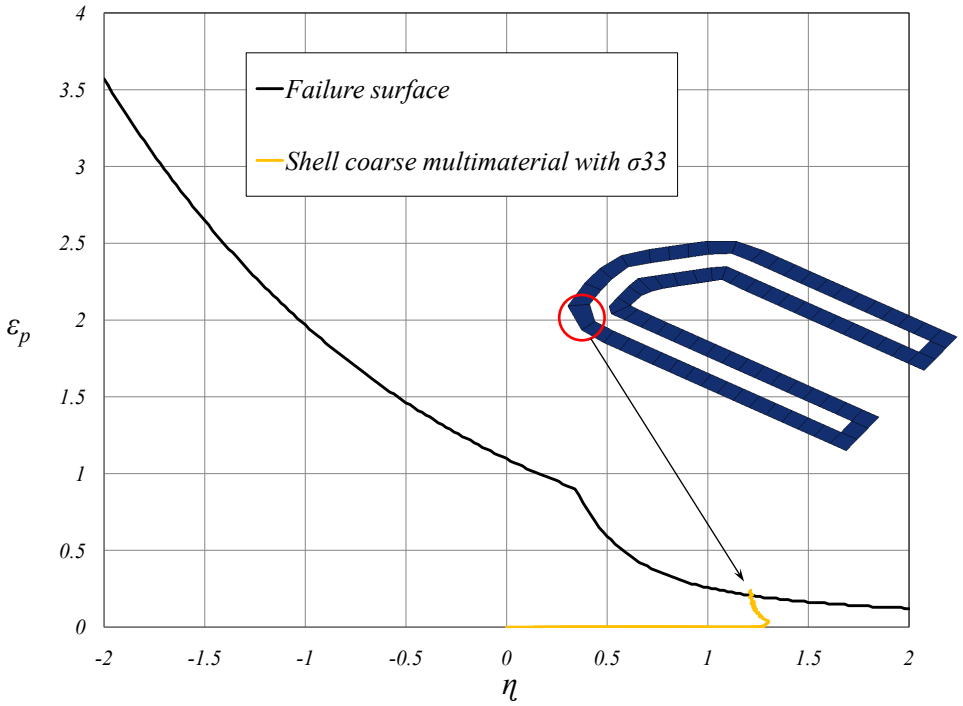

Figure 4.36: Loading history curve of the element in the transition area S500 in shell coarse model including transverse stress enhancement.

Damage evolution curve comparison between "*Solid Refine Model*" and "*Coarse Shell Model*" is presented in Figure 4.37. In "*Coarse Shell Model*" with σ_{33}, damage value approaches to $D = 1$ at $55ms$ simulation time and at a load of $13.5kN$. Damage evolution appears slower in "*Coarse Shell Model*" compared to "*Solid Refined Model*", this is probably due to the different element size between the two models. The use of regularization technique should improve the solution.

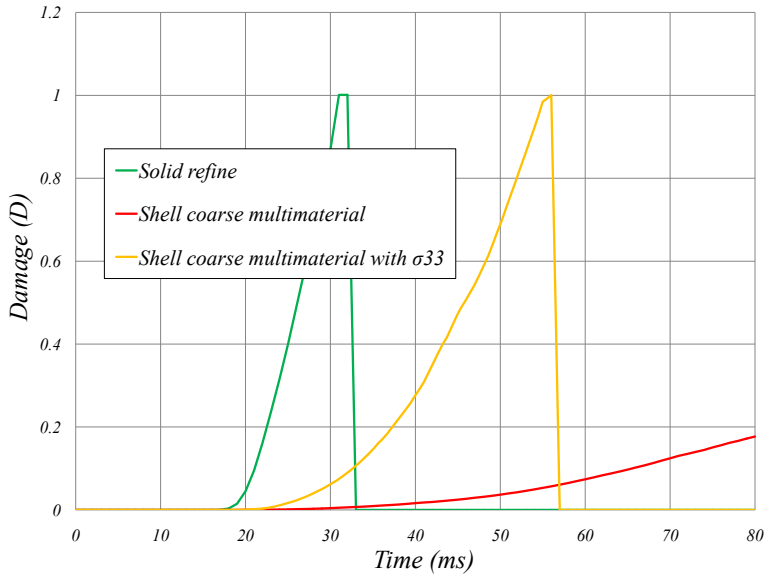

Figure 4.37: Damage evolution comparison between solid refine, shell coarse multimaterial and shell coarse multimaterial model after adding transverse stress component.

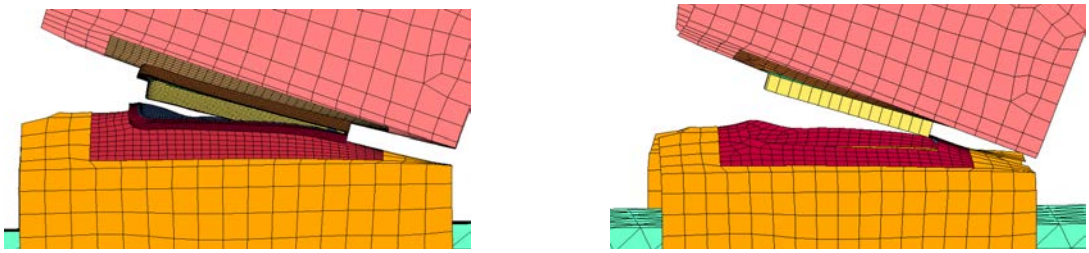

(a) Solid refine model.

(b) Shell coarse model.

Figure 4.38: Weld line rupture in the solid refine and shell coarse models.

4.6 Concluding remarks

In the present chapter, a standard elasto-plastic model based on an isotropic hardening law was implemented as a user material subroutine within Ls-dyna software to be able to model the nonlinear behavior of the pair of assembled metallic sheets. A multimaterial element including the HAZ and the BM within the same element has been proposed with its implementation. A weak discontinuity of material inside the element has been also presented and numerical integration of the internal force vector has been discussed. In order to predict failure, the generalized incremental stress dependent damage model has been developed and implemented within the commercial software Ls-dyna.

In order to improve the efficiency of failure prediction using the previous damage model, it has been shown that triaxiality stress state plays an important role. To this end, the plastic incompressibility condition has been imposed within the multimaterial element to be able to estimate the transverse stress component in a post-processing phase. Numerical validation of the shell coarse model, has been shown through the solution of the WSII benchmark, where failure has been predict accurately compared to the solid refine model.

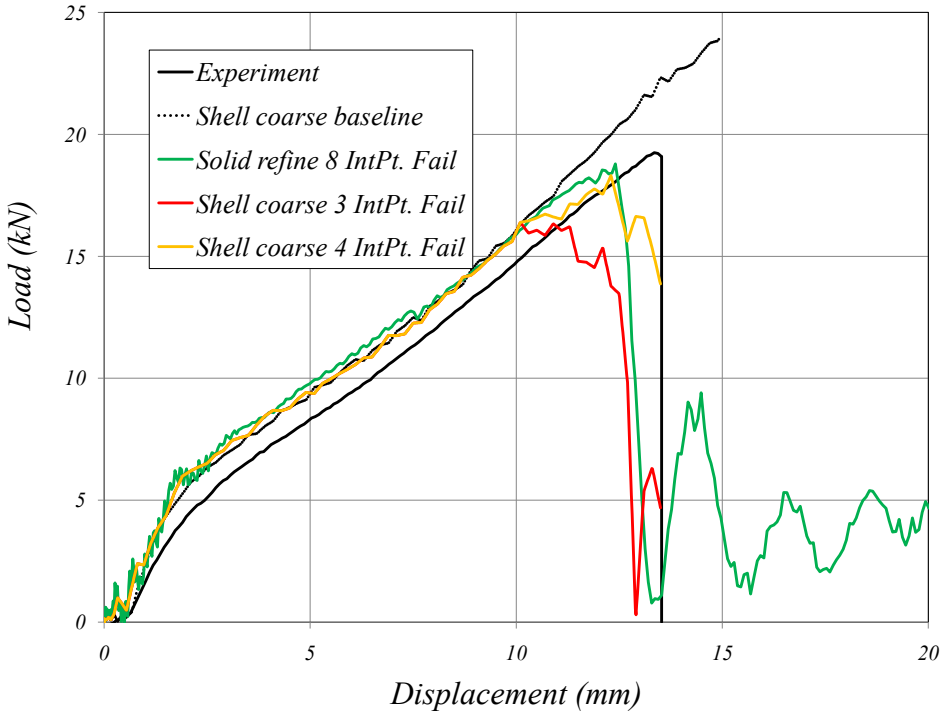

Figure 4.39: Load vs displacement curves comparison between solid refine, shell coarse models and experiment in WSII laser welded benchmark.

Finally, it is important to give an overview of the computing performances between the different models. All numerical simulations were carried out using a computer type `x86_64-suse-linux` with two parallel processors. Intel MPI compiler has been used to generate the Usermat executable of Ls-dyna version 971 R6.1.2, which was used to run the simulations in the current investigation. Some important characteristics of solid refine and shell coarse models are summarized in table 4.1.

Table 4.1: Performances comparison between solid refine and shell coarse models.

Models	no. of nodes	F_{max} (kN)	IE (kN-mm)	CPU time
Solid refine	119934	18.8	99.78	9h 9min 37s
Shell coarse baseline	950	N/A	144.9	22min 4s
Shell coarse multimaterial	950	18.3	77.6	35min 21s

As one can observe, the multimaterial shell coarse model allows now a very good estimation of the ultimate load using a CPU time relatively comparable to the one used in the baseline model proposed and used by Faurecia Automotive Seating Engineers. This will allow the use of the multimaterial shell coarse model in the industrial context where a full car seat can be modeled to perform a crash simulation.

Concluding remarks and perspectives

To reduce the fuel economy and due to the environmental safety concerns, light weight with high strength materials have become of great interest in the car industry. Faurecia Automotive Seating holds a vital place amongst the car seat manufacturing industries. There are several hundred welded joints involved to manufacture a car seat. Therefore, an accurate prediction of material behavior constitutes a great challenge.

To study the influence of different welding parameters on the ultimate welding strength compared to a FE modeling using a simple welding line, Engineers of Faurecia Automotive Seating developed a FE model called here "*Solid refine model*" SRM) to represent the real geometry of the welding assembly. This model has shown to be capable of predicting the the local welding behavior until failure. Unfortunately, due to the high computational time, this kind of modeling cannot be adopted for complete car seat. Another FE model called in this thesis "*Shell coarse model*" (SCM) was also proposed by Faurecia Automotive Seating to overcome the high computational cost problem. SCM is computationally efficient but it cannot predict accurately the weld line behavior.

Therefore, the objective of the present investigation is to develop a multimaterial User Element including a User Material model within the commercial software Ls-dyna, in order to enhance the SCM to allow it predicting the accurate weld line behavior until failure, to be used by the engineers of Faurecia Automotive Seating company at a low cost.

At first an introduction to laser welding technology has been given showing its importance in automobile industry. Different types of laser gaining media and some progress to improve the laser welding techniques were discussed. The influence of microstructure of different kind of steels on their mechanical properties were reviewed. Microstructural studies revealed that very hard matensitic structure was present in the FZ due to the fast cooling rate whereas tempered martensite in the HAZ. It was also found that high strength low alloy steels showed rupture in the HAZ during mechanical testing. A number of stress improvement methods had been reviewed from the latest published papers and interpolation covers method was selected to develop enriched element. Most commonly used damage models were also briefly discussed.

In the second chapter, the formulation of explicit dynamic time integration was discussed. In explicit methods, at first the accelerations are determined from the equations of dynamics and then integrated to obtain the displacements. It was also stated that the central difference scheme is used to integrate the equations of motion in explicit method. Explicit dynamic schemes do not check equilibrium requirements at the end of each increment of time that leads to the additional computational advantages. Then an experimental analysis based on the arcan test set up was discussed to conduct mechanical characterization and welding subsystem was also detailed. Two different kind of FE models called "*solid refine model*" and "*shell coarse model*" were presented and their performances were also evaluated. Numerical calculations were carried out in explicit dynamic conditions and $0.2m/s$ velocity was used as peeling force. Material data

of different material zones were presented and contacts used between these material zones were also discussed.

The SRM composed by melted zone (MZ), heat affected zone (HAZ) and base material (BM) was modeled by 3D solid elements with mesh size $0.2mm$. This model showed realistic representation of the welding sections, material and accurate prediction of failure of the welding line. Due to numerical computation time it was not possible to use it in a complete structure during dynamic loading as front crash on seat structure. To address this issue, the SCM was introduced using only coarse shell elements of size $1.5mm$ to make numerical simulations faster. This kind of modeling can be used in the complete part due to its low computational cost but it was not able to capture stress concentrations accurately in the vicinity of weld line and hence did not show rupture. Von mises result comparison was carried out between solid refine and shell coarse models. This comparison demonstrated that SCM got failed to capture stress concentration in the vicinity of weld line due to the absence of HAZ.

Chapter 3, proposes the formulation and evaluation of a new enriched quadrilateral shell element based on the famous MITC shell element. The formulation of the shell element is based on the Reissner–Mindlin assumptions of "material fibres originally straight and normal to the shell mid-surface do not stretch and remain straight" and "zero stress normal to the shell mid-surface". This four node shell element possess six degrees of freedom per node with a quadratic representation on z of the strains along the thickness. To demonstrate the validity of the implemented shell element, three different numerical applications were tested successfully and their results were compared with ABAQUS shell element S4 and with analytical reference solutions. It was concluded after comparing the results that the implemented shell element shows more accurate results and gives faster solution convergence compared to standard ABAQUS S4 shell elements.

To enrich the standard 4-node shell element, interpolation covers method (ICM) was selected and its formulation was detailed. The main idea of the ICM is to use new set of interpolation cover functions developed over patches of elements along with standard FE shape functions. The ICM was capable to improve the solution accuracy without mesh refinement procedure. To evaluate the accuracy of the proposed enrichment method, three different academic applications were carried out and their results were compared with obtained using very fine mesh and also with some reference solutions. It was summarized after results comparison that ICM is capable of capturing the stresses accurately even with the coarser mesh size. The influence of the selection of nearest neighboring nodes on the solution accuracy was also studied and investigated.

In chapter four, a new multimaterial model especially dedicated to laser welding, has been proposed. At first a standard elasto-plastic model based on isotropic hardening assumption is introduced and a user material subroutine (UMAT) was implemented into the explicit dynamic code of Ls-dyna to be able to model the steel metallic sheets to be assembled using laser welding process. Then a multimaterial element was presented including the HAZ and the BM within the same element. To this end, a weak discontinuity of material inside the element has been presented and numerical integration of the internal force vector has been discussed. Three different numerical applications of the proposed material model were presented and their results were compared with the reference solid models. The proposed material model showed the capability to capture the high concentration of stresses and plastic strain accurately after comparing with the reference solid models.

At the end of chapter four, the generalized incremental stress dependent damage model has been presented, with its implementation within the commercial software Ls-dyna to predict failure in the welding subsystem WSII. In order to improve the efficiency of failure prediction, it has been shown that triaxiality stress state is very important. Therefore, the plastic incompressibility condition has been forced within the multimaterial element to estimate the transverse

stress component in a post-processing phase. This 3D stress state helped to enhance the stress triaxiality in the shell structures. Shell coarse model anticipated failure in the weld line by using stress based damage model and it also showed the load-displacement curve in the similar fashion as observed in the solid refine model with the same maximum value of load $19.5kN$.
As it is the case for any research investigation, some developments need to be undertaken in order to improve the proposed multimaterial model. First it appears to be necessary to apply the multimaterial model for WSII using other loading conditions to study its performances. It is also interesting to study the behavior of the proposed model when dealing with other materials than S500 and S420 steels. Further investigations are necessary also to improve the transverse stress estimation, using some simplified formulas of bending and unbending of elasto-plastic beam, which are used in sheet metal forming. Finally, it will be also interesting to rethink completely the estimation of the transverse stress, by formulation a thick shell element called generally in the literature Solid-shell elements which can take into account the transverse stress naturally.

Bibliography

[1] Bleck, W., "Cold-rolled, high-strength sheet steels for auto applications", *JOM*, 48(7), 26-30, 1996.

[2] Hamm L., "Stahl-ein zukunftst Rachtiger Werkstoff im Karosseriebau", *Proc. IISI 27th Annual Meeting and Conference, Paris*, 1993.

[3] Kuziak R., Kawalla R. and Waengler S., "Advanced high strength steels for automotive industry", *Archives of civil and mechanical engineering*, 8(2), 103-117, 2008.

[4] Carry H.B. and Helzer S.C., "Modern Welding Technology", *Pearson Education Inc., New Jersey, U.S.A.*, 2005.

[5] Ma C., Chen D.L., Bhole S.D., Boudreau G., Lee A. and Biro E., "Microstructure and fracture characteristics of spot-welded DP600 steel", *Materials Science and Engineering: A*, 485(1), 334-346, 2008.

[6] Rossillon F., Galtier A., Robert J.L., Duchet M., Lens A. and Oikawa H., "Effect of welding cycle on the fatigue behaviour of resistance spot welded dual phase steels", *Welding in the World*, 52(11-12), 30-41, 2008.

[7] Ghosh P.K., Gupta P.C., Avtar R.A.M. and Jha B.K., "Resistance spot weldability of comparatively thick C-Mn-Cr-Mo dual phase steel sheet", *ISIJ International*, 30(3), 233-240, 1990.

[8] Daneshpour S., Riekehr S., Kocak M. and Gerritsen C.H.J., "Mechanical and fatigue behaviour of laser and resistance spot welds in advanced high strength steels", *Science and Technology of Welding and Joining*, 2013.

[9] Koganti R., Angotti S., Joaquin A. and Stiles E., "Laser Hybrid Welding of Advanced High Strength Steels (AHSS) for Automotive Body Construction", *In ASME 2007 International Mechanical Engineering Congress and Exposition. American Society of Mechanical Engineers*, 699-703, 2007.

[10] Miles M.P., Pew J., Nelson T.W. and Li M., "Comparison of formability of friction stir welded and laser welded dual phase 590 steel sheets", *Science and Technology of Welding and Joining*, 11(4), 384-388, 2006.

[11] Larsson J.K., "Overview of joining technologies in the automotive industry", *Welding Research Abroad*, 49(6/7), 29-45, 2003.

[12] Dahotre N.B. and Harimkar S.P., "Laser Fabrication and Machining of Materials", *Edition Springer*, ISBN 978-0-387-72344-0, 558 pages, 2008.

[13] Kovacevic R., "Welding Process", *Edition InTech*, ISBN 979-953-307-1089-4, DOI:10.5772/45850, 2012.

[14] Karlsson J., "Two laser welding cases and suitable documentation methods.", *Lulea tekniska universitet*, 2010.

[15] Fan Y., "Mechanical properties of laser beam welded Ti6Al4V.", *Doctoral dissertation, University of Nottingham*, 2010.

[16] Sonti N., "Influence of Process Parameters on Laser Weld Characteristics in Aluminum Alloys.", *PENNSYLVANIA STATE UNIV UNIVERSITY PARK APPLIED RESEARCH LAB*, 1988.

[17] Sivakumar M., "Lasers in Materials Processing and Manufacturing", *Department of Sciences Amrita University*, 2013.

[18] Weglowski M.S., Kwiecinski K., Krasnowski K. and Jachym R., "Characteristics of Nd:YAG laser welded joints of dual phase steel", *Archives of Civil and Mechanical engineering*, 9(4), 85-97, 2009.

[19] Farabi N., Chen D.L., Li J., Zhou Y. and Dong S.J., "Microstructure and mechanical properties of laser welded DP600 steel joints", *Materials Science and Engineering A*, 527(4), 1215-1222, 2010.

[20] Farabi N., Chen D.L. and Zhou Y., "Microstructure and mechanical properties of laser welded dissimilar DP600/DP980 dual-phase steel joints", *Journal of Alloys and Compounds*, 509(3), 982-989, 2011.

[21] Xu W., Westerbaan D., Nayak S.S., Chen D.L., Goodwin F., Biro E. and Zhou Y., "Microstructure and fatigue performance of single and multiple linear fiber laser welded DP980 dual-phase steel", *Materials Science and Engineering A*, 51-58, 2012.

[22] Coelho R.S., Corpas M., Moreto J.A., Jahn A., Standfuss J., Kaysser-Pyzalla A. and Pinto H., "Induction-assisted laser beam welding of a thermomechanically rolled HSLA S500MC steel: A microstructure and residual stress assessment", *Materials Science and Engineering A*, 125-133, 2013.

[23] Parkes D., Xu W., Westerbaan D., Nayak S.S., Zhou Y., Goodwin F., Bhole S. and Chen D.L., "Microstructure and fatigue properties of fiber laser welded dissimilar joints between high strength low alloy and dual-phase steels", *Materials and Design*, 665-675, 2013.

[24] Dong D., Liu Y., Yang Y., Li J., Ma M. and Jiang T., "Microstructure and dynamic tensile behavior of DP600 dual phase steel joint by laser welding", *Materials Science and Engineering A*, 17-25, 2014.

[25] Ahmed E.A.A. and Reisgen U., "Laser welding of advanced high strength steels (No. RWTH-CONV-125622)", *Lehrstuhl und Institut fur Schweisstechnik und Fugetechnik*, 2011.

[26] Ha J. and Huh H., "Failure characterization of laser welds under combined loading conditions", *International Journal of Mechanical Sciences*, 40-58, 2013.

[27] Mayboudi L.S., Birk A.M., Zak G. and Bates P.J., "A three-dimensional thermal finite element model of laser transmission welding for lap-joint.", *International Journal of Modelling and Simulation*, 29(2), 149-155, 2009.

[28] Mayboudi L.S., Birk A.M., Zak G. and Bates P.J., "Finite volume model for laser-soot interaction for a laser transmission welding process", *Journal of Laser Applications*, 22(1), 22-28, 2010.

[29] Shanmugam N.S., Buvanashekaran G., Sankaranarayanasamy K. and Manonmani K., "Some studies on temperature profiles in AISI 304 stainless steel sheet during laser beam welding using FE simulation.", *The International Journal of Advanced Manufacturing Technology*, 43(1-2), 78-94, 2009.

[30] Buvanashekaran G., Shanmugam S.N., Sankaranarayanasamy K. and Sabarikanth R., "A study of laser welding modes with varying beam energy levels.", *Proceedings of the Institution of Mechanical Engineers, Part C: Journal of Mechanical Engineering Science*, 223(5), 1141-1156, 2009.

[31] Mahnken R., Shaban A., Potente H. and Wilke L., "Thermoviscoplastic modelling of asymmetric effects for polymers at large strains.", *International Journal of Solids and Structures*, 45(17), 4615-4628, 2008.

[32] Potente H., Wilke L., Ridder H., Mahnken R. and Shaban A., "Simulation of the residual stresses in the contour laser welding of thermoplastics.", *Polymer Engineering and Science*, 48(4), 767-773, 2008.

[33] Lacki P. and Adamus K., "Numerical simulation of the electron beam welding process.", *Computers and Structures*, 89(11), 977-985, 2011.

[34] Turna M., Taraba B., Ambroz P. and Sahul M., "Contribution to numerical simulation of laser welding.", *Physics Procedia*, 12, 638-645, 2011.

[35] Chen S., Li L., Chen Y., Dai J. and Huang J., "Improving interfacial reaction nonhomogeneity during laser weldingâĂŞbrazing aluminum to titanium.", *Materials and Design*, 32(8), 4408-4416, 2011.

[36] Nelias D., Jullien J.F., Boitout F., Dischert L. and Noe X., "Finite element analysis of metallurgical phase transformations in AA 6056-T4 and their effects upon the residual stress and distortion states of a laser welded T-joint.", *International Journal of Pressure Vessels and Piping*, 88(1), 45-56, 2011.

[37] Han Q., Kim D., Kim D., Lee H. and Kim N., "Laser pulsed welding in thin sheets of Zircaloy-4.", *Journal of Materials Processing Technology*, 212(5), 1116-1122, 2012.

[38] Montalvo-Urquizo J., Akbay Z. and Schmidt A., "Adaptive finite element models applied to the laser welding problem.", *Computational Materials Science*, 46(1), 245-254, 2009.

[39] Salonitis K., Drougas D. and Chryssolouris G., "Finite element modeling of penetration laser welding of sandwich materials.", *Physics Procedia*, 5, 327-335, 2010.

[40] Yu S.R., Yan Y.X., Hao Z.M., Yin Y.H., Wang J. and Mo J., "Analysis of temperature distribution and its influencing factors in laser welding of beryllium cylindrical shells.", *In Key Engineering Materials*, 419, 449-452, 2010.

[41] Casalino G., Olabi A.G., Cipriani N. and Rotondo A., "Investigation on the residual stress of AISI 4047 low alloy steel laser welded.", *In Key Engineering Materials*, 344, 715-722, 2007.

[42] Balasubramanian K.R., Suthakar T., Sankaranarayanasamy K. and Buvanashekaran G., "Finite element analysis of heat distribution in laser beam welding of AISI 304 stainless steel sheet.", *International journal of manufacturing research*, 7(1), 42-58, 2012.

[43] Kuppuswamy N., Schmidt R., Seeger F. and Zhang S., "Finite element modeling of impact strength of laser welds for automotive applications.", *WIT Transactions on The Built Environment*, 94, 375-384, 2007.

[44] Kim J. and Bathe K.J., "The finite element method enriched by interpolation covers.", *Computers and Structures* , 116, 35-49., 2013.

[45] Jeon H.M., Lee P.S. and Bathe K.J., "The MITC3 shell finite element enriched by interpolation covers.", *Computers and Structures* , 134, 128-142, 2014.

[46] Kim J. and Bathe K.J., "Towards a procedure to automatically improve finite element solutions by interpolation covers.", *Computers and Structures* , 131, 81-97, 2014.

[47] Kramer R., Bochev P., Siefert C. and Voth T., "An extended finite element method with algebraic constraints (XFEM-AC) for problems with weak discontinuities.", *Computer Methods in Applied Mechanics and Engineering*, 266, 70-80, 2013.

[48] Benson D.J., Bazilevs Y., De Luycker E., Hsu M.C., Scott M., Hughes T.J.R. and Belytschko T., "A generalized finite element formulation for arbitrary basis functions: from isogeometric analysis to XFEM.", *International Journal for Numerical Methods in Engineering*, 83(6), 765-785, 2010.

[49] Natarajan S., Mahapatra D.R. and Bordas S., "Integrating strong and weak discontinuities without integration subcells and example applications in an XFEM/GFEM framework.", *International Journal for Numerical Methods in Engineering*, 83(3), 269-294, 2010.

[50] Dreau K., Chevaugeon N. and Moes N., "Studied X-FEM enrichment to handle material interfaces with higher order finite element.", *Computer Methods in Applied Mechanics and Engineering*, 199(29), 1922-1936, 2010.

[51] Soghrati S. and Geubelle P.H., "A 3D interface-enriched generalized finite element method for weakly discontinuous problems with complex internal geometries.", *Computer Methods in Applied Mechanics and Engineering*, 217, 46-57, 2012.

[52] Xu J., Lee C.K. and Tan K.H., "Studied X-FEM enrichment to handle material interfaces with higher order finite element.", *Computers and Structures*, 128, 64-76., 2013.

[53] Leconte N., Langrand B. and Markiewicz E., "Toward a Hybrid-Trefftz element with a hole for elasto-plasticity?", *Journal of Computational and Applied Mathematics*, 218(1), 88-95, 2008.

[54] Leconte N., Langrand B. and Markiewicz E., "On some features of a plate hybrid-Trefftz displacement element containing a hole.", *Finite Elements in Analysis and Design*, 46(10), 819-828, 2010.

[55] Piltner R., "Some remarks on finite elements with an elliptic hole.", *Finite elements in analysis and design*, 44(12), 767-772, 2008.

[56] Wang H. and Qin Q.H., "Fundamental-solution-based hybrid FEM for plane elasticity with special elements.", *Computational Mechanics*, 48(5), 515-528, 2011.

[57] Icardi U. and Sola F., "Variable Singularity Power Wedge Element for Multilayered Composites.", *Universal Journal of Engineering Science*, 2(1), 16-29, 2014.

[58] Mukhopadhyay N.K., Maiti S.K. and Kakodkar A., "Variable singularity boundary element and its applications in computation of SIFs.", *Computers and Structures*, 77(2), 141-154, 2000.

[59] Cheng C., Niu Z., Zhou H. and Recho N., "Evaluation of multiple stress singularity orders of a V-notch by the boundary element method.", *Engineering analysis with boundary elements*, 33(10), 1145-1151, 2009.

[60] Pageau S.S. and Biggers S.B., "Finite element evaluation of free?edge singular stress fields in anisotropic materials.", *International journal for numerical methods in engineering*, 38(13), 2225-2239, 1995.

[61] Soghrati S. and Geubelle P.H., "A 3D interface-enriched generalized finite element method for weakly discontinuous problems with complex internal geometries.", *Computer Methods in Applied Mechanics and Engineering*, 217, 46-57, 2012.

[62] Michel J.C., Moulinec H. and Suquet P., "Effective properties of composite materials with periodic microstructure: a computational approach.", *Computer methods in applied mechanics and engineering*, 172(1), 109-143, 1999.

[63] Masoud S., Ahmad R. N., Nancy R. S. and Philippe H. G., "A NURBS-based interface-enriched generalized finite element method for problems with complex discontinuous gradient fields.", *International Journal for Numerical Methods in Engineering*, 101, 950-964, 2015.

[64] Payen D.J. and Bathe K.J., "The use of nodal point forces to improve element stresses.", *Computers and Structures*, 89(5), 485-495, 2011.

[65] Payen D.J. and Bathe K.J., "Improved stresses for the 4-node tetrahedral element.", *Computers and Structures*, 89(13), 1265-1273, 2011.

[66] Payen D.J., "A method to significantly improve finite element stress predictions.", *Doctoral dissertation, Massachusetts Institute of Technology*, 2012.

[67] Bathe K.J., "Finite element procedures.", *Prentice Hall*, 1996.

[68] Chapelle D., Bathe K.J., "The finite element analysis of shells ? fundamentals.", *2nd ed. Springer*, 2010.

[69] Payen D.J. and Bathe K.J., "A stress improvement procedure.", *Computers and Structures*, 112, 311-326, 2012.

[70] Stein E. and Ohnimus S., "Equilibrium method for postprocessing and error estimation in the finite element method.", *Computer Assisted Mechanics and Engineering Sciences*, 4, 645-666, 2012.

[71] Brezzi F. and Fortin,M., "Mixed and Hybrid Finite Element Methods.", *no. 15 in Springer Series in Computational Mathematics*, 1991.

[72] Brezzi F. and Bathe K.J., "A discourse on the stability conditions for mixed finite element formulations.", *Computer methods in applied mechanics and engineering*, 82(1-3), 27-57, 1990.

[73] Dhia H.B. and Rateau G., "The Arlequin method as a flexible engineering design tool.", *International journal for numerical methods in engineering*, 62(11), 1442-1462, 2005.

[74] Ghanem A., Torkhani M., Mahjoubi N., Baranger T.N. and Combescure A., "Arlequin framework for multi-model, multi-time scale and heterogeneous time integrators for structural transient dynamics.", *Computer Methods in Applied Mechanics and Engineering*, 254, 292-308, 2013.

[75] Ben Dhia H. and Zammali C., "Level-Sets and Arlequin framework for dynamic contact problems.", *Revue Europeenne des Elements*, 13(5-7), 403-414, 2004.

[76] Hu H., Belouettar S. and Potier-Ferry M., "Multi-scale modelling of sandwich structures using the Arlequin method Part I: Linear modelling.", *Finite Elements in Analysis and Design*, 45(1), 37-51, 2008.

[77] Qiao H., Yang Q.D., Chen W.Q. and Zhang C.Z., "Implementation of the Arlequin method into ABAQUS: Basic formulations and applications.", *Advances in Engineering Software*, 42(4), 197-207, 2011.

[78] Gurson, A.L., "Continuum theory of ductile rupture by void nucleation and growth: Part I?Yield criteria and flow rules for porous ductile media", *Journal of engineering materials and technology*, 99(1), 2-15, 1977.

[79] Gurson, A.L., "Porous rigid plastic materials containing rigid inclusions; yield function, plastic potential and void nucleation", *Int. Conf. Fracture Waterloo (Canada)*, 1977.

[80] Gurson, A.L., "Plastic flow and fracture behavior of ductile materials incorporating void nucleation, growth and coalescence", *PhD Diss, Brown University*, 1975.

[81] Tvergaard V. and Needleman A., "Analysis of the cup-cone fracture in a round tensile bar", *Acta metallurgica*, 32(1), 157-169, 1984.

[82] Needleman A. and Tvergaard V., "An analysis of ductile rupture in notched bars", *Journal of the Mechanics and Physics of Solids*, 32(6), 461-490, 1984.

[83] Acharyya S. and Dhar S., "A complete GTN model for prediction of ductile failure of pipe", *Journal of Materials Science*, 43(6), 1897-1909, 2008.

[84] Wang X. and Shi J., "Validation of Johnson-Cook plasticity and damage model using impact experiment", *International Journal of Impact Engineering*, 60, 67-75, 2013.

[85] Johnson G.R. and Cook W.H., "A constitutive model and data for metals subjected to large strains, high strain rates and high temperatures", *In Proceedings of the 7th International Symposium on Ballistics*, 21, 541-547, 1983.

[86] Johnson G.R. and Cook W.H., "Fracture characteristics of three metals subjected to various strains, strain rates, temperatures and pressures", *Engineering fracture mechanics*, 21(1), 31-48, 1985.

[87] Macdougall D.A.S. and Harding J., "A constitutive relation and failure criterion for Ti6Al4V alloy at impact rates of strain", *Journal of the Mechanics and Physics of Solids*, 47(5), 1157-1185, 1999.

[88] Meyer, H.W. and Kleponis, D.S., "Modeling the high strain rate behavior of titanium undergoing ballistic impact and penetration", *International Journal of Impact Engineering*, 26(1), 509-521, 2001.

[89] Tham C.Y., Tan V.B.C. and Lee H.P., "Ballistic impact of a KEVLAR helmet: Experiment and simulations", *International Journal of Impact Engineering*, 35(5), 304-318, 2008.

[90] Peirs J., Verleysen P., Van Paepegem W. and Degrieck J., "Determining the stress-strain behaviour at large strains from high strain rate tensile and shear experiments", *International Journal of Impact Engineering*, 38(5), 406-415, 2011.

[91] Banerjee A., Dhar S., Acharyya S., Datta D. and Nayak N., "Determination of Johnson cook material and failure model constants and numerical modelling of Charpy impact test of armour steel", *Materials Science and Engineering*, 640, 200-209, 2015.

[92] Schwer, L., "Optional Strain-rate forms for the Johnson Cook Constitutive Model and the Role of the parameter Epsilon 0", *LS-DYNA Anwenderforum, Frankenthal*, 2007.

[93] Hancock J.W. and Mackenzie A.C., "On the mechanisms of ductile failure in high-strength steels subjected to multi-axial stress-states", *Journal of the Mechanics and Physics of Solids*, 24(2-3), 147-160, 1976.

[94] Liu J., Bai Y. and Xu C., "Evaluation of ductile fracture models in finite element simulation of metal cutting processes", *Journal of Manufacturing Science and Engineering*, 136(1), 011010, 2014.

[95] Bao Y. and Wierzbicki T., "On fracture locus in the equivalent strain and stress triaxiality space", *International Journal of Mechanical Sciences*, 46(1), 81-98, 2004.

[96] Wilkins M.L., Streit R.D. and Reaugh J.E., "Cumulative-strain-damage model of ductile fracture: simulation and prediction of engineering fracture tests (No. UCRL-53058)", *Lawrence Livermore National Lab., CA (USA); Science Applications, Inc., San Leandro, CA (USA)*, 1980.

[97] McClintock, Frank A, "Plasticity aspects of fracture", *Fracture: an advanced treatise 3*, 47-225, 1971.

[98] Livermore Software Technology Corporation; (LSTC), "LS Dyna Keyword User's manual Volume 2 Material models R 7.1", 2014.

[99] Papadrakakis M., Papadopoulos V., Stefanou G. and Plevris V., "MATERIAL MODELLING OF CAST ALUMINIUM BY APPLICATION OF THE WILKINS DAMAGE MODEL.", *VII European Congress on Computational Methods in Applied Sciences and Engineering* , 2016.

[100] Yamasaki H. and Nishimura R., "Development of Material Model for Crack Propagation of Casted Aluminum.", *LS-DYNA Anwenderforum Frankenthal*, 2007.

[101] Feucht M., Sun D.Z., Erhart T. and Frank T., "Recent development and applications of the Gurson model.", *In Proceedings of the 5th LS-DYNA Forum, Ulm, Germany*, 2006.

[102] Neukamm F., Feucht M. and Haufe A., "Considering damage history in crashworthiness simulations", *7th European LS-DYNA Conference*, 2009.

[103] Neukamm, F., Feucht, M. and Haufe, A., "Consistent damage modelling in the process chain of forming to crashworthiness simulations", *In The 7th German LS-DYNA Conference, Bamberg, Germany, volume 30*, 2008.

[104] Neukamm F., Feucht M. and Bischoff M., "On the Application of Continuum Damage Models to Sheet Metal Forming Simulations", *In International Conference on Computational Plasticity COMPLAS X, Barcelona, Spain*, 2009.

[105] Basaran M., Wolkerling S.D., Feucht M., Neukamm F., Weichert D. and AG D., "An extension of the GISSMO damage model based on lode angle dependence", *In LS-Dyna forum. Dynamore, Bamberg*, 2010.

[106] Neukamm F., Feucht M., Haufe A. and Roll K., "On closing the constitutive gap between forming and crash simulation", *In 10th Internation LS-DYNA Users Conference 2008, Dearborn, Michigan, USA*, 2008.

[107] Ebelsheiser H., Feucht M. and Neukamm F., "On calibrating advanced damage models using sheet metal coupon tests", *In LS-Dyna forum. Daimler AG, Bamberg*, 2008.

[108] Effelsberg J., Haufe A., Feucht M., Neukamm F. and Du Bois P., "On parameter identification for the GISSMO damage model", *In Proceedings of the 12th international LS-DYNA users conference. Detroit*, 2012.

[109] Basaran M., "Stress state dependent damage modelling with a focus on lode angle influence", *PhD thesis, RWTH Aachen university* , 2011.

[110] Andrade F.X.C., Feucht M., Haufe A. and Neukamm F., "An incremental stress state dependent damage model for ductile failure prediction", *International Journal of Fracture*, 1-24, 2016.

[111] Belytschko T., " An overview of semidiscretization and time integration procedures", *Computational methods for transient analysis*, Amsterdam, North-Holland, 1-65, 1983.

[112] ANSYS Academic Research, " Release 16.2, Help System, Coupled Field Analysis Guide", *ANSYS, Inc.*

[113] Hibbitt, Karlsson and Sorensen, " ABAQUS/Explicit: User's Manual", *Hibbitt, Karlsson and Sorenson Incorporated*, (Vol. 1), 2001.

[114] ADINA R., " An ADINA System 8.8 Documentation", , 1-65, 2011.

[115] Manual L.D.T., " An Version 970, Livermore Software Tech. Corp", , April, 2003.

[116] Belytschko T., " A survey of numerical methods and computer programs for dynamic structural analysis", *Nuclear Engineering and Design*, 37(1), 23-34, 1976.

[117] Kirkpatrick S.W., Schroeder M. and Simons J.W., " Evaluation of passenger rail vehicle crashworthiness", *International Journal of Crashworthiness*, 6(1), 95-106, 2001.

[118] Cook R.D., Malkus D.S. and Plesha M.E., " Concepts and applications of finite element method", *John Willey and Sons, New York*, 1989.

[119] Chung K. and Shah K., "Finite element simulation of sheet metal forming for planar anisotropic metals", *International Journal of Plasticity*, 8(4), 453-476, 1992.

[120] Chung K. and Richmond O., "A deformation theory of plasticity based on minimum work paths", *International Journal of Plasticity*, 9(8), 907-920, 1993.

[121] Chung K., Lee S.Y., Barlat F., Keum Y.T. and Park J.M., "Finite element simulation of sheet forming based on a planar anisotropic strain-rate potential", *International Journal of Plasticity*, 12(1), 93-115, 1996.

[122] Simo J.C. and Ortiz M., "A unified approach to finite deformation elastoplastic analysis based on the use of hyperelastic constitutive equations", *Computer methods in applied mechanics and engineering*, 49(2), 221-245, 1985.

[123] Armero F. and Simo J.C., "A priori stability estimates and unconditionally stable product formula algorithms for nonlinear coupled thermoplasticity", *International Journal of Plasticity*, 9(6), 749-782, 1993.

[124] Auricchio F. and Taylor R.L., "A return-map algorithm for general associative isotropic elasto-plastic materials in large deformation regimes", *International Journal of Plasticity*, 15(12), 1359-1378, 1999.

[125] Tugcu P. and Neale K.W., "On the implementation of anisotropic yield functions into finite strain problems of sheet metal forming", *International Journal of Plasticity*, 15(10), 1021-1040, 1999.

[126] Hashiguchi K., "Generalized plastic flow rule", *International Journal of Plasticity*, 21(2), 321-351, 2005.

[127] Yoon J.W., Yang D.Y., Chung K. and Barlat F., "A general elasto-plastic finite element formulation based on incremental deformation theory for planar anisotropy and its application to sheet metal forming", *International Journal of Plasticity*, 15(1), 35-67, 1999.

[128] Han C.S., Chung K., Wagoner R.H. and Oh S.I., "A multiplicative finite elasto-plastic formulation with anisotropic yield functions", *International Journal of Plasticity*, 19(2), 197-211, 2003.

[129] Simo J.C. and Hughes T.J.R., "Computational Inelasticity Springer-Verlag", *New York*, 143-149, 1998.

[130] Ortiz M. and Simo J.C., "An analysis of a new class of integration algorithms for elastoplastic constitutive relations", *International Journal for Numerical Methods in Engineering*, 23(3), 353-366, 1986.

[131] Arcan M., Hashin Z.A. and Voloshin A., "A method to produce uniform plane-stress states with applications to fiber-reinforced materials", *Experimental mechanics*, 18(4), 141-146, 1978.

[132] Voloshin A. and Arcan M., "Pure shear moduli of unidirectional fibre-reinforced materials (FRM)", *Fibre Science and Technology*, 13(2), 125-134, 1980.

[133] d'Almeida J.R.M. and Monteiro S.N., "The Iosipescu test method as a method to evaluate the tensile strength of brittle materials", *Polymer Testing*, 18(6), 407-414, 1999.

[134] Cognard J.Y., Sohier L. and Davies P., "A modified Arcan test to analyze the behavior of composites and their assemblies under out-of-plane loadings", *Composites Part A: Applied science and manufacturing*, 42(1), 111-121, 2011.

[135] Sutton M.A., Deng X., Ma F., Newman Jr J.C. and James M., "Development and application of a crack tip opening displacement-based mixed mode fracture criterion", *International Journal of Solids and Structures*, 37(26), 3591-3618, 2000.

[136] Sutton M.A., Boone M.L., Ma F. and Helm J.D., "A combined modeling?experimental study of the crack opening displacement fracture criterion for characterization of stable crack growth under mixed mode I/II loading in thin sheet materials", *Engineering Fracture Mechanics*, 66(2), 171-185, 2000.

[137] Langrand B. and Combescure A., "Non-linear and failure behaviour of spotwelds: a global finite element and experiments in pure and mixed modes I/II", *International journal of solids and structures*, 41(24), 6631-6646, 2004.

[138] Kavamura H.A. and Batalha G.F., "Mechanical strength evaluation for Nd-YAG laser and electric resistance spot weld (ERSW) joint under multiaxial loading.", *Journal of materials processing technology*, 201(1), 507-514, 2008.

[139] Lin S.H., Pan J., Tyan T. and Prasad P., "A general failure criterion for spot welds under combined loading conditions", *International Journal of Solids and Structures*, 40(21), 5539-5564, 2003.

[140] Lemaitre J., "A continuous damage mechanics model for ductile fracture", *Journal of engineering materials and technology*, 107(1), 83-89, 1985.

[141] McClintock F.A., "A criterion for ductile fracture by the growth of holes", *Journal of applied mechanics*, 35(2), 363-371, 1968.

[142] Rice J.R. and Tracey D.M., "On the ductile enlargement of voids in triaxial stress fields", *Journal of the Mechanics and Physics of Solids*, 17(3), 201-217, 1969.

[143] Hancock J.W. and Mackenzie A.C., "On the mechanisms of ductile failure in high-strength steels subjected to multi-axial stress-states", *Journal of the Mechanics and Physics of Solids*, 24(2-3), 147-160, 1976.

[144] Mackenzie A.C., Hancock J.W. and Brown D.K., "On the influence of state of stress on ductile failure initiation in high strength steels", *Engineering fracture mechanics*, 9(1), pp.167-168, 1977.

[145] Johnson G.R. and Cook W.H., "Fracture characteristics of three metals subjected to various strains, strain rates, temperatures and pressures", *Engineering fracture mechanics*, 21(1), 31-48, 1985.

[146] Bao Y. and Wierzbicki T., "A comparative study on various ductile crack formation criteria", *Journal of Engineering Materials and Technology*, 126(3), 314-324, 2004.

[147] Ottosen N.S. and Ristinmaa M., "The mechanics of constitutive modeling", *Elsevier*, 2005.

[148] Ottosen N.S. and Ristinmaa M., "The mechanics of constitutive modeling", *Elsevier*, 2005.

[149] Wierzbicki T. and Xue L., "On the effect of the third invariant of the stress deviator on ductile fracture", *Impact and Crashworthiness Laboratory, Technical Report*, (136), 2005.

[150] Kachanov L.M., "Rupture time under creep conditions", *International journal of fracture*, 97(1-4), 11-18, 1999.

[151] Rabotnov Y.N., "On the equations of state for creep", *Progress in Applied Mechanics*, 12, 307-315, 1963.

[152] Chaboche J.L., "Continuum damage mechanics: Part II-Damage growth, crack initiation, and crack growth", *Journal of applied mechanics*, 55(1), 65-72, 1988.

[153] Lemaitre J., "How to use damage mechanics", *Nuclear engineering and design*, 80(2), 233-245, 1984.

[154] Bonora N., Ruggiero A., Esposito L. and Gentile D., "CDM modeling of ductile failure in ferritic steels: assessment of the geometry transferability of model parameters", *International Journal of Plasticity*, 22(11), 2015-2047, 2006.

[155] Chaouadi R., De Meester P. and Vandermeulen W., "Damage work as ductile fracture criterion", *International Journal of Fracture*, 66(2), 155-164, 1994.

[156] Teng X., Wierzbicki T. and Huang M., "Ballistic resistance of double-layered armor plates", *International journal of impact engineering*, 35(8), 870-884, 2008.

[157] Bai Y., Bao Y. and Wierzbicki T., "Fracture of prismatic aluminum tubes under reverse straining", *International journal of impact engineering*, 32(5), 671-701, 2006.

[158] Xue L., " Ductile fracture modeling-theory, experimental investigation and numerical verification", *Doctoral dissertation, Massachusetts Institute of Technology*, 2007.

[159] Tasan C.C., " Micro-mechanical characterization of ductile damage in sheet metal", *TU Delft, Delft*, 2010.

[160] Weck A., Wilkinson D.S., Toda H., and Maire E., " 2D and 3D visualization of ductile fracture", *Advanced Engineering Materials*, 8(6), 469-472, 2006.

[161] Weck A. and Wilkinson D.S., " Experimental investigation of void coalescence in metallic sheets containing laser drilled holes", *Acta Materialia*, 56(8), 1774-1784, 2008.

[162] Xue L., " Damage accumulation and fracture initiation in uncracked ductile solids subject to triaxial loading", *International journal of solids and structures*, 44(16), 5163-5181, 2007.